Transmission Electron Microscopy on GaAs Nanowires – Spontaneous Polarization and MnAs Nanocrystals

Dissertation

zur Erlangung des
Doktorgrades der Naturwissenschaften (Dr. rer. nat.)
der Fakultät für Physik der
Universität Regensburg

vorgelegt von

Benedikt Bauer, geb. Eberl
aus Dachau

im Jahr 2015

Promotionsgesuch eingereicht am: 2. Oktober 2014
Die Arbeit wurde angeleitet von: Prof. Dr. Josef Zweck

Prüfungsausschuss:

Vorsitzender:	Prof. Dr. Gunnar Bali
1. Gutachter:	Prof. Dr. Josef Zweck
2. Gutachter:	Prof. Dr. Dominique Bougeard
Weiterer Gutachter:	Prof. Dr. John Lupton

Contents

1 Introduction 1

2 III–V Semiconductor Nanowires 3
- 2.1 Nanowire Growth . . . 3
  - 2.1.1 Growth methods and substrates . . . 3
  - 2.1.2 Growth modes . . . 5
  - 2.1.3 The *vapour-liquid-solid* growth . . . 7
- 2.2 Properties and Applications . . . 9

3 Crystal Structures and Crystal Structure Related Effects 13
- 3.1 Zincblende and Wurtzite Crystal Structure . . . 13
  - 3.1.1 Stacking orders . . . 13
  - 3.1.2 Atomic configuration . . . 17
  - 3.1.3 Polytypism . . . 20
  - 3.1.4 Stacking faults . . . 23
- 3.2 Spontaneous Polarization . . . 26
  - 3.2.1 Structural parameters . . . 26
  - 3.2.2 Microscopic charge redistribution . . . 30
  - 3.2.3 Macroscopic implication – the quantum confined Stark effect 33
  - 3.2.4 Expected polarization strengths . . . 37
- 3.3 Summary . . . 37

4 Transmission Electron Microscopy 39
- 4.1 General Setup and Components . . . 40
  - 4.1.1 Electron source and accelerator – the gun system . . . 40
  - 4.1.2 Optical system . . . 41
  - 4.1.3 Detection . . . 43
- 4.2 Modes of Operation . . . 45
  - 4.2.1 Transmission electron microscopy (TEM) . . . 45
  - 4.2.2 Electron diffraction . . . 47
  - 4.2.3 Scanning transmission electron microscopy (STEM) . . . 48
- 4.3 Analytical Methods . . . 51
  - 4.3.1 Differential phase contrast microscopy (DPC) . . . 51
  - 4.3.2 Energy dispersive X-ray spectroscopy (EDX) . . . 55

4.4 Sample Preparation 55

5 Spontaneous Polarization in the Wurtzite Phase of III–V Nanowires 57

5.1 Detection and Quantification of the Spontaneous Polarization 57

5.1.1 Prerequisites 57

5.1.2 GaAs nanowires 59

5.1.3 GaP nanowires 69

5.1.4 Discussion 73

5.2 Factors Influencing Quantitative DPC Measurements 77

5.2.1 Simulation setup 77

5.2.2 Influence of crystal structure on the DPC signal 80

5.2.3 An analytical approach to diffraction disc broadening 83

5.2.4 Implications for quantitative DPC 88

5.3 Summary 89

6 Characterization of MnAs Nanocrystals 91

6.1 Motivation 91

6.2 Characterization 92

6.2.1 Mn supply during and after growth 92

6.2.2 Growth termination under arsenic atmosphere 97

6.3 Summary 101

7 Conclusion and Outlook 103

Appendix 105

A Growth Parameters 105

A.1 MBE-grown pure GaAs Nanowires 105

A.2 MOVPE-grown GaP Nanowires 105

A.3 MBE-Grown GaAs Nanowires with additional Mn 106

B Field Determination Data 107

B.1 Experimental parameters 107

B.2 GaP Raw Data 107

C Simulation Data 110

Bibliography 111

Own Publications 137

List of Figures

2.1 Schematic drawing of the gold-catalysed growth of GaAs nanowires. 8
2.2 Schematic drawing of the self-catalysed growth of GaAs nanowires. . 9
2.3 Number of publications per year having nanowires as topic. 10

3.1 The non-trivial unit cells of the hcp and fcc structure 14
3.2 Stacking sequence and crystal directions of hexagonal and cubic close-packed structures 15
3.3 hcp and fcc stacking seen along a $\langle 1\bar{1}00\rangle/\langle 11\bar{2}\rangle$ direction 16
3.4 The non-trivial unit cell of the zincblende structure 18
3.5 Comparison of wurtzite and zincblende crystal structure 19
3.6 The competing interactions which are responsible for the preference of wurtzite versus zincblende crystal structure 21
3.7 Stacking sequences of the different stacking fault types in zincblende and wurtzite 24
3.8 Atomic tetrapod and its structural parameters 27
3.9 Charge localization in an atomic tetrapod in ideal and non-ideal tetrahedral configuration 31
3.10 Polarization of the non-trivial wurtzite unit cell of Nitride–like, ideal, and non-Nitride–like crystal configuration 32
3.11 Schematic localization of the polarization charge planes in a wurtzite crystal 34
3.12 Quantum confined Stark effect in a quantum well of type-I band alignment 35
3.13 Quantum confined Stark effect in a series of layers with type-II band alignment 36

4.1 The double condensor system with the limit cases of ‘parallel’ and ‘convergent illumination’ 42
4.2 The projection system of the transmission electron microscope in imaging and diffraction mode 44
4.3 Schematic of beam path and intensity profile evolution in the STEM 49
4.4 Comparison of a conventional circular STEM and the DPC detector 51

5.1 Schematic sketch of the orientation of the nanowires towards the electron beam and optical axis for polarization measurements. 58
5.2 TEM images of the GaAs nanowire for the spontaneous polarization detection. 60
5.3 Charge distribution map of the transition from wurtzite to zincblende in GaAs with superimposed linescan profile. 61
5.4 TEM micrograph of the double twin structure. 63
5.5 DPC imaging of the double twin defect. 64
5.7 Raw data images of the electric field determination measurements in GaAs. 66
5.8 Uncorrected electric field across the GaAs double twin structure. . . 67
5.9 Corrected plot of the electric field across the double twin structure. . 68
5.10 High-resolution TEM micrograph of the beginning of the zincblende segment region in the GaP nanowires 70
5.11 Field map of the first five zincblende segments of the GaP nanowire 72
5.12 Electric field plot across the first five zincblende segments of the GaP nanowire 73
5.13 Typical intensity distribution of the diffraction disc after traversing a nanowire. 76
5.14 Datasets used for the simulation of the DPC signal. 78
5.15 Angular dependence of the deflection determination. 80
5.16 Angular dependence of the deviation of the measured from the factual rotation angle. 82
5.17 Simulation data: measured deflection plotted against the pattern shift. 82
5.18 Dependence of the detector response function on the overlap of diffraction disc and detector. 86
5.19 Accuracy of the quantitative shift determination for changed diffraction disc radii. 88

6.1 Compositional characterization of a GaAs nanowire with Mn added during growth. 93
6.2 Interface between nanowire crystal and Mn-Ga droplet. 95
6.3 High-resolution TEM of a partially crystallized Mn-Ga droplet. . . . 96
6.4 Compositional analysis of the catalyst droplet after growth termination in arsenic atmosphere 97
6.5 High-resolution TEM of the crystalline MnAs droplet resulting from growth termination under arsenic atmosphere. 99
6.6 Diffraction pattern of the topmost part of a GaAs nanowire with MnAs crystal on top. 100

B.1 High-resolution TEM overview over the segmented area of the GaP nanowire. 107
B.2 Raw data images of the electric field determination measurements in GaP. 108
B.3 Line scan plots of the raw DPC images from the GaP nanowire. . . . 109
B.4 Uncorrected electric field plot of the GaP nanowire. 109
C.1 Angular and shift dependence of simulated detector intensity. 110

List of Tables

3.1 Collection of structural parameters of GaAs and GaP as presented in different publications 29

A.1 Growth parameters used in the MOVPE growth of GaP nanowires. . 106

B.1 Measurement and specimen parameters used for the DPC measurements and field quantifications on GaAs and GaP nanowires. 107

Acronyms

Notation	**Description**
4H	stacking order with hexagonal symmetry and a periodicity of 4 layers
6H	stacking order with hexagonal symmetry and a periodicity of 6 layers
BF	bright-field
CBED	convergent electron beam diffraction
CCD	charge-coupled device
ccp	cubic close-packed
CVD	chemical vapour deposition
DF	dark field
DFT	density functional theory
DPC	differential phase contrast
EDX	energy dispersive X-ray spectroscopy
ESF	extrinsic stacking fault
fcc	face-centered cubic
FEG	field-emission gun
FFT	fast Fourier transform
FWHM	full width at half maximum
GaAs	gallium arsenide
(Ga,Mn)As	gallium manganese arsenide
GaN	gallium nitride
GaP	gallium phosphide
hcp	hexagonal close-packed
HR-TEM	high-resolution TEM

Notation	**Description**
InAs	indium arsenide
ISF	intrinsic stacking fault
MBE	molecular beam epitaxy
MnAs	manganese arsenide
MOCVD	metal-organic chemical vapour deposition
MOVPE	metal-organic vapour-phase epitaxy
QCSE	quantum confined Stark effect
SA aperture	selective area aperture
SNR	signal-to-noise ratio
STEM	scanning transmission electron microscopy
TEM	transmission electron microscopy
twin	twin stacking fault
UHV	ultra-high vacuum
VLS	*vapour-liquid-solid* growth
VS	*vapour-solid* growth
VSS	*vapour-solid-solid* growth
wz	wurtzite
XRD	X-ray diffraction
zb	zincblende

List of Symbols and Notations

Notation	Description	Unit
$[hk(i)l]$	crystal vector	
$\langle hk(i)l \rangle$	family of equivalent crystal vectors	
$(hk(i)l)$	crystal plane	
$\{hk(i)l\}$	family of equivalent crystal planes	
α	bonding angle between the vertical and any other bond of the atomic tetrapod	$^\circ$
a_{cub}	lattice parameter of the cubic unit cell	nm
a_{hex}	lattice parameter perpendicular to the principal axis in the hexagonal unit cell	nm
β	bonding angle between the basal plane forming bonds of the atomic tetrapod	$^\circ$
c_{hex}	lattice parameter parallel to the principal axis in the hexagonal unit cell	nm
$\Delta E_{\text{wz-zb}}$	formation enthalpy: energy difference between wurtzite and zincblende crystal	meV/atom
$\Delta I_{3,9}, \Delta I_{6,12}$	intensity difference of opposing segments of the DPC detector	
$\vec{E}$	electric field	$\frac{\text{MV}}{\text{m}}$
h	height of the atomic tetrapod, stacking height perpendicular to the basal plane	nm
I_3, I_6, I_9, I_{12}	intensity on a segment of the DPC detector	
I_{sum}	sum of the intensities from all four segments of the DPC detector	
j	current density	$\frac{\text{A}}{\text{m}^2}$

Notation	Description	Unit
κ	calibration factor of the DPC system with respect to electric fields	$\frac{\mathrm{V\,m}}{\mathrm{m}}$
κ_k	calibration factor of the DPC system with respect to diffraction disc shift	m
$\vec{k}_0$	shift vector in the diffraction plane	m
λ_e	electron wavelength	$\frac{1}{\mathrm{m}}$
L	camera length	m
φ_{rot}	rotation angle	$^\circ$
p	stacking periodicity	
P_{sp}	spontaneous polarization	$\frac{\mathrm{C}}{\mathrm{m}^2}$
q	net charge of an atom in a polar bond	C
ρ'	projected charge distribution	$\frac{\mathrm{C}}{\mathrm{m}^2}$
R_{d}	radius of the diffraction disc	m
R_{h}	inner radius of the DPC detector ring	m
σ	sheet charge	$\frac{\mathrm{C}}{\mathrm{m}^2}$
t	specimen thickness	nm
θ	electron probe convergence semi-angle	rad
u	internal-cell parameter: fraction of the atomic bond parallel to the crystallographic c axis in terms of lattice constant c_{hex}	

Straight roads do not make skillful drivers.

Paulo Coelho

1 Introduction

The research on semiconductor nanowires – tiny semiconductor crystals of sub-micron diameter and some microns length – has, although around only for about one and a half decade, already significantly diversified and developed. However, it has relied on characterization methods provided by electron microscopy since the earliest days, on the one hand as their sheer size keeps them out of reach of light-based imaging techniques and on the other hand due to their interesting structural properties down to the atomic level, which is one of the core capabilities of transmission electron microscopy when it comes to characterization. While the first years of research were governed mainly by exploration of their most fundamental properties and finding out the mechanisms of their synthesis, meanwhile already a lot of progress has been made towards the controlled growth and manipulation of their properties. Also, people quite early extended the activities beyond practising nanowire research for its own sake and started to seek ways to make use of their unique features for applications – both in the literal sense, i.e. the development of nanowire based devices and functionalization, as well as in the less applied sense, where the nanowires are used as a model system to investigate fundamental material properties.

Applying several transmission electron microscopical techniques, this thesis contains contributions to both of the fields mentioned above:

Concerning the research on fundamental material properties spontaneous polarization is a property unique to the wurtzite crystal structure, which was within the III–V semiconductors up to now only known to be present in the nitride based ones since they are the only ones that grow by default in the wurtzite crystal structure. Only since the discovery of nanowire growth this crystal structure has gotten available also for the other III–V semiconductor materials and provides a model system to access its properties experimentally and verify the theoretical calculations that have been done on such (up to then hypothetical) crystal structures. The first part of this work therefore contains the first direct experimental observation of the spontaneous polarization in the III–V semiconductor materials gallium arsenide (GaAs) and gallium phosphide (GaP).

More towards the application oriented side is the field of spintronics, i.e. the development of electronic devices that make use of the electron spin instead of the charge as the fundamental property to transfer, process and store information. This field requires the fabrication of ferromagnetic device structures that allow to

generate and detect spin polarized electrons within the semiconductor materials it should integrate with. One candidate for such a ferromagnetic material is manganese arsenide (MnAs) which includes semiconducting and ferromagnetic properties within one material and is hence considered to be an important building block with respect to the development of spin-based electronic devices. The second part of this work is the characterization of such MnAs nanocrystals that have been grown on top of GaAs nanowires.

The document at hand is organized in five main chapters of which the first three describe the theoretical and experimental framework in which this work took place, while the remaining two present the results that have been achieved.

Chapter 2 gives an introduction into the topic of semiconductor nanowires, about their synthesis, and their properties of interest, with a special focus on III–V semiconductor nanowires and especially gallium arsenide (GaAs) and gallium phosphide (GaP) nanowires. Since one of the features of semiconductor nanowires is their polytypism, i.e. the possibility to adopt different crystal structures in Chapter 3 the occurring crystal structures and some of their properties and implications are discussed. Chapter 4 explains the transmission electron microscope – the experimental instrument used – and the analytical methods available in this device which were employed in this work.

The first experimental chapter, Chapter 5, presents the experimental evidence of spontaneous polarization in gallium arsenide and gallium phosphide. In addition, based on the issues that arose with the quantitative evaluation of the measurements, the properties and experimental limitations of the differential phase contrast (DPC) microscopy technique are discussed. Finally in Chapter 6, the second experimental chapter, the characterization of samples from a growth study on the route towards the inclusion of manganese arsenide (MnAs) is described.

2 III–V Semiconductor Nanowires

Semiconductor nanowires are quasi-one-dimensional nanocrystals with a typical diameter around 100 nm and lengths up to several micrometers. Basically, objects of such physical dimensions can be created in two different ways, either by eroding material from a bulk crystal through etching or milling techniques – which is referred to as *top-down* approach [1, 2] – or by techniques where a crystal of the desired shape is synthesized from molecular precursors, hence the latter is called *bottom-up* process.[3] Although sometimes also structures produced in top-down techniques are called 'nanowires', this term typically refers to crystals that have been grown in a bottom-up process which is also how the term will be used in the further reading.

In this chapter a general overview over the growth, properties, and applications of semiconductor nanowires, with a focus on III–V semiconductors and especially GaAs will be given.

2.1 Nanowire Growth

2.1.1 Growth methods and substrates

All crystal growth or epitaxy techniques have in common that the atoms needed to build the crystal somehow have to be supplied and transported to an already existing seed crystal where they can be attached to the present material which makes the crystal grow. In general, this supplying phase can be a liquid where the precursors are dissolved or some more or less dense precursor vapour. Above that the different epitaxy techniques can be distinguished regarding if the atoms needed for the crystal growth are supplied in multi-species molecules which act as carrier or in such where each molecule consists of only one single atom species.

Generally nanowires can be grown with any epitaxy technique as long as it allows to establish a suitable nanowire growth mode (cf. Section 2.1.2) for the desired material system. However, de facto III–V nanowires, as well as most other semiconductor nanowires are grown either via *molecular beam epitaxy* (MBE) or one of the various *chemical vapour deposition* (CVD) techniques.

Molecular beam epitaxy

Molecular beam epitaxy growth happens, as the name suggests, by directing beams of the growth molecules onto the sample substrate within a *ultra-high vacuum* (UHV) chamber. The ultra-high vacuum serves two purposes: First it provides an ultra-clean environment that is nearly free of contaminations which could get included into the crystal and second it ensures, that molecules that travel in the chamber have a mean free path in the order of the dimensions of the chamber, which means they are unlikely to collide with each other but travel straight until they hit any surface within the chamber. On one side of this chamber the growth substrate is mounted on a rotatable sample holder stage that allows to heat the sample up to around 1000 K and on the opposing side effusion cells are located which contain highly pure precursor materials in solid or liquid form. Mechanical shutters in front of the cells allow to abruptly switch on and off single molecular beams which enables to grow samples with very sharp compositional changes down to atom layer precision.[4] The chamber walls between the sample holder and the effusion cells are lined with liquid nitrogen cooled shrouds where molecules that re-evaporated from any surface condensate and therefore get caught, which helps to prevent contamination of the grown sample.[5]

As the precursor materials are heated in the effusion cells they evaporate or sublimate in the case of GaAs as Ga_2 and As_2 or As_4 molecules which are emitted from the cells towards the sample as molecular beams. Where the molecules hit the sample surface they decompose into single atoms and get included into the crystal. The parameters to influence the growth process are – beside chamber specific parameters as the vacuum which are normally kept unchanged – the beam fluxes of the different growth species and the temperature of the growth substrate.[4, 6]

Metal-organic chemical vapour deposition

From the chemical vapour deposition techniques especially the metal-organic variants are commonly used for nanowire growth. A CVD system basically consists of a so-called reactor tube through which gas can flow via an input and an exhaust port and a valve and pipe system in which a carrier gas (typically H_2 or N_2) and the various precursor gases are mixed before they are passed into the reactor. There exist different reactor designs but they all have in common that the gas mixture enters the reactor at one end, flows across the growth substrate which is located on a heatable and rotatable sample stage and is pumped out of the reactor at the other end. Typically the growth is done at pressures close to atmospheric pressure.

In the metal-organic variant of the CVD technique the precursors of the desired atomic species are bound in organic molecules, hence the name *metal-organic chem-*

ical vapour deposition (MOCVD) or *metal-organic vapour-phase epitaxy* (MOVPE). For the growth of GaAs and GaP for example, gallium is bound in trimethylgallium ($Ga(CH_3)_3$) or triethylgallium ($Ga(C_2H_5)_3$) while arsenic and phosphorous are supplied via the inorganic arsine (AsH_3) and phosphine (PH_3) or some organoarsenic and -phosphenic compounds such as trimethylarsine ($(CH_3)_3As$) and tert-butyl phosphine ($(CH_3)_3CPH$). In the growth reactor the molecules react such that the gallium, arsenic, and phosphorus atoms are set free to be included into the crystal and the remnant parts of the molecules rearrange to new compounds that are carried away towards the exhaust by the gas flow. In MOCVD there are more parameters than in MBE which can be tuned: The temperatures of both, the substrate itself and the gas flow can be varied as well as the overall gas flow and pressure and the partial pressures of the particular precursor materials.[4, 7]

Due to their high scalability and fast growth rates compared to MBE the MOCVD techniques are the industrial quasi-standard for the growth of epitaxial semiconductor thin films. However they have also the drawback that due to the organic carrier gases a significant incorporation of carbon and oxygen atoms into the crystal occurs which act as so-called 'unintentional doping'.[4, 7, 8] Therefore MBE is especially considered superior where materials of very high purity are needed.[4]

Growth substrates

For the growth of semiconductor nanowires usually semiconductor wafers are used as substrates. Over a long time the growth was performed on the same substrate types that also were used for the growth of 2D layers, which is in most cases identical to the material system that should be grown onto it. Over the recent years many groups have switched to silicon as growth substrate which is cheaper and easier available than the specialized III–V growth substrates but does not have negative influence on the nanowire quality as the nanowire–substrate interface does not suffer from lattice mismatch problems (cf. Section 2.2). Actually, the growth on silicon even offers the perspective of an easier integration of III–V nanowire based devices into existing silicon based production environments.[9–11] In addition to the self-evident growth on semiconductor wafer substrates also more exotic materials such as glass[12, 13] and graphene sheets[14, 15] have been used to grow nanowires on. Heurlin *et al.* [16] even have shown the growth of III–V nanowires without any substrate from gold nanoclusters which are fed into the gas flow of a MOVPE reactor.

2.1.2 Growth modes

In the growth kinetics of epitaxial layers, the surface perpendicular to the one on which the growth takes place, is the surface that is the slowest growing crystal facet for a given set of growth conditions.[3] Starting from a seed crystal with facets of

different surface energies and providing the necessary precursor materials the new material will adsorb to all surfaces with different growth rates which are related to the formation enthalpies specific to those surfaces. As one of the core properties of crystals is their high symmetry there are always several surfaces of different orientation but with the same surface energies, which makes the crystal expand primarily perpendicular to the fastest growing surfaces. What remains is the surface with the slowest growth speed and whenever a small crystal island forms on this surface, it will have faster growing facets than the one it is sitting on and therefore expand parallel to the surface until another layer was formed. By this growth mode, depending on the crystal symmetry, only bulk or two-dimensional crystals can form.

To form one-dimensional crystals instead, this symmetry has to be broken somehow, leaving only one preferential direction in which growth occurs faster than in the other ones.[17–19] To achieve this, depending on the material system different possibilities exist, which will be called *growth modes* in the following.[19, 20]

Catalyst-free growth modes

In materials with monoclinic, rombohedral, tetragonal, and trigonal/hexagonal symmetry, whose crystal structures have a single principal axis, it can be sufficient to use this anisotropy and chose conditions that favour the growth along this principal axis. This mode is referred to as *vapour-solid* (VS) growth as the material is incorporated into the crystal directly from the gaseous precursor phase. In this mode there is often also a significant growth on the side facets as the growth rates in the different directions do not differ too much, which leads to rather short, pillar-like structures. Those are quite common among III–nitride nanowires[21, 22], but also occurrences in the case of GaAs [23–27] and InAs [28] have been reported.

However, even for such materials a size-limiting element is needed at the initial stage of the growth process to prevent the growth of a whole surface area and promote the growth of a needle-like structure instead. This is often achieved by a mask material – usually some oxide layer – where the crystal can only grow at spots where the mask material has holes that reveal the underlying substrate material. As soon as a small stub has been grown the further process works just by the top facets of the crystal stub being the fastest growing surfaces. This template based mode is therefore sometimes referred to as *selective area growth* [10, 25–27] and is one of the two typical growth modes of the hexagonal crystal lattice based III–nitrides.[21, 29–31] At the same time the mask material does not only limit the places where the initial growth can occur but also provides a low sticking coefficient for the precursor materials. Therefore they can easily either diffuse towards the nanowire crystals to get incorporated there or desorb from the surface and hence reduce parasitic growth on the mask surface.

Catalyst-mediated growth

The III–V semiconductors, except for the III–nitrides, as well as the group–IV semiconductors silicon and germanium, grow in cubic crystal structure with a *face-centered cubic* (fcc) lattice, which has four equivalent symmetry axes, as described in detail in Section 3.1. Without any additional measures the crystal would grow along all four axes simultaneously, leading to a volume crystal. Therefore some element is necessary that reduces the symmetry by favouring one of those symmetry axes over the other ones. Typically this is reached by a nanometre sized particle which acts as a physical and/or chemical catalyst to ease the incorporation of the growth species into the crystal leading to a significantly faster growth of the crystal right below the particle compared to other spots on the sample. The particle helps to decompose the precursors and to transport the growth atoms to the crystal growth front, which is situated directly below the particle. As a consequence the particle is always sitting on top of the nanowire as it is lifted upwards by the growing crystal.

Sometimes this catalyst particle is a solid crystallite[17, 32–35] but typically it is a liquid droplet. The former is called *vapour-solid-solid* (VSS) growth, as the growth species are transported from the gas phase via the solid particle to the crystal phase, while the latter and most common one is referred to as *vapour-liquid-solid* (VLS) growth due to the fact that the growth species are carried to the growth front through the liquid droplet. The droplet can consist either of an eutectic formed by a metal and one of the growth species or just by one of the growth species.

2.1.3 The *vapour-liquid-solid* growth

Gold-catalysed growth

The eutectic or *metal-catalysed* growth mode was first discovered in the 1960s by Wagner and Ellis[36, 37] – back then for the growth of micron-wide so-called silicon 'whiskers' from a silicon-gold eutectic – who already created the term *vapour-liquid-solid* growth, and theoretically described by Givargizov [38]. In this growth mode the metal alloys with one of the growth species, in the case of the III–V semiconductors with the group–III material, and does – in theory – not get incorporated into the nanowire crystal but acts only as a physical catalyst to enhance the incorporation of growth atoms into the crystal. Although nowadays other metals are used as alloy material as well,[39] gold is still the most widely used one.

The theoretical description of III–V semiconductor based nanowire growth has especially been carried out by Dubrovskii [40–49], Harmand [50–52], and Glas [53–55]. For the gold-catalysed growth of GaAs nanowires as schematically depicted in Figure 2.1 a gold film with typically sub-nanometre thickness [56, 57] is evaporated onto a substrate wafer – either native GaAs or Si – before loading it into the growth chamber. There the substrate is heated to temperatures above 500 °C which makes

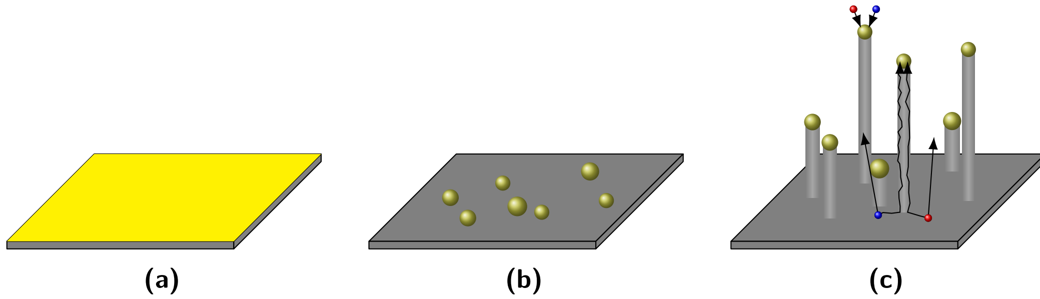

Figure 2.1: Schematic drawing of the gold-catalysed growth of GaAs nanowires: (a) A substrate wafer (grey) covered with a thin gold film (yellow) is put into a growth chamber. (b) Prior to growth the wafer is heated to around 600 °C, which causes the metal to form randomly distributed eutectic droplets with Ga from either the wafer or from already provided growth species. (c) Ga and As supplied from the gas phase get included into the nanowire through the eutectic droplet. Atoms that impinge on the substrate or the nanowire side walls either desorb or travel across the substrate and along the nanowire side walls towards the droplet.

the gold form eutectic alloy droplets with gallium from the wafer or supplied from the gas phase in the case of a Si wafer. Those droplets are randomly distributed and act as nucleation seeds for the further growth of nanowires.

Self-catalysed growth

Although it had been shown before on MOVPE-grown InAs nanowires[60, 61], the MBE growth of GaAs nanowires by Colombo *et al.* [58] is regarded as the foundation of the *self-catalysed* nanowire growth mode of III–V semiconductors. The central feature of this growth mode is a liquid droplet of the group–III material on top of the nanowire crystal that promotes the VLS growth in the same way as the eutectic droplet in the metal-catalysed growth.

For this type of nanowire growth either a native substrate wafer is covered with silicon dioxide (SiO_2) or a Si wafer with its native oxide is used. At a thickness below 30 nm the SiO_2 provides pinholes that serve two purposes: SiO_2 exhibits different sticking coefficients for the group–III and group–V materials, allowing the group–III atoms to diffuse along the oxide surface while most of the group–V atoms arriving at the oxide surface desorb again.[62–65] As there are few group–V atoms on the surface to bind to, the group–III atoms can move freely on the oxide surface until they desorb as well or get trapped at one of the pinholes. After some incubation time this will lead to the formation of group–III droplets at the pinholes that will then collect atoms of both species arriving at their surface and guide them to the droplet-crystal interface where they get incorporated into the crystal.[58, 64]

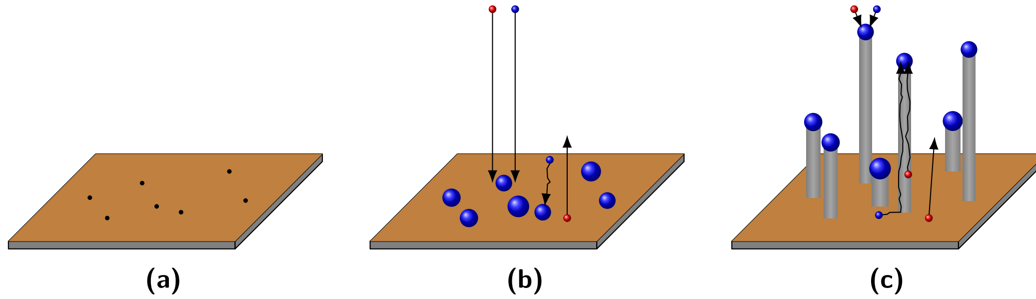

Figure 2.2: Schematic drawing of the self-catalysed growth of GaAs nanowires (based on [58]): (a) Starting point is a substrate wafer covered with SiO_2 (brown) and small pin holes (black dots) due to etching. (b) With the start of the growth process both growth species are provided. Ga that hits the SiO_2 surface can migrate to the pinholes to form droplets while As does desorb again. (c) After the nanowire growth has started the Ga is fed to the droplet either directly from the gas phase or from the substrate and the nanowire side walls. For the As supply only direct impingement on the droplet and diffusion from the nanowire side walls is important, whereas diffusion of As from the SiO_2 does only seem to play a minor role.[59]

The second purpose of the pinholes is to provide an epitaxial relationship between the nanowire and the substrate crystal below the oxide to obtain nanowires that are all oriented the same way with respect to the crystallographic orientation of the substrate.[66]

Self-catalysed grown nanowires are to some extent considered superior to metal-catalysed ones as via the metal-catalysed growth small amounts of the metal atoms can get included into the nanowire crystal,[67] where they are suspected to form deep level traps [23] and therefore influence luminescence properties.[68]

2.2 Properties and Applications

Most of the properties that make nanowires interesting subjects for materials science and application oriented research is more or less directly connected to their high aspect ratio, i.e. the combination of a diameter in the sub-micrometre range with lengths of several micrometres. As such many of their material properties can differ significantly from the properties of the same material's bulk form, which made nanowire research a growing field over the recent 15 years (cf. Figure 2.3).

Their pure diameter makes nanowires quasi–one-dimensional objects as many characteristic quantum-mechanically and mesoscopically relevant length scales such as the Bohr radius for excitons and the mean free paths of electrons and phonons lie

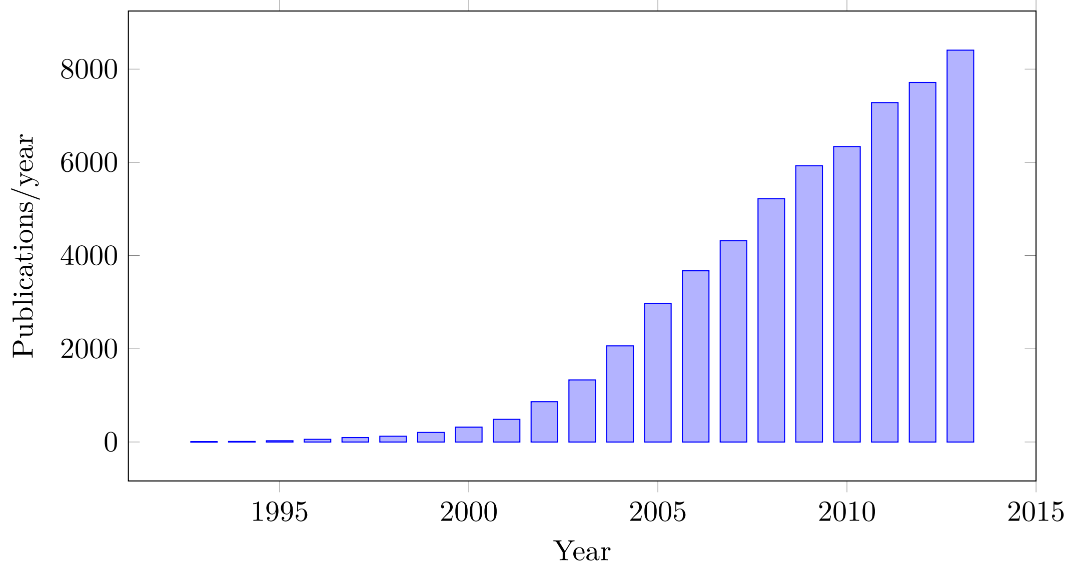

Figure 2.3: The number of publications per year that have 'nanowire' or variations thereof as their topic. With only a few publications (below 200 per year) in the 1990's their number started to increase significantly around 2000 and is increasing still nearly linearly since then (based on publication statistics taken from the *Web of Science Core Collection* with topic search for `*nanowire*`).

within the same range as their diameter. Thus nanowires are considered to be ideal objects for the exploration of mesoscopic phenomena that require a size constriction in two dimensions.[69] Maybe the most spectacular finding in this branch was the possible, yet still debated,[70] evidence of Majorana fermions using a device based on a nanowire coupled to a superconductor.[71]

From an application-oriented point of view especially the high surface-to-volume ratio that comes with the aspect ratio seems to be the base for the most promising research. One topic that is already quite developed is chemical and biological sensing, where the comparatively large surface is used to detect even single molecules in liquid or gas flows.[72–75] Another promising field are opto-electronics: With nanowire-based solar cells it has been shown that the special form of the nanowires allows to overcome fundamental efficiency limitations of planar solar cells.[76, 77] In terms of light generation, white light [78] as well as multicolour [79] light-emitting diode structures that work without a converting phosphor have been fabricated by including materials of different compositions into one nanowire.[80] Besides that nanowires are also seen as candidates to overcome the limitations given by Moore's Law in future electronics.[81, 82]

Above that the small diameter of nanowires allows for material properties that do not occur in the bulk form of the same material. Those properties are often in some way connected to the crystal structure which in nanowires is less affected by some limitations compared to the bulk crystal, e.g. the lattice mismatch between the materials of a heterostructure.[9, 83, 84] Here especially crystal structure polytypism[46, 85–87] – i.e. the possibility to have different crystal structures within one crystal, which will be covered more detailed in Section 3.1 – has to be mentioned as this phenomenon is subject to the present work. In the III–V semiconductors which – except for the III–nitrides – have a bulk crystal structure of zincblende nanowires can also exhibit wurtzite crystal structure. As such crystal structures got only available with nanowires for many materials, there is an ongoing hunt for those materials properties which have up to now only been subject to theoretical considerations.

3 Crystal Structures and Crystal Structure Related Effects

3.1 Zincblende and Wurtzite Crystal Structure

All III–V-semiconductors have in common that they crystallize in a close-packed configuration, i.e. their atoms are arranged in a way that a given number of atoms occupies the least possible volume.[88] For the bulk form of the III-Nitrides this is the *hexagonal close-packed* (hcp) stacking while the III-Arsenides, III-Phosphides, and III-Selenides take a *face-centered cubic* (fcc) (also known as *cubic close-packed* (ccp)) configuration in their bulk form. In both cases the lattice has a diatomic base consisting of a group–III and a group–V atom, however, for an easier description the base will be omitted for the time being, treating the situation as stacked hard balls.

3.1.1 Stacking orders

For the non-trivial unit cell of the hcp structure as depicted in Figure 3.1a one starts with six balls arranged as a regular hexagon in a plane with a seventh ball in its center. In this configuration every two neighbouring balls in the hexagon form a triangle together with the central ball. A second layer of three balls is then stacked onto the first one in a way that the balls in the second layer are placed above every other of those triangles. Finally a third layer consisting of seven balls is placed on top so that it corresponds in its orientation with the first layer. It can be seen easily that this structure is rotation-symmetric with a three-fold symmetry around the normal axis of the stacking planes and has three equivalent symmetry axes which are situated at 120° angles within the stacking planes which was already discovered by Kepler [89] in the early 17th century.[88] Also, the stacking does have a different symmetry along the axis perpendicular to the stacking planes, which makes this a principal axis of the structure.

To describe the crystal directions of such a configuration one often uses a system of four instead of three Miller indices to determine lattice vectors and planes in hexagonal symmetric crystal structures. This indexing system consists of three equivalent unit vectors $\vec{a}_1$, $\vec{a}_2$ and $\vec{a}_3$ that are of equal length and arranged in 120° angles within the three-fold symmetric stacking plane. A fourth unit vector $\vec{c}$ which normally has not the same length as the $\vec{a}$ vectors is oriented perpendicular to the

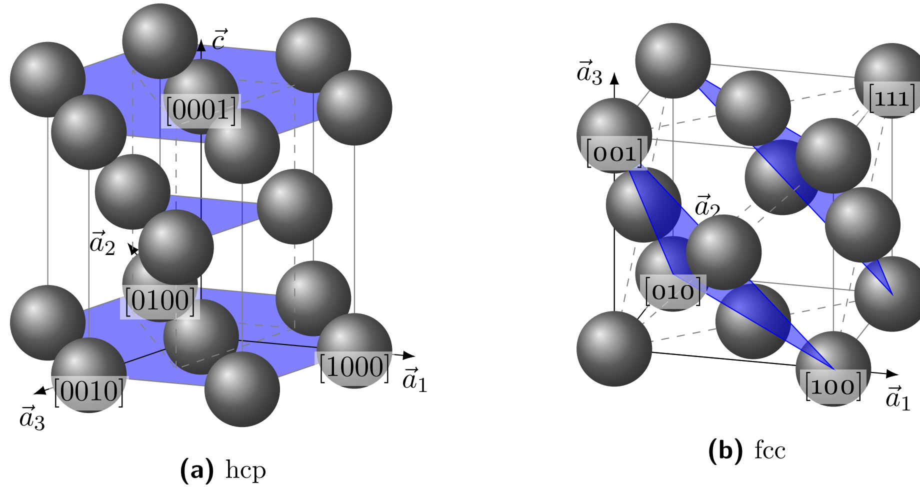

Figure 3.1: The non-trivial unit cells of the hexagonal close-packed (hcp) and face-centered cubic (fcc) structure with the axes of their indexing systems. The balls representing the stacking units are reduced in size to allow for a better view on the structure. The blue planes denote the lattice planes in which the structures have hexagonal symmetry, i.e. the hexagonal {0001} and the cubic {111} planes.

plane formed by the $\vec{a}$ vectors. This is in contradiction to the three-index notation system that is used for cubic crystals, where the unit vectors $\vec{a}_1$, $\vec{a}_2$ and $\vec{a}_3$ are perpendicular to each other and hence form a Cartesian coordinate system. Although a four-index system is over-determined and therefore contains some redundancy it allows to denote lattice planes that are perpendicular to a certain lattice vector by the same set of indices, which would not necessarily be true in a three-index notation. For the crystal systems used in this work the [0001] or c-axis, i.e. the symmetry axis of the hexagonal crystal is equivalent to the $\langle 111 \rangle$ axes of the cubic indexing system; the spatial correlation between both indexing systems for the axes that lie in the plane perpendicular to this axis can be seen in Figure 3.2b.

In the face-centered cubic case the close-packing is less obvious. While first findings about the tetragonal nature and therefore about possible hexagonal configurations of close-packed stackings had already been made by Hooke [90] and Huygens [91] in the 17th century and the hexagonal structure was finally recognized by Wollaston [92] in the early 19th century, it took another 70 years until Barlow [93] found in 1883 that the close-packing of spheres could also produce an fcc structure.[88] Wollaston even had described the stacking configuration that results in the fcc structure but hadn't recognized its implications. Considering a unit cube of edge length 1 the face-centered cubic structure is produced by placing an atom at every corner of the cube as well as in the center of every side face – hence the name of

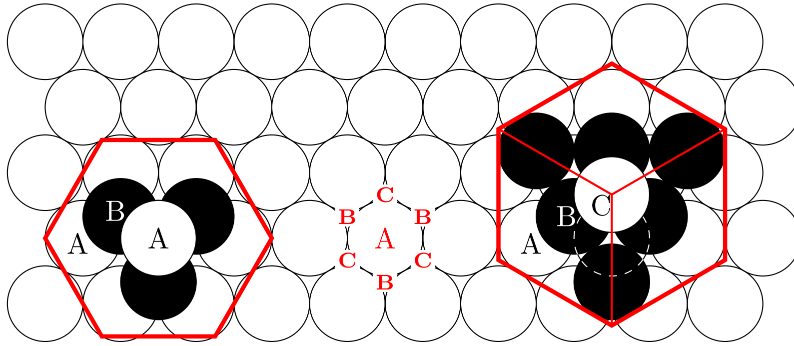

(a) Stacking sequence of hcp (left) and fcc (right) built on the same base layer. Between them the possible placements for the layer stacking are indicated with red characters. The hcp structure with ABA sequence only occupies two of the possible positions in alternating order while the ABC sequence of fcc on the right cycles through all three positions. The red frames around both stackings are the unit cells projected along their [0001] (hcp) and [111] (fcc) axis, respectively. (redrawn based on [94] with additional information from [95, 96])

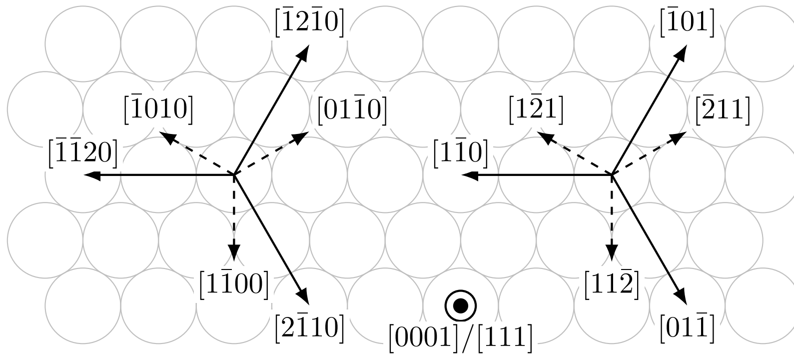

(b) The two crystal direction families of lowest order which are perpendicular to the [0001] axis in hcp (left) and the [111] axis in fcc (right), respectively. The indexed arrows indicate only the directions, but not necessarily the correct lengths of the vectors. (redrawn from [97])

Figure 3.2: The stacking sequence and important crystal directions of hexagonal close-packed and face-centered cubic stacking.

the structure – as depicted in Figure 3.1b. If one now does not consider one face of the cube as the base plane of the stacking, but the (111) plane, which is the plane that intersects with all three coordinate axes at a value of 1, one finds that the balls have the same hexagonal arrangement as the base plane of the hcp structure.

A direct comparison of both stackings based on the same base layer is shown in Figure 3.2a. Starting from the first layer (A) in both structures the second layer is shifted such that its balls are located above the center of a triangle formed by the

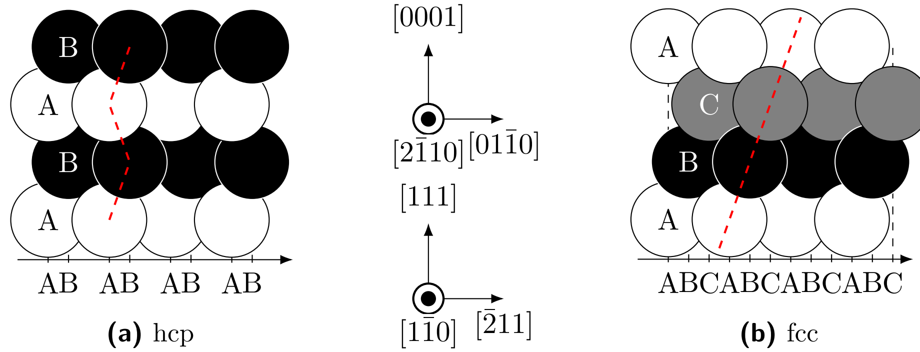

(a) hcp

(b) fcc

Figure 3.3: hcp and fcc stacking seen along a $\langle 1\bar{1}00\rangle/\langle 11\bar{2}\rangle$ direction. The hcp stacking is characterized by a zig-zag like appearance while fcc forms inclined rows, in both cases indicated by dashed red lines. At the bottom the projection of the ball center positions onto one line is indicated. Between both images the seen crystal orientations are indicated in hexagonal and cubic notation.

elements of layer A. As depicted in the center of Figure 3.2a, there are six such valleys around every ball of which only three can be occupied by the neighbouring layer, hence there are two possible ways to place a subsequent layer on an existing one. In the following those positions will be referred to as B and C where B always denotes the position that is occupied by the second layer and C is then determined as the remaining one accordingly. The first two layers of the stacking sequence of hcp and fcc are identical, whereas their third layer makes the fundamental difference: in the hcp case the stacking order is $ABAB$, i.e. the sequence repeats itself after two layers omitting the C position while for fcc the stacking makes use of all three positions repeatedly, therefore the stacking order is $ABCABC$.[88]

The situation gets even more clear when viewing both stackings from the side through a $\langle 2\bar{1}10\rangle$ (hcp) or $\langle 1\bar{1}0\rangle$ (fcc) crystal direction, as depicted in Figure 3.3: In this projection the elements in one layer are not situated centered in a valley between the elements of their adjacent layers. Instead, concerning the connection line between two neighbouring balls of one layer, there are two equally spaced off-center positions where the ball of the subsequent layer can be situated. In the hcp case the directly adjacent balls of subsequent layers form a zig-zag line as only two of the three possible positions are used. However, for fcc the occupation of all three positions appears as an inclined sequence of balls as indicated by the dashed red line in Figure 3.3b.

Leaving out the C layer in the hcp structure fundamentally influences the symmetry compared to the fcc case: starting in the A layer with a triangular arrangement of three balls side length and a B layer of two balls side length, then in the C layer

of the fcc structure a single ball can be placed on top of the stack such that an equilateral pyramid or regular tetrahedron is formed. All four {111} side walls of the tetrahedron show an identical arrangement of balls, thus the structure has four equivalent symmetry axes arranged in a tetrahedral configuration. In contrast, as already mentioned above, hcp has three equivalent axes that are situated in the (0001) plane and a forth axis of different symmetry along its normal vector, i.e. the [0001] direction.

3.1.2 Atomic configuration

The zincblende and wurtzite crystal structures have, as already mentioned above, a diatomic base, i.e. the hard balls used up to now represent in fact a set of two atoms. Their orientation with respect to the lattice can be described in two different but equivalent ways: either an atom pair is situated at every lattice point that was occupied with a simple ball up to now or the whole structure consists of two interlaced sublattices (both either hcp or fcc) that are shifted via a displacement vector $\vec{u}$. In the zincblende case $\vec{u} = \frac{a}{4}(1, 1, 1)$ while in wurtzite it is $\vec{u} = \frac{3}{8}\vec{c} = \frac{3}{8}[0001]$.[98] As (111) and (0001) represent the same basal plane, in both cases those planes are built by two atoms vertically stacked onto each other. Above that in the zincblende and wurtzite case the base consists of two different atomic species – a so-called heteroatomic base. If the base was homoatomic instead, this would lead to the diamond crystal structure for fcc and the hexagonal diamond or lonsdaleite [99–101] in the hcp case. As a result of the heteroatomic base, both zincblende and wurtzite do not have an inversion symmetry as compared to the pure fcc and hcp stacking.[102]

Based on the cubic unit cell of fcc (Figure 3.1b), to form the zincblende structure, atoms of one species are situated at the fcc positions of the unit cube. The atoms of the second species are then located in four of the eight interstitial positions between them (cf. Figure 3.4). Each atom in the crystal has a coordination number of 4, which means it is sp^3-hybridized and has four nearest neighbours that are covalently bound. Due to the heteroatomic base every atom of species A is the center of a tetrahedron formed by four atoms of species B and vice versa, as indicated by the orange tetrahedra in Figure 3.4. With the hexagonal wurtzite the situation is more obvious as one of the faces of the bonding tetrahedra lies within the basal plane of the stacking (cf. Figure 3.5a).

In Figure 3.5 a direct comparison of wurtzite and zincblende is shown with zincblende rotated such that the $[\bar{1}\bar{1}\bar{1}]$ axis is parallel to the wurtzite [0001] axis which is also the growth direction of nearly all semiconductor nanowires. Both structures are drawn on the same hexagonal bottom plane contained by a central atom and six surrounding ones.

Here several features that both structures have in common get visible:

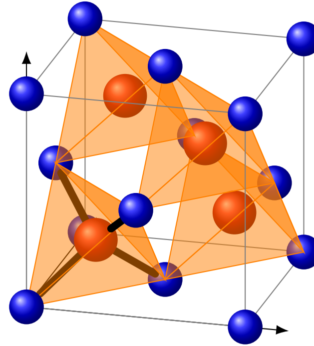

Figure 3.4: The non-trivial unit cell of the zincblende structure: atoms of one species (blue) are sitting at the fcc positions with atoms of the second species (red) in four of the eight interstitial positions between them. The orange tetrahedra represent the coordination configuration of the red atoms. In the bottom left the bonding configuration around one red atom is drawn.

The [0001] as well as the $\langle 111\rangle$ direction are polar directions [103] which are characterized by the fact that on any plane perpendicular to those axes only one species of atoms will be found. In a real crystal the topmost layer of blue atoms would not exist as a crystal surface since each of the atoms would have three unsaturated or dangling bonds. This configuration is energetically less favourable than the configuration of the red atoms directly below with only one dangling bond per atom. As a consequence single atomic layers cannot occur separately along the polar axes, but will always come up in pairs of a group–III and a group–V atomic layer, which is in contrast to e.g. the non-polar $\{11\bar{2}0\}$ planes where atoms of both species are arranged within the same layers. Along the polar directions – which are the ones examined in this thesis – a monolayer can therefore be considered to consist of two homoatomic sublayers.

As another consequence of the polarity in III–V semiconductors such as GaAs the $\{111\}$ and $\{\bar{1}\bar{1}\bar{1}\}$ surfaces of the crystal are terminated by different atomic species, namely group–III atoms on the $\{111\}$ and group–V on the $\{\bar{1}\bar{1}\bar{1}\}$ surfaces. In the field of the wurtzite structured III-Nitride semiconductors the polar surfaces therefore are also known as e.g. Ga-face and N-face (for a GaN semiconductor).[104] For growth substrates the surfaces are often also named $\{111\}A$ and $\{111\}B$ instead, to denote the wafer sides where the crystal is terminated either by a surface of group–III (A) or group–V (B) atoms. Since the native substrates for nanowire growth have typically $\{111\}B$ surfaces [61, 105–107], the occurrence of nanowires grown in $\langle 111\rangle A$ direction is rather rare [61, 108, 109] and in most cases considered parasitic,[105, 110] the exact directionality will be omitted in the further reading and $\langle 111\rangle$ will refer to the $\langle 111\rangle B$ direction unless explicitly specified elsewise.

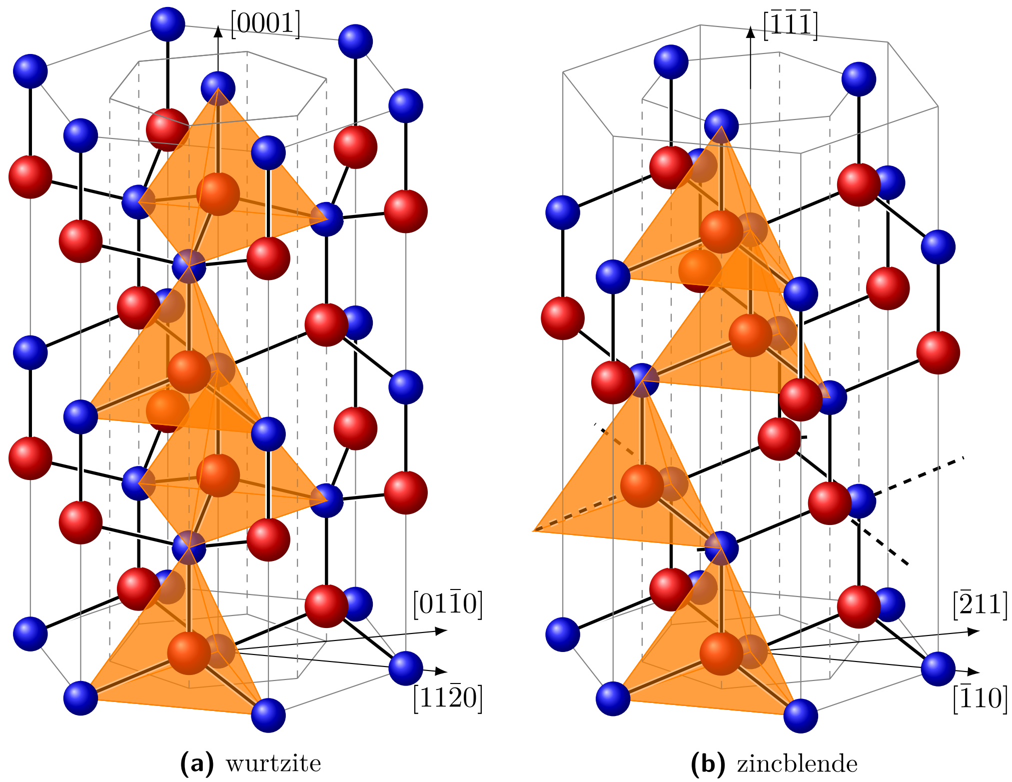

(a) wurtzite **(b)** zincblende

Figure 3.5: Direct comparison of Wurtzite and zincblende crystal structures along the [0001] and [111] axes, respectively. The structures contain four monolayers, which correspond to two stacking sequences in wurtzite and four thirds in zincblende. All bonds connecting neighbouring atoms within the bounding box are drawn. Dashed bonds in (b) denote bonds that belong to an atom within the bounding box but penetrate the outer surface of the box. The orange tetrahedra represent the coordination configurations of the one red atom of each layer.

Beside the polarity also the inversion asymmetry is easily visible in Figure 3.5 as under an inversion of the [0001] or ⟨111⟩ axis the structures will look the same but with the positions of the two atom species switched.

In the direct comparison the differences caused by the stacking orders of hcp and fcc get cleanly visible through the orange bonding tetrahedra. The tetrahedra in the zincblende structure (Figure 3.5b) are all oriented in the same direction and only translated laterally while in wurtzite the tetrahedra of consecutive layers additionally have to be rotated in the (0001) plane by 180°. At this point the higher symmetry of the zincblende structure comes into play again as it would be possible to rotate the structure such that another facet of the tetrahedra would form the bottom face and still have the tips of all tetrahedra point upwards. For the wurtzite structure, where only the tetrahedra of the next-nearest neighbours share the same orientation, such a transformation is not possible, leaving the [0001] axis as the only principal axis.

Another difference is illustrated by the dashed bonds in Figure 3.5b which denote bonds from atoms within the bounding box to atoms that are not drawn since they are outside the box. In the wurtzite structure the bounding box drawn in Figure 3.5a is self-contained, i.e. every atomic bond that originates at an atom within the box also ends at another atom within the box. This is not the case in zincblende where some bonds protrude the bounding box side surfaces. Enlarging the bounding box to the next larger configuration by adding an additional layer of atoms around the current bounding box would eliminate these open bonds but at the same time create new ones at other places which means that for zincblende there cannot be a self-contained hexagonal bounding box.

3.1.3 Polytypism

From the hexagonal basal plane of both structures along the considered axes it appears obvious that it should be possible for the crystal to switch between zincblende and wurtzite structure without causing significant disturbance – a phenomenon that is known as *polytypism*.[46, 85–87, 111] However, this is not the case for most III–V semiconductors and all but the Nitride-based ones occur only in zincblende structure in their bulk form and under 'normal' ambient conditions. Only some publications report the generation of bulk wurtzite GaAs after a treatment with pressures of several tens of gigapascal.[112–114] Another group that analysed the properties of a wurtzite GaAs layer frankly admits that the growth of this layer was due to pure luck and could not be explained nor reproduced.[115] The III-Nitrides take again a special role here as those are the only III–V semiconductors that can have stable phases of both wurtzite and zincblende crystal structure in their bulk form.[116]

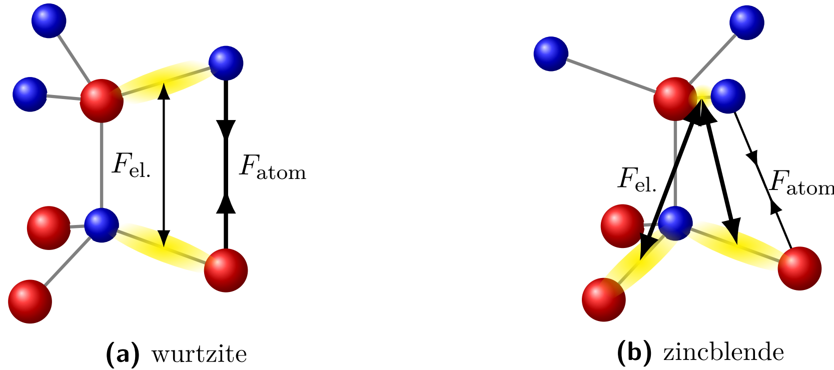

(a) wurtzite **(b)** zincblende

Figure 3.6: The competing interactions which are responsible for the preference of wurtzite versus zincblende crystal structure. The two involved atomic species are drawn in blue and red, the bonding orbitals are symbolized as yellow clouds on some bonds. The resulting forces F_{atom} and $F_{el.}$ are denoted by arrows with the arrow tips indicating the force direction and their thickness symbolizing their relative strength. In (b) the second F_{core} vector between the bottom left red and the top center blue atom was omitted for clarity. (based on [118])

Energetics

Per definition of the $ABAB$ stacking order the wurtzite structure is invariant under a translation by an even number of monolayers along the [0001] axis while for zincblende a translation by multiples of three monolayers is needed. Seen from any atom within the crystal lattice this means that along the [0001] direction the next atom of the same species is only two monolayers away in wurtzite while it is separated by three monolayers in zincblende.[98, 117] This difference in vicinity between both structures influences the electrostatic interaction between neighbouring monolayers. Depending on the electronegativity differences of the involved elements this leads to attractive and repulsive force between the atoms of the neighbouring monolayers.

The difference in electronegativity causes the binding orbitals to be not evenly distributed between the two bound atoms but to be located more closely at the one with the higher electronegativity, which makes this atom appear 'charged' negatively with respect to the less electronegative one. The two competing interactions that come into then are the attractive force F_{atom} between the atoms of different electronegativity of neighbouring monolayers and the repulsive force $F_{el.}$ between the binding orbitals of those monolayers. The possible configurations are depicted in Figure 3.6 on a molecule consisting of one diatomic base and its direct adatoms. In this configuration the top and bottom part can be freely rotated relative to each other around the vertical axis. Considering only the attractive force between the atoms first, their interaction leads to a configuration where the top and bottom half

are vertically aligned on top of each other, such that every adatom from the bottom group has a direct vertical neighbour in the top group (Figure 3.6a). This type of molecular configuration can be found in wurtzite structured crystals. If one on the other hand only regards the repulsive interaction between the bonding electron orbitals then the top half of the molecule is rotated by 60° and every adatom from the top group is positioned vertically above the center of the gap between two of the bottom adatoms (Figure 3.6b) – a configuration as found in the zincblende structure. Which of the interactions dominates and therefore determines the crystal structure of a given material depends on the ionicity of the bonds and hence on the electronegativity difference between the involved elements. With increasing ionicity the preferred structure changes from zincblende to wurtzite and for even higher ionicities towards rock salt structure.[118, 119]

The strength of the preference towards the one or the other structure can be expressed by a difference in the *formation enthalpy* $\Delta E_{\mathrm{wz-zb}} = E_{\mathrm{wz}} - E_{\mathrm{zb}}$. If this value, which is typically given as (meV/atom pair) or (meV/atom), is positive then the zincblende structure is favoured and vice versa. Simulations show that $\Delta E^{\mathrm{bulk}}_{\mathrm{wz-zb}}$ is positive in the order of 10 meV/atom for non-Nitride III–V semiconductors but negative and of slightly larger absolute value for the Nitrides, which explains the predominance of the wurtzite strucutre in the Nitrides.[116, 120] For bulk GaAs the published values are in the 8 meV/atom to 12 meV/atom range.[113, 116, 120–123] It is notable that the thermal energy $k_{\mathrm{B}}T$ of the crystal at typical growth conditions is somewhere above 60 meV and therefore much larger than the transition energy between both structures.[123] Hence a coexistence between both crystal phases should be possible from an energetic point of view but is not observed in bulk materials or layer growth, as already stated before.

Size effects

For nanowires the situation is different due to their limited diameter. In the bulk case one can simply neglect the influence on the total formation enthalpy that atoms at the crystal surface have compared to those in the volume as the number of atoms within the crystal exceeds by far the number of surface atoms. A nanowire can easily be approximated as a long thin cylinder, which yields a surface to volume ratio that is proportional to its inverse diameter $\frac{1}{d}$ which also applies to the number of atoms in the crystal. For typical nanowire diameters around 100 nm and below this figure is well above $\frac{1}{100}$, i.e. the fraction of surface atoms compared to the total number of atoms can easily make up several percent. In this case a non-negligible amount of energy is needed to rearrange dangling bonds on the surface atoms which significantly changes the overall formation enthalpy per atom of the crystal – and from a surface energy point of view the wurtzite structure obviously is in favour here.[124, 125] Theoretical calculations show that $\Delta E^{\mathrm{Nanowire}}_{\mathrm{wz-zb}}$ decreases with

decreasing nanowire diameter and can reach negative values also for the non-Nitride materials below diameters around 20 nm. This means that the probability for wurtzite growth is strongly enhanced for the non-Nitride materials and that for small nanowire diameters even wurtzite is the favoured crystal structure.[120, 124, 125] The latter has been shown also experimentally by Shtrikman *et al.* [123] which were able to grow GaAs nanowires with diameters of less than 10 nm which are nearly pure wurtzite.

On the other hand typical nanowire diameters are about one order of magnitude larger than those reported by Shtrikman *et al.* [123] where the diameter-related preference for wurtzite vanishes. Therefore it is quite common for nanowires to have both polytypes contained in the very same nanowire with more or less frequent and mostly random switching between both structures and a tendency towards one polytype. Nonetheless there are numerous reports on the growth of wurtzite dominated nanowires also at higher, more 'typical' nanowire diameters.[56, 57, 126–130] Also there were many works exploring the problem from the theoretical side and trying to find criteria to explain how the local thermodynamic conditions at the growth front influence the genesis of either of the two crystal structures.[40–55] But most publications only describe which growth parameters and methods are able to produce a tendency towards one ot the other crystal structure and only very little publications claimed to be able to – at least partially – control and tune the growth of a certain crystal structure.[126, 130, 131]

Beside the pure wurtzite and zincblende structure there have also been some rare observations of the 4H polytype.[86, 132, 133] This polytype with a stacking order $ABCB$ can be considered as intermediate structure between zincblende and wurtzite which contains both, cubic and hexagonal contributions in a repetitive sequence that repeats after every fourth stacking layer.[46, 86, 98]

3.1.4 Stacking faults

Much more frequent than nanowires of pure crystal structure is the occurrence of *stacking faults* where the structure is disturbed by the random inclusion of a single or a few stacking planes that deviate from the normal stacking sequence. Such inclusions are much easier to achieve than a whole unfavoured crystal structure as a small thermodynamic fluctuation in the growth conditions or even the thermal energy alone might suffice for its genesis. Stacking faults are known from bulk crystals as well, but play a much bigger role in nanowire growth as a result of the shift of the formation enthalpy towards more unstable conditions.

Stacking faults can in both crystal structures be divided into different categories depending on whether they can be generated from an undisturbed crystal by removal or shift of a stacking plane or if an additional plane has to be introduced into the crystal (cf. Figure 3.7). In this categorization scheme an *intrinsic stacking fault*

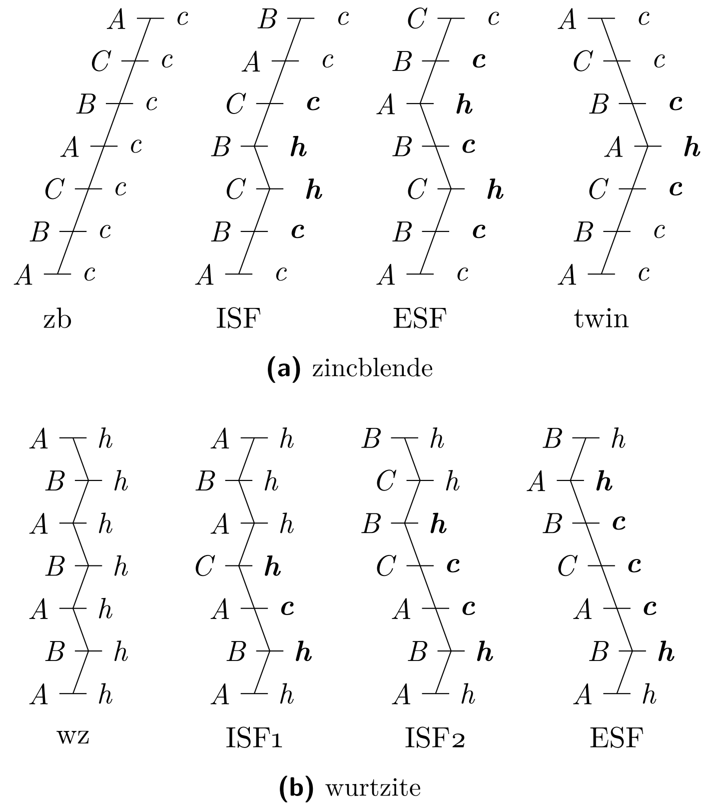

Figure 3.7: Stacking sequences of the different stacking fault types in zincblende and wurtzite. The horizontal lines in each figure denote the vertical position of the layers, with their position in the stacking order left of them. The letters on the right side of each figure denote if a layer has cubic (c) or hexagonal (h) characteristics. The layers forming the stacking fault and the direct neighbours of the fault are indicated in bold face. (redrawn from [117])

(ISF) is generated in the zincblende structure by removing one monolayer while in wurtzite a stacking plane with all its successors is shifted from its original position to the not occupied C stacking position. Consequently there is only one type of intrinsic stacking fault in zincblende as the structure is identical except for a translation at every layer, but there are two such types in wurtzite where it matters if the A or the B layer is shifted to the C position. Of the *extrinsic stacking fault* (ESF) on the other hand – which forms by inclusion of an additional layer into the stacking order – there is only one type in both crystal structures. In addition to the already described types there exists another stacking fault type only in zincblende which is generated by reversing the stacking order from ABC to CBA. As this can also be seen as two identical crystals brought together after one of them was rotated by 180° this stacking fault is referred to as (rotational) *twin stacking fault* (twin).[88, 97, 117, 134, 135] The twin in zincblende and the ISF1 in wurtzite are the faults that each introduce the smallest possible segment of the respective other stacking as can be seen from the annotations in Figure 3.7 indicating cubic (c) and hexagonal (h) layers. Here a layer is hexagonal when its neighbouring layers are of equal type in the ABC notation, while a cubic layer has two different neighbours.[88, 117]

Glas [117] has estimated the formation energies for the different stacking fault types in common semiconductor materials. The calculations are based on the measurable energy of the intrinsic stacking fault (for GaAs compare [136, 137] and references therein) and calculated differences in formation enthalpies between polytypes. The values given by Glas are positive for stacking faults in the default crystal structure a material exhibits and negative for such in the other structure. For GaAs additional energy is needed to create a stacking fault in its zincblende phase while creating a stacking fault in the wurtzite phase frees energy, making it difficult to create a stacking fault free wurtzite crystal in GaAs. The values given in [117] are in units of (mJ/m^2) which can, according to Gottschalk *et al.* [138], be converted to (meV/atom) via a multiplication by $2.7a_{\mathrm{cub}}^2$ where a_{cub} is the cubic unit cell parameter in (nm).

According to Glas [117] the twin is the zincblende stacking fault with the lowest energy of 14.8 meV/atom – which is rather close to the energy difference between zincblende and wurtzite– and therefore the most probable stacking fault in GaAs with the two other types requiring roughly twice and thrice as much energy. This also coincides with the observations made with semiconductor nanowires in the zincblende structure, where nearly exclusively twin stacking faults occur, sometimes even in highly regular order.[139–142]

In wurtzite GaAs the ESF (81.0 meV/atom) should be the dominating type as it contains the highest amount of cubic layers and should free the most energy. However, the values presented in [117] are calculated based on bulk material properties and, as Glas himself points out, do not take into account any surface or size related effects. Based on the consideration presented in Section 3.1.3 of the present work one can

therefore assume that for conditions, where wurtzite gets the preferred structure for a normally zincblende crystal, also the energies have to be adjusted. This is easily done by switching the sign of the values given in [117] with the result that the ISF1 with an energy of 33.1 meV/atom is then the most probable one for the wurtzite phase. This also corresponds to the values for the wurtzite structured III–nitrides, where the ISF1 is the one with the lowest energy.[117, 135]

In consequence – especially of the shifted energies due to the high surface to volume ratio – most nanowires exhibit a high number of stacking faults that can reach densities around hundred stacking faults per micron. In such case it often no longer appears appropriate to distinguish between wurtzite and zincblende structure but to qualify this as a random stacking sequence instead, even if this apparently random behaviour seems to be organized to some extent.[143] But also with nanowire samples where the growth conditions were tuned to enforce a certain crystal structure it is a rare occasion to find a nanowire that is totally free of stacking faults. Instead a stacking fault density of some ten per micron is already considered a good value.[127, 130, 131]

3.2 Spontaneous Polarization

3.2.1 Structural parameters

The competing attractive and repulsive forces between different parts of the crystal as discussed in Section 3.1.3 (cf. also Figure 3.6) do not only result in a preference for either one of the two possible crystal phases but cause also a deformation of the atomic tetrahedron in the wurtzite crystal phase. Up to now the atomic tetrahedra have been considered perfectly regular, formed around a central atom by four bonds of equal length. This is true for real zincblende crystal structures, but not for hexagonal polytypes, where the real structure can deviate from this ideal tetrahedral form. As the deviations from an ideal tetrahedron are in the single-digit percent range or smaller for the crystal structures regarded here, this will in the following just be called a non-ideal tetrahedron.[144]

Under the requirement, that the resulting body should keep a three-fold symmetry around one of its height axes, it is a pyramid with an equilateral triangle as bottom plane and the pyramid's tip above the center of the bottom triangle. Together with the atomic tetrapod that represents the arrangement of atoms within this pyramid, there are three parameters to fully characterize the situation, as denoted in Figure 3.8. Those *structural parameters* are typically used in relation to the wurtzite unit cell, i.e a unit cell that has a height of two monolayers. The pyramid itself is characterized by its bottom plane with side length a_{hex} and the height h. h is related to c_{hex} via $\frac{1}{p}$ with p the stacking periodicity of the considered polytype, i.e. for wurtzite $h = \frac{1}{2}c_{\text{hex}}^{\text{wz}}$, for zincblende it is $h = \frac{1}{3}c_{\text{hex}}^{\text{zb}}$. For cubic crystal

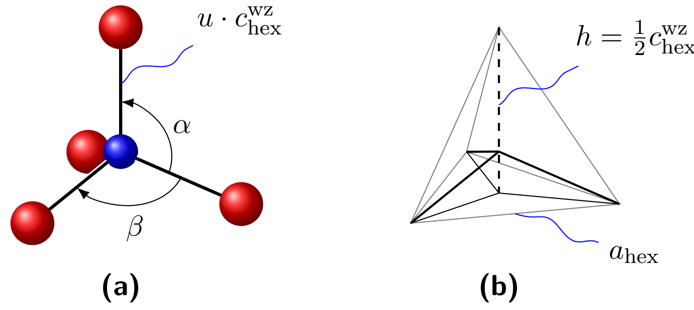

Figure 3.8: The atomic tetrapod and its structural parameters in terms of the wurtzite unit cell parameters $c_{\text{hex}}^{\text{wz}}$ and a_{hex}: (a) The atomic tetrapod consisting of a sp^3-hybridized atom of one species with four adatoms at its bonding orbitals is drawn together with the representation of the parameter u and the two bond angles α and β. In (b) only the bonds of the same molecule are drawn together with the surrounding tetrahedron and with the structural parameters annotated.

structures a_{hex} and c_{hex} can easily be calculated from a_{cub} via $a_{\text{hex}} = \sqrt{2} a_{\text{cub}}$ and $c_{\text{hex}} = \sqrt{3} a_{\text{cub}}$ for geometrical reasons. Typically the dimensionless ratio h/a_{hex} or more commonly $c_{\text{hex}}^{\text{wz}}/a_{\text{hex}}$ are used as they allow to compare the parameters of different materials. The latter is known as *cell-shape parameter*. The third, so-called *internal-cell parameter* u describes the fraction between the atomic base length and the height of the wurtzite unit cell.[98] Hence it is a measure for the position of the central atom within the pyramid. For a perfectly symmetric tetrahedron as it occurs in zincblende the structural parameters are

$$\frac{c_{\text{hex}}}{a_{\text{hex}}} = \frac{2h}{a_{\text{hex}}} = \frac{2c_{\text{hex}}^{\text{zb}}}{3a_{\text{hex}}} = \sqrt{\frac{8}{3}} = 1.633 \tag{3.1}$$

and

$$u = \frac{3}{8} = 0.375. \tag{3.2}$$

Additionally, the bond angle α (see Figure 3.8) between the vertical and any of the three other bonds is the same as the angle β between the bonds forming the bottom plane of the ideal tetrahedron and amounts to $\alpha = \beta = 109.47°$.[144]

Deviations of the structural parameters are caused by the forces that also lead to the formation of either wurtzite or zincblende as explained in Section 3.1.3. In the III-Nitrides with their 'natural' wurtzite structure the attractive force between unlike core atoms of neighbouring layers (cf. Figure 3.6a) 'flattens' the angles between the basal plane of the atomic tetrapod and its central atom. Under the assumption, that

the bonding lengths do not change that means that a_{hex} is increased and h reduced, resulting in a cell-shape parameter $c_{\text{hex}}/a_{\text{hex}} < \sqrt{8/3}$. It was already discovered in the 1970s by Lawaetz [145] that this is common to all materials with a stable wurtzite phase and confirmed with different methods by Yeh *et al.* [116] and Ito [119]. For the non-Nitrides the situation is reversed as the atoms in the basal plane are pushed to steeper angles, which reduces a_{hex} and increases h and therefore also causes $c_{\text{hex}}/a_{\text{hex}}$ to be larger than $\sqrt{8/3}$.[98, 116, 146]

Consequently the internal-cell parameter u changes opposite to the $c_{\text{hex}}/a_{\text{hex}}$ ratio – even if the length of the vertical bond is assumed to stay constant – as it describes the fraction of the vertical bond of the overall height c_{hex} of the unit cell. But according to calculations of Belabbes *et al.* [98] the change is about 0.5 % larger than expected for a constant bond length, which suggests that also bond lengths change by a small amount. This was experimentally verified for the III–nitrides (see [144]) and McMahon and Nelmes [113] did find for wurtzite GaAs that the three non-vertical bonds are elongated by 0.04 % to (0.2449 ± 0.0001) nm compared to the ideal 0.2448 nm of zincblende. However, the difference they determine is still within the error margin of their measurement.

The deviations of both parameters $c_{\text{hex}}^{\text{wz}}/a_{\text{hex}}$ and u from the values for an ideal tetrahedron are very small: For the Nitrides they are calculated to be in the range of 1 % and about an order of magnitude smaller in the non-Nitrides.[98, 116] The different lattice parameters and other relevant quantities are listed in Table 3.1 for GaAs and GaP.

For the zincblende phase of the non-Nitrides the lattice parameters are experimentally well explored and the widely accepted values of a_{cub} for GaAs and GaP are 0.565 32 nm and 0.545 05 nm, respectively.[116, 150] This results in lattice spacings h of 0.326 39 nm (GaAs) and 0.314 68 nm (GaP). For the wurtzite phases of the non-Nitrides the situation is less clear due to the fact that there was no such material widely available until some years ago. Table 3.1 contains a collection of theoretically and experimentally obtained figures for the different lattice parameters of GaAs and GaP. For GaAs the values calculated in theoretical works diverge significantly among different publications especially in consideration of the magnitude of the expected deviations.[98, 116, 122, 124, 146] Also there are only few experimental values yet which are astonishingly consistent, though.[113, 115, 148, 149, 153] Only the value for c_{hex} given by Gurwitz *et al.* [115] is significantly off compared to the other ones. However, the way their sample was fabricated does not necessarily exclude the possibility of a strained growth and hence a modified lattice constant. Above that, they argue that they could not determine for sure that the crystal structure is pure wurtzite and not for example a 4H polytype. Among GaP there are less values available which makes it more complicated to estimate their consistency, but there is a certain trend for the experimental values to be slightly larger compared to the theoretical ones.

Table 3.1: Collection of structural parameters of GaAs and GaP as presented in different publications. The superscripts at the citations denote if the values were determined theoretically (t) or experimentally (e). h_{cub} and h_{hex} are not explicitly given in the referenced publications but can be calculated as $h_{\text{cub}} = \sqrt{3}/3 \cdot a_{\text{cub}}$ and $h_{\text{hex}} = c_{\text{hex}}/2$.

	a_{cub} nm	h_{cub} nm	a_{hex} nm	c_{hex} nm	h_{hex} nm	$\frac{c_{\text{hex}}}{a_{\text{hex}}}$	u
				GaAs			
[116][t]	0.5654	0.3264	0.3912	0.6441	0.3221	1.647	0.374
[146][t]	0.56110	0.32395	0.39556	0.65095	0.32548	1.6456	—
[124][t]	0.5721	0.3303	0.4029	0.6652	0.3326	1.651	—
[98][t]	—	—	—	—	—	1.6456	0.3746
[147][t]	—	—	0.3928	0.6482	0.3241	1.650	0.3712
[122][t]	—	—	0.3540	0.6308	0.3154	1.782	—
[148][e]	—	—	0.3987	0.6575	0.3288	1.649	—
[113][e]	—	—	0.3989	0.6564	0.3282	1.6455	0.373
[149][e]	—	—	0.3988	0.6562	0.3281	1.645	—
[115][e]	—	—	—	0.668	0.334	—	—
[116][e]	0.565325	0.326391	—	—	—	—	—
[150][e]	0.56532	0.32639	—	—	—	—	—
				GaP			
[116][t]	0.5328	0.3076	0.3759	0.6174	0.3087	1.643	0.374
[98][t]	—	—	—	—	—	1.6443	0.3746
[147][t]	—	—	0.3789	0.6253	0.3127	1.650	0.371
[116][e]	0.54506	0.31469	—	—	—	—	—
[150][e]	0.54505	0.31468	—	—	—	—	—
[151][e]	—	—	0.3842	0.6335	0.3168	1.649	—
[152][e]	—	—	0.38419	0.63353	0.31677	1.6490	0.37385

The bonding angles α and β can be calculated through geometrical considerations from the structural parameters $c_{\text{hex}}/a_{\text{hex}}$ and u via the equations presented in Ambacher and Cimalla [144]:

$$\alpha = \frac{\pi}{2} + \arccos\left[\left(\sqrt{1 + 3\left(\frac{c_{\text{hex}}}{a_{\text{hex}}}\right)^2\left(\frac{1}{2} - u\right)^2}\right)^{-1}\right] \tag{3.3}$$

$$\beta = 2\arcsin\left[\left(\sqrt{\frac{4}{3} + 4\left(\frac{c_{\text{hex}}}{a_{\text{hex}}}\right)^2\left(\frac{1}{2} - u\right)^2}\right)^{-1}\right] \tag{3.4}$$

Based on the structural parameters calculated by Belabbes *et al.* [98] they result in $\alpha = 109.7°$ and $\beta = 109.3°$ for both GaAs and GaP which means that the 'legs' of the tetrapod are pushed downwards by approximately 0.2° with respect to the zincblende configuration.

3.2.2 Microscopic charge redistribution

Since the elements involved in a compound semiconductor differ in their electronegativity there is a polarization in the bond between two atoms of different species. The polarization is caused by the fact that the bonding orbital is not symmetric between the atoms but located closer to the atom with the stronger electronegativity. One can assign the different atomic species a positive or negative net charge q depending on how much the orbital is shifted towards or away from them and call them *anion* and *cation* accordingly. Among the III–V semiconductors the role of the cation is taken over by the group–V element and the group–III is the anion.[154]

Put together to a tetrapod one can easily see that for an ideal tetrahedral configuration as depicted in Figure 3.9a the charge barycentre of the adatom species lies exactly at the position of the central atom. In the 2D projection this is represented by the fact that there are three cations of charge $\frac{1}{4}q^-$ which are located at a height of $\frac{1}{4}h$ below the central atom and one such atom at $\frac{3}{4}h$ above. The central anion itself has net charge q^+ in this example as it has four polar bonds, hence the whole molecule does not have a polarization. Since in a crystal also every cation is surrounded by four anions in the same manner, the same is true for every cation with the polarities reversed. As a result it can be stated that in a crystal structure that is built from atoms in ideal tetrahedral configuration there exists no net polarization within the crystal.[144, 154–156]

With a non-ideal configuration this is no longer true, as can be seen in Figure 3.9b. Here the barycentre of the net charges of the adatoms (indicated by the red dot) does no longer coincide with the central atom but is shifted, with the direction depending on the cell-shape parameter. With the III-Nitrides with $c_{\text{hex}}/a_{\text{hex}} < \sqrt{8/3}$

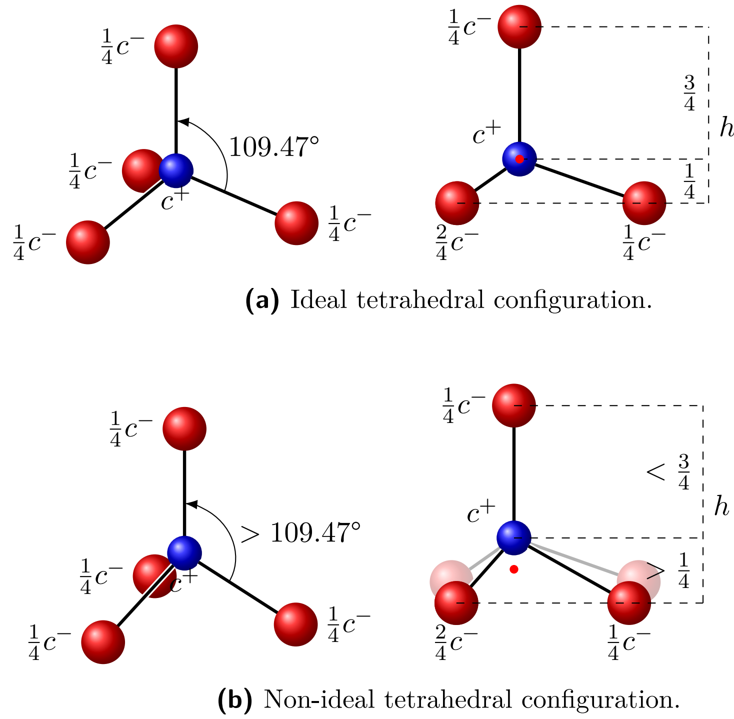

(a) Ideal tetrahedral configuration.

(b) Non-ideal tetrahedral configuration.

Figure 3.9: Charge localization in an atomic tetrapod consisting of a central anion with four cationic adatoms in ideal (a) and non-ideal (b) tetrahedral configuration. The drawings show a 3D representation on the left and on the right a 2D projection, where the two bottom left cations ly exactly behind each other. In the 2D images the red dot denotes the position of the charge barycentre of the four cationic atoms. For the drawings of the non-ideal configuration the example case of $c_{\text{hex}}/a_{\text{hex}} > \sqrt{8/3}$ (non-Nitride materials) is drawn with highly exaggerated angular deviation. The semi-transparent features in the 2D projection represent the atom positions of the ideal case for comparison.

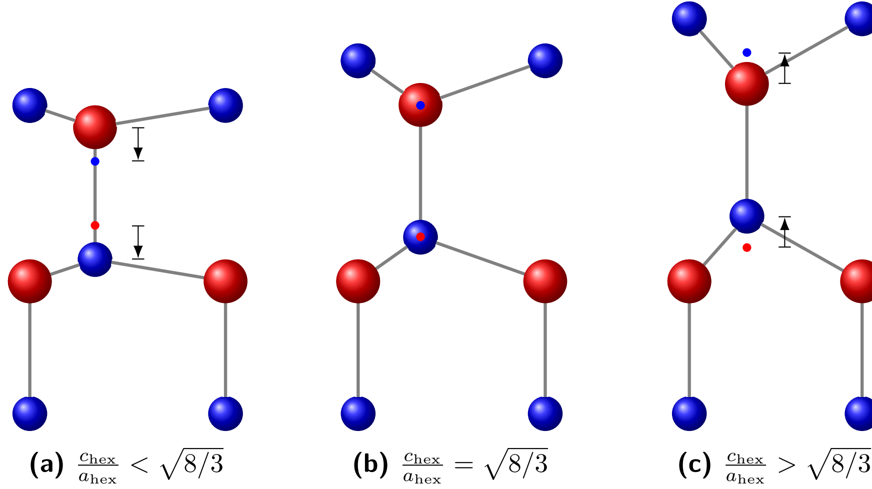

(a) $\frac{c_{\text{hex}}}{a_{\text{hex}}} < \sqrt{8/3}$ **(b)** $\frac{c_{\text{hex}}}{a_{\text{hex}}} = \sqrt{8/3}$ **(c)** $\frac{c_{\text{hex}}}{a_{\text{hex}}} > \sqrt{8/3}$

Figure 3.10: Polarization of the non-trivial wurtzite unit cell of (a) Nitride–like, (b) ideal, and (c) non-Nitride–like crystal configuration. The polarization features are only drawn at the single vertical bond of each structure but are present analogously at the other atoms as well in a full crystal lattice. Red and blue atoms represent cations and anions, respectively. The red and blue dots denote the barycentres of negative and positive charges of the surrounding atoms. Arrows mark the dipole moment between charge barycentre and its nearest atom.

the charge barycentre of the adatoms is located at the vertical bond while in the non-Nitrides it sits within the pyramid formed by the three bottom atoms and the central one as depicted in Figure 3.9b.[154, 156]

If one now builds non-trivial wurtzite unit cells from those tetrapods for the ideal and both non-ideal configurations as depicted in Figure 3.10 one can see in the non-ideal configurations that at every atom there is a dipole between the atom itself and the barycentre of the surrounding atoms. Although this is a highly oversimplified image it demonstrates that there are no dipoles in the case of an ideal tetrahedral configuration (Figure 3.10b) due to symmetry reasons and that the direction of the dipoles change when going from a Nitride-like configuration ($c_{\text{hex}}/a_{\text{hex}} < \sqrt{8/3}$, Figure 3.10a) to a configuration as it occurs in the wurtzite phases of the non-Nitride III–V semiconductors ($c_{\text{hex}}/a_{\text{hex}} > \sqrt{8/3}$, Figure 3.10c). Regarding the full unit cell this results in a net *polarization* of the unit cell that is caused by the non-ideality of the atomic configuration.[144, 154–156]

As already touched on shortly, the explanation for the origin of the polarization given in the previous paragraphs is handwaving, highly simplified and especially only based on electrostatic considerations. The reason is that a quantum-mechanical treatment – as it is needed on this microscopic scale – was due to its complexity

only introduced about twenty years ago by King-Smith and Vanderbilt [157] and Resta [158] – long after most other fundamental crystal properties at atomic level. Deeper explanations of the issues involved and the methods used in calculations are given in [159] and [160]. Nowadays the charge distribution in such systems is typically calculated with *density functional theory* (DFT) methods. However, even in such calculations the exact charge distribution and therefore the localization of the polarization depends on the chosen boundary conditions.[159, 160] Therefore it is not easily possible to draw a definitive charge distribution within the crystal, especially if one considers rather uncommon configurations such as more or less randomly mixed wurtzite and zincblende structures. However, it can be stated that a wurtzite unit cell contains one positive and one negative charge barycentre that are oriented along the [0001] direction [155] and that the polarization in the non-Nitrides is basically oriented opposite to the Nitride semiconductors. Above that it can be stated that '[t]he electric dipoles in each unit cell [. . .] are "frozen" once the crystal is grown, and can contribute to the formation of bound as well as mobile charges.' [155]

The polarization can further be distinguished by the origin of the non-ideality in the atomic configuration: If the deformation is the result of strain applied to the crystal lattice it is called *piezoelectric polarization*. This is typically the case by compressing or extending a crystal along a polar axis to make use of the piezoelectric effect. Another way is the lattice-mismatched growth of one material onto a different one, where the former material is strained as it adapts to the crystal lattice of the underlying one. As such it can occur also in materials and crystal structures that are unpolarized in their unstrained state. The *spontaneous polarization* P_{sp} on the other hand does not result from an external force acting on the crystal lattice but is an intrinsic property of the crystal lattice itself – it exists in a totally relaxed crystal just due to the non-ideal atomic configuration.

3.2.3 Macroscopic implication – the quantum confined Stark effect

To see how the polarization acts on a macroscopic level the polarized wurtzite unit cell is extended to a crystal lattice. By that there form planes perpendicular to the [0001] axis that contain either only positive or only negative charge centres. From a mesoscopic point of view these can be regarded just as charged planes or 'charge sheets' of alternating polarities $\sigma+$ and $\sigma-$ stacked along the crystallographic c axis with the same periodicity as the crystal lattice itself, as depicted in Figure 3.11. Drawing a diagram with the polarization strength on one and the location of the charge sheet on the other axis (Figure 3.11b) the picture resembles a comb with two back-to-back rows of teeth, each of them having a period of c_{hex} and shifted towards the other by a half period.

For a perfect, defect-free wurtzite crystal – the same would of course apply for any other polar configuration, such as the 4H and 6H structures[98, 146] – the

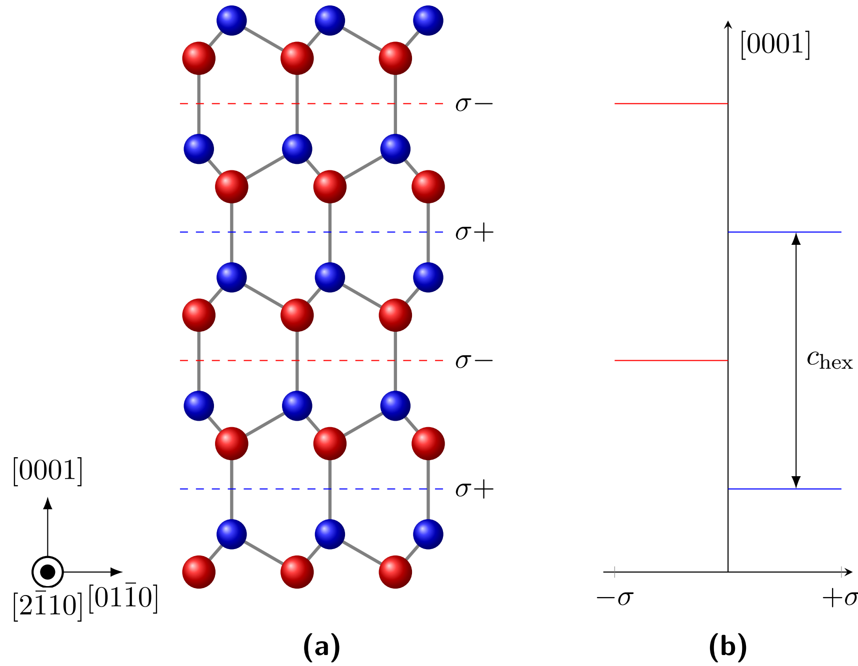

Figure 3.11: Schematic wurtzite crystal lattice of a non-Nitride semiconductor with a possible localization of the positive ($\sigma+$) and negative ($\sigma-$) sheet charges within the crystal. The diagram (b) is reduced to the localization and sign of the sheet charges. (redrawn in analogy to [155])

alternately charged layers inside the crystal cancel each other out when seen from a macroscopic level. Therefore the crystal can be considered free of macroscopic electric fields. Only on the {0001} surfaces there remains a charge sheet at each end of the crystal that is not enclosed between sheets of opposite polarity and therefore contains a macroscopically relevant charge. These surface charge sheets would act like the plates of a capacitor with the whole crystal as a dielectric in between. In a perfect vacuum which is free of any residual gas this would theoretically even happen with the unpolarized zincblende crystal, as the symmetric arrangement of the charge barycentres is broken at the surfaces as well. In reality, however, these surface charges are saturated by adsorbate contaminations that form from molecules present in the environment on the crystal surfaces, hence a real crystal without any external influences such as pressure or strain applied does not show charge effects at its outside.[155] As a side-note it should be mentioned here that in most publications such images are drawn based on an even number of monolayers which corresponds to a crystal that consists only of full wurtzite unit cells and therefore it can be assumed that the crystal is terminated by charge sheets of

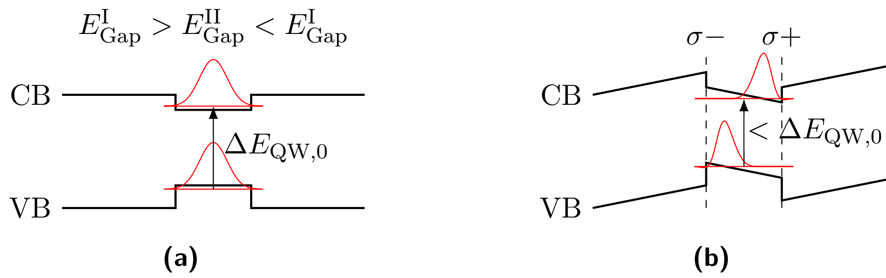

Figure 3.12: Schematic drawing of a typical quantum well of a layer of one material enclosed between two layers of wider band gap material. The band structures of the materials lead to heterojunctions with a type-I band alignment. The red curves schematically represent the electron and hole wave functions of the ground state within the quantum well. (a) shows the situation without any electric fields while in (b) there is an electric field present caused by sheet charges $\sigma-$ and $\sigma+$. This results in a displacement of the electron and hole wave functions and a reduction of the band gap known as the quantum confined Stark effect.

opposite polarity at opposing surfaces, as it is also drawn in Figure 3.11a. However, there is no obvious reason why the crystal should not terminate after an odd number of monolayers, which would leave the crystal with two charge surfaces of equal polarity.

In a realistic world, however, if there are 'imperfections' within the crystal, these can give rise to charge sheets within the crystal which are not or only partially saturated and cause an electric field on a macroscopic level. Probably the most common case of such 'imperfection' in semiconductors are hetero-interfaces where the material composition changes. They are rather well explored and especially in the III–nitrides it is known that there are differences in spontaneous polarization from the crystal structure and piezoelectric polarization from the lattice mismatch involved at such interfaces.[144, 154–156, 159, 161] But also the interface between a polarized and an unpolarized crystal structure – as it occurs at a wurtzite-zincblende interface – or even a single stacking fault is enough that there remain unsaturated or only partially saturated charge sheets.[162–165] Also a twin defect in zincblende, which forms the smallest possible wurtzite type segment as mentioned in Section 3.1.4 will have an influence here.

Such electric fields inside the material cause a deformation of the band structure and therefore of the properties related to the band structure. A very well-known effect in this context is the so-called *quantum confined Stark effect* (QCSE) where the electric field causes a tilting of the bands inside and outside of a quantum well.[166] This results in a change in luminescence behaviour in two ways: As the band edges come closer the band gap in the quantum well gets smaller, hence the emission

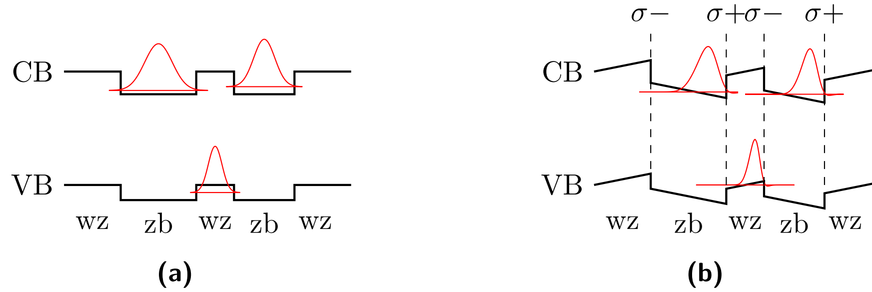

Figure 3.13: Schematic drawing of a series of layers with type-II band alignment in (a) field-free conditions and (b) with quantum confined Stark effect (QCSE) caused by internal sheet charges. The type-II band alignment which is in this case caused by alternating wurtzite and zincblende segments causes a spatial separation of electron and hole wave functions in different segments. The QCSE further complicates the situation by shifting the energies and localizations of the wave functions.

wavelength decreases, and the wave functions for electrons and holes in the quantum well are shifted to opposite sides of the quantum well which results in a reduction of luminescence efficiency due to a smaller transition dipole moment.[144] Figure 3.12 shows the commonly known situation for the QCSE in a heterostructure quantum well in different materials which form a type-I band alignment, i.e. where between the narrow and the wide band gap material the valence and conduction band offsets are of different sign and electrons and holes are confined at the same position. This arrangement is well-known and explored in the III-Nitride semiconductor heterostructures as described for example in Wood and Jena [167] and Jain *et al.* [168].

In a *staggered* or *type-II* band alignment the valence and conduction band offsets between two materials have the same sign, which causes a spatial separation of electrons and holes (cf. Figure 3.13a).[163, 169, 170] Such a band alignment can not only be formed by different materials but ab-initio calculations show that all non-Nitride III–V semiconductors except GaP should have this band alignment between their zincblende and wurtzite phase.[171] For GaAs the theoretical predictions are confirmed by several experimental works [129, 169, 170, 172] and also for GaP there are hints that under certain conditions a staggered band alignment may occur.[151] As frequent crystal structure switching and stacking faults are common in semiconductor nanowires, many of them can be regarded as a sequence of wurtzite and zincblende segments of random thickness where the segments act as quantum wells of various width and therefore with a wide range of different ground state energies. This already can lead to rather complicated luminescence spectra compared to bulk or quantum well samples [172, 173] and can be seen as one reason why the

emission energies that various publications claim to have measured for the wurtzite crystal phase of GaAs deviate significantly.[68, 127, 129, 163, 169, 170, 174–179]

To this already complicated situation another parameter was added by Jahn *et al.* [169] who found that their experimental values can be better explained by theory if they include a QCSE contribution caused by a spontaneous polarization of the wurtzite crystal phase.[163, 169]

3.2.4 Expected polarization strengths

Since the wurtzite phases of non-Nitride III–V semiconductors are only widely available for about one decade and the idea, that the wurtzite phase of the other III–V semiconductors should also exhibit a spontaneous polarization, is even younger, there is only a very limited number of figures available about the polarization strengths that can be expected in those materials.

For GaAs the values published so far are all in quite good agreement: The first to give a value for the magnitude of the spontaneous polarization P_{sp} were Jahn *et al.* [169], who estimated it to be one order of magnitude smaller than the one of GaN. This approach appears valid as the quantities $c_{\mathrm{hex}}/a_{\mathrm{hex}}$ and u to which P_{sp} is related, differ also one order of magnitude between GaN and GaAs. Their value of $0.002\,\frac{\mathrm{C}}{\mathrm{m}^2}$ is in very good agreement with later DFT calculations by Belabbes *et al.* [98] which yield a P_{sp} of $0.002\,\frac{\mathrm{C}}{\mathrm{m}^2}$ or $0.003\,\frac{\mathrm{C}}{\mathrm{m}^2}$, depending on the exact method, and by Al-Zahrani *et al.* [147] who give a value of $0.002\,\frac{\mathrm{C}}{\mathrm{m}^2}$.

In GaP the values are more ambiguous. Belabbes *et al.* [98] and Kriegner *et al.* [152] independently of each other published numbers nearly at the same time, the former with $0.003\,\frac{\mathrm{C}}{\mathrm{m}^2}$ calculated by DFT and the latter with $0.009\,\frac{\mathrm{C}}{\mathrm{m}^2}$ determined from *X-ray diffraction* (XRD) measurements. More recent DFT calculations by Al-Zahrani *et al.* [147] come to the same value as Belabbes *et al.* [98].

3.3 Summary

The crystal structure polymorphism that occurs in III–V-semiconductor nanowires and especially the wurtzite crystal structure that is not available in the bulk form of the non-Nitride III–V-semiconductors gives experimental access to material properties that have up to now been only described theoretically. One of them is the spontaneous polarization which results from the structural properties of the crystal lattice in the wurtzite phase and which was up to now only experimentally available with the III-Nitride semiconductors that grow in wurtzite by default. The experimental detection of the spontaneous polarization in the two non-Nitride III–V materials GaAs and GaP will be the subject of the experimental Chapter 5.

4 Transmission Electron Microscopy

Transmission electron microscopy (TEM) was initially developed in the 1930s by Knoll and Ruska [180] to overcome the limited spatial resolution of classical visible-light microscopes of about 200 nm. High energetic electrons that are accelerated by a voltage of some 100 kV have a de Broglie wavelength in the order of picometres which would yield diffraction limited spatial resolutions in the order of single-digit picometres. The realistically achievable resolution is about two orders of magnitude lower in the 0.1 nm range (the reason for this discrepancy is given in Section 4.1.2) but still three orders of magnitude better than what is possible with conventional light microscopy.[181–183]

Since then, many techniques and applications have been developed which made electron microscopy[1] far more than just the 'enhanced' light microscopy it was at first thought to be. In the physical and materials sciences it has proven to be a versatile tool especially under the aspect that today's semiconductor technologies with their trend towards miniaturization are already dealing with structure sizes in the order of few ten atom diameters. In this context today's state of the art electron microscopy is able to provide imaging and analysis methods with down to atom precision.

As there is a lot of literature on electron microscopy this chapter is restricted to a basic description of the technical details of transmission electron microscopy and only the important aspects of the techniques used in this work. For a comprehensive, yet very detailed, overview over nearly all aspects of electron microscopy the reader is referred to the textbook of Williams and Carter [181]. In addition the books of Thomas and Gemming [182], Reimer and Kohl [183], Spence [184] and Fultz and Howe [185] deal with certain fields of electron microscopy that were also employed in this work and discuss in great detail the various theoretical and technical aspects of their respective subjects. The descriptions given here also focus on general working principles while the actual technical realization in the instrument used for this work – a *Tecnai F30* by the manufacturer *FEI* – may contain additional components that enhance or optimize certain aspects but do not change the overall functionality. Such details are omitted or only shortly mentioned for completeness unless they are of importance within the framework of this thesis.

[1]Although also the non-transmissive *scanning electron microscopy* (SEM) is subsumed under the term 'electron microscopy' this term is used synonymously to the '*transmission* electron microscopy' techniques in the further reading.

4.1 General Setup and Components

A common transmission electron microscope is to a great extent built in analogy to a light microscope which is operated in transmission, i.e. it consists of an electron or light source, respectively, which illuminates the specimen through an optical system, another optical system that generates a magnified image of the specimen, and a detector to record this magnified image. Those components are described in this section.

However, as electrons interact much stronger with matter than photons do, the optical path of an electron microscope – the so-called *column* – has to be kept under high to ultra-high vacuum to allow the electrons to travel freely and without unwanted scattering within the optic system. Of course glass lenses are also not suitable since they would not work with electrons which will be addressed in Section 4.1.2.[181, 182]

It should be noted here that contrary to typical, conventional light microscopes, where the specimen is illuminated from the bottom and the detection system is located at the upper end, the optical path of most electron microscopes is reversed, i.e. the electron source is the top-most and the detection system the bottom end of the optical system.

4.1.1 Electron source and accelerator – the gun system

The first essential part of an electron microscope is the so-called *gun* system. It consists of an electron source that emits electrons which then are accelerated towards an accelerator anode to give them the desired energy of several hundred keV. The three common types of electron sources – the tungsten hairpin filament, the LaB_6 cathode, and the *field-emission gun* (FEG) – as well as their specific characteristics are described in references [181–185].

In the *Tecnai F30* used in this work the electron source is a field-emission gun which was first developed by Crewe *et al.* [186] and consists of a tungsten crystal needle with a tip radius of less than one nanometre. The crystal is set to negative acceleration voltage which is $-300\,\text{kV}$ in the course of this work. A ring-shaped anode – the *extractor* – in front of the crystal tip and at an electrostatic potential of about $+3\,\text{kV}$ to $+4\,\text{kV}$ with respect to the crystal extracts electrons from the tip via Schottky emission. As the electrons are accelerated towards the extractor anode, those which did exit the tip at too high an angle with respect to the optical axis impinge on the anode while those which left the tip at a flat angle pass the hole in the anode. Closely below the extractor there is a second ring-shaped anode at an electrostatic potential between the tip and the extractor potentials which compresses the divergent electron beam that passed through the extractor into a convergence point or cross over. As this anode acts as an electrostatic lens it is

called *gun lens* and the cross over it produces is known as the virtual source. From an electron optics point of view the cross over is the actual source to which the further optical system is related. After the gun lens the electrons are accelerated to their desired energy towards a third ring anode – the *accelerator* – which is at zero potential and where they finally enter the *column* which contains the optical system itself.[182, 186, 187]

4.1.2 Optical system

To direct the electrons from the gun towards the specimen and from the specimen to a detection unit an optical system is needed. However, electron optics cannot be built from glass lenses as was already mentioned before. Therefore an electron microscope requires a different type of lens which is formed by a rotation-symmetric inhomogeneous magnetic field that acts as a collective lens via the Lorentz force, as first described by Busch [188, 189]. Technically this is realized by current-carrying coils within a pole piece of soft magnetic material. Since the focal length of such lenses can be tuned via the current flowing through the coil – or a lens can even be switched off altogether – the optical setup is much more flexible than that of a light microscope. It allows for a magnification range of around five orders of magnitude with the same set of lenses without changing their physical position as well as several modes of operation with different lens configurations within one instrument (see Section 4.2).[181–185]

Unfortunately, the optical quality of magnetic lenses is quite low – in terms of optical lenses it is often compared to the imaging quality of the bottom of a glass bottle [190] – with significant spheric and chromatic aberration, described and often also named by their respective coefficients C_s and C_c, as well as astigmatism. The former two aberration types limit the achievable spatial resolution and are hard to overcome since they are due to the mechanical manufacturing precision of the lens components, as Scherzer [191] already realized in 1939. The resolution limit of about hundred electron wavelengths λ_e he formulated basically holds until present day for the lenses. Instead correctors for C_s and C_c were developed by Haider *et al.* [192, 193] in 1998 and 2010, respectively, which do not improve the lens itself but subsequently correct its aberrations caused by the lens through additional quadrupole and octopole magnetic fields, yielding the already mentioned achievable resolution slightly below 0.1 nm (around $25\,\lambda_\mathrm{e}$).[193, 194] The microscope used in this work was built before the realization of such correctors, therefore its resolution is still subject to the $100\,\lambda_\mathrm{e}$ limit, which nonetheless gives a 0.2 nm spatial resolution at an electron energy of 300 keV.

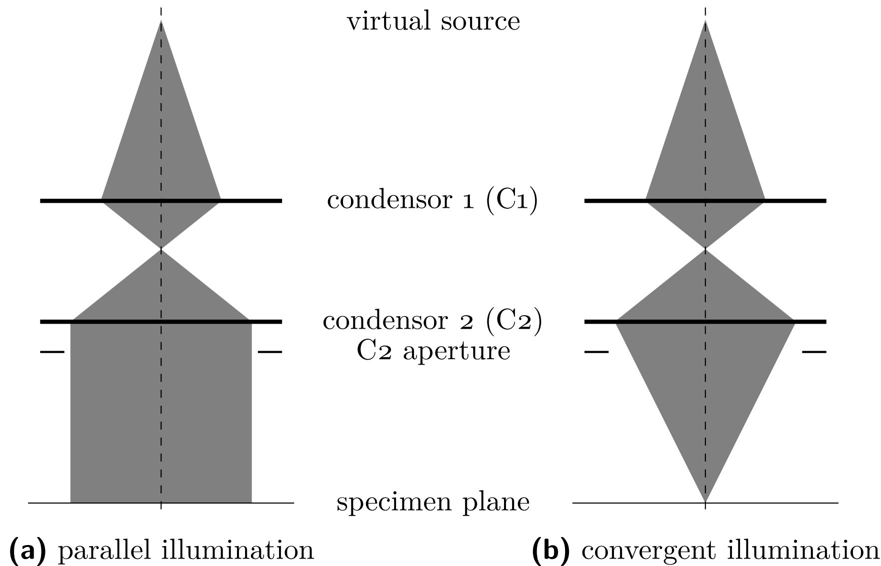

Figure 4.1: The double condensor system with the limit cases of 'parallel' and 'convergent illumination': The divergent beam coming from the virtual source is focused by the C1 lens into a cross over which is then projected by the C2 lens into the specimen plane either (a) as a parallel beam or (b) as a convergent cone that forms a small spot in the specimen plane. The C2 aperture below the C2 lens can block the outermost part of the beam after the C2 lens. (redrawn from [182])

Illumination system

Just like in a light microscope the *illumination* or *condensor* system projects the light source or in the electron microscope the first virtual image after the gun lens towards the specimen plane to illuminate the specimen there. By tuning the condensor system the illumination of the specimen can be varied continuously over a wide range of incidence cone angles according to the desired mode of operation. In Figure 4.1 the limit cases 'parallel' and 'convergent illumination' are depicted which are the two most frequently used illumination conditions.

Although basically a single lens would be sufficient to achieve the illumination conditions shown in Figure 4.1, the illumination system of most microscopes consists of a double condensor arrangement. The technical reason is that the aberrations of electron lenses scale with their focal length. Hence using two combined lenses of short focal length yields a better imaging quality than the use of only one lens which would need a significantly longer focal length. In addition the *condensor 1* (in short *C1*) lens creates a beam cross over in between both lenses which can be used

as an additional parameter named *spot size* to optimize the illumination conditions for certain applications. In real microscopes and also in the *Tecnai F30* further lenses are placed within the beam path between the *condensor 2* or *C2* lens and the specimen which help in reaching certain illumination conditions but do not change the overall beam path.[181, 182]

Projection system

The *projection* or *imaging* system does, as the name suggests, provide a magnified image of the illuminated specimen. It basically consists of three lenses, called the *objective*, *intermediate*, and *projective* lens as drawn in Figure 4.2 which in reality are again supplemented by additional lenses that have no influence on the general functionality. Above that magnetic lenses, due to their working principle, introduce a rotation around the optical axis by an arbitrary amount between an object and its image. The drawing is simplified insofar, as this rotation has been omitted.[181, 182]

In the following the setup of the projection system in *imaging* or *TEM* mode (for further information see Section 4.2.1) is described which is the functional analogy to the classical light microscope and is drawn in Figure 4.2a. Here the electrons coming from the specimen are projected by the objective lens into a *first intermediate image* which is transferred via the intermediate lens into the *second intermediate image* that is finally magnified and imaged to the detector plane by the projection lens. From a functional point of view changing the strength of the objective lens is providing the focusing of the specimen while tuning the projection lens does the main magnification of the final image. The function of the intermediate lens in the imaging mode is basically restricted to delivering a pre-magnified intermediate image of the specimen to the correct distance in front of the projection lens such that the latter will magnify it to the desired magnification. The more important function of the intermediate lens will come into play when the projection system is switched to diffraction mode as described in Section 4.2.2.

4.1.3 Detection

After the electrons have passed the specimen and the optical system they have to be recorded somehow to generate a viewable image. How this is done and which detection mechanisms are used for this task depends in the first place of the mode the microscope is operated in.

For the imaging or TEM mode and the diffraction mode which are described in more detail in Section 4.2.1 and Section 4.2.2 the projector system creates a spatially resolved image in the detector plane which requires also a detection system that is suitable to record such a spatial image. In the simplest case that is just a viewing screen consisting of a metal plate covered with a fluorescent coating like zinc

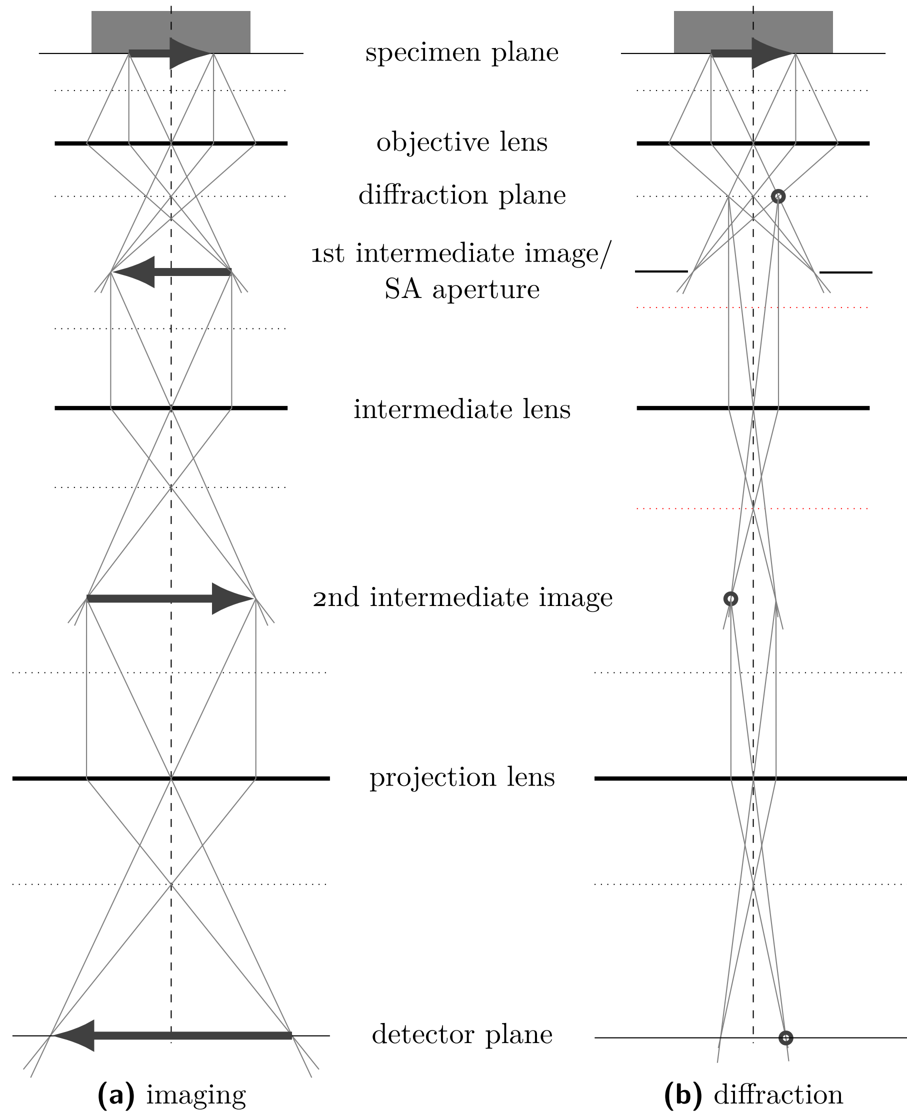

Figure 4.2: The projection system of the transmission electron microscope in (a) imaging and (b) diffraction mode. The dotted horizontal lines indicate the focal planes of the respective lenses. For the imaging mode (a) the thick arrows represent the imaged object and the planes where images of it are produced. In diffraction mode (b) the focal length of the intermediate lens is changed (compare the dotted red focal planes in (b)) such that it images the back focal plane of the objective lens, where a diffraction pattern of the imaged object is formed. Here one diffracted spot in the diffraction plane and its projections through the beam path are marked with circles.[181, 182]

selenide (ZnS) which converts the energy deposited by the electrons into visible light that can directly be seen by the human eye. If the image should not just be seen by eye but be recorded digitally, a similar setup is used, consisting of a scintillator crystal that is coupled to a peltier cooled *charge-coupled device* (CCD) camera via a bundle of optical fibres. The reasons for such a setup as well as a performance comparison with other recording techniques are reviewed in [195] and shall not be further discussed here. The CCD camera used in the *Tecnai F30* is capable of recording up to a few images per second at a resolution of 1024^2 pixels (px).

In contrary in scanning mode as explained in Section 4.2.3, where the spatial information of the image is acquired by scanning an electron probe across the specimen, one is interested in electrons that have left the specimen at a certain angular range with respect to the optical axis. Hence such a detector does not need to provide spatial resolution by itself but just has to count the electrons arriving at the desired solid angle region. This can be realized either by a photomultiplier tube with a scintillator crystal in front of it or by a semiconductor detector. The latter basically consists of a p-n junction in a semiconductor material (in most cases silicon) where the incident electrons create electron-hole pairs in the depletion region of the p-n junction which then can be recorded as a current proportional to the number of electrons. One of the benefits of the semiconductor detector design is that it can be fabricated in arbitrary shapes, which is taken advantage of in the differential phase contrast (DPC) system used in this work (cf. Section 4.3.1).[181, 183]

4.2 Modes of Operation

4.2.1 Transmission electron microscopy (TEM)

The classical *transmission electron microscopy* (TEM) imaging mode is the analogy to the conventional light microscope where a specimen is illuminated by a spatially extended beam and directly magnified by an optical system as explained above and drawn in Figure 4.2a. This mode is sometimes also named ‘conventional’ TEM (abbreviated CTEM) to distinguish it from scanning transmission electron microscopy (STEM) mode as described in Section 4.2.3.

While in the classical optical light microscopy the image contrast is formed by absorption of light within the specimen – unless special techniques as phase contrast or dark field microscopy are used – the absorption contrast does not play a significant role in electron microscopy. Instead three other contrast mechanisms are of importance in electron microscopy: mass thickness contrast, diffraction contrast and phase contrast.[181, 182] Diffraction contrast will not be further explained here since it does not play a role for the measurements presented in this work.

Mass thickness contrast

Mass thickness contrast is based on scattering of electrons within the specimen material. Its name stems from the fact that the scattering strength and therefore the resulting image contrast is related to the atomic masses of the elements contained within the specimen and the specimen thickness. The mass thickness contrast is the principal contrast mechanism for the imaging at low and medium ($\lessapprox 100\,000\times$) magnifications and of non-crystalline materials.

By filtering out scattered electrons that have left the specimen at angles higher than a certain maximum angle they cannot contribute to the image formation in the detector plane and hence lead to an intensity modulation in the detector plane. The selection of the maximum scattering angle can happen either just by the acceptance angle of the optical system itself, i.e. it is limited by the geometry of the beam path and the diameters of the lenses, or it can in addition be restricted by an aperture (not drawn in Figure 4.2) in the back focal or diffraction plane of the objective lens.[181, 182]

High-resolution imaging: phase contrast

Atomically resolved imaging of crystalline specimens – also known as *high-resolution TEM* (HR-TEM) – requires magnifications of several $100\,000\times$ where the aperture needed to achieve mass thickness contrast would insufficiently limit the spatial resolution. Instead the image formation is dominated by *phase contrast.*[181–184]

Unlike mass thickness contrast which can easily be described in the particle image, it is easier to employ the wave nature of high energy electrons for the understanding of phase contrast formation. In this picture the electrons that arrive at the specimen are plane waves – technically this is best achieved in the parallel illumination configuration (cf. Figure 4.1a) of the condensor system. As such a wave transverses the specimen it is retarded locally by the electrostatic potential of the atoms it passes and hence experiences a local phase shift. Therefore the wave front that exits the specimen is no longer flat but modulated by the accumulated phase shifts it has experienced on its way through the specimen. Unfortunately all technically realized detector types can only record intensities but no phase modulations, hence a method is needed to transform the modulated phase into a recordable intensity pattern. This can be done by bringing the phase modulated wave front into interference with another wave front of different phase to cause a pattern of constructive and destructive interference, i.e. an intensity modulated image. In general this can be solved by electron holography, where the electron wave is split into two beams of which only one passes the specimen. Both waves are then brought to interference after the specimen to generate an image of the phase distribution of the object wave that contains the phase information of the specimen.

For the investigation of crystalline specimens the same can be achieved without holography by using the crystal itself to split the wave into different beams. In this case the second wave of different phase is generated by the crystal lattice that acts on the electron wave as a diffraction grating. The diffracted beams caused by this process are shifted in phase with respect to the zero order beam and bringing them to interference with the correct phase shift would yield the desired imaging condition. To achieve this a combination of slightly defocusing from the specimen plane and making use of the spheric aberration C_s is employed to create an – from an imaging theory point of view – imperfect image of the specimen into the detector plane which, however, meets the interference condition and therefore produces an intensity modulated image of the crystal lattice.

To achieve atomically resolved imaging some conditions must be fulfilled: Firstly, as already said, the incoming wave should be as plane as possible, that means the phase front should at best be describable by a plane wave of wave vector $\vec{k}$, to illuminate a wide specimen area coherently. Secondly, the specimen has to be thin enough – typically $\lessapprox 50\,\mathrm{nm}$ [182, 183] – otherwise the phase contrast is affected by additional thickness-dependent distortions. The third and most crucial point is that the specimen has to be 'in zone axis' which means it has to be tilted with respect to the electron beam such that a crystal direction of high symmetry is oriented along the optical axis. Only if a zone axis is chosen where the crystal appears as built from independent, spatially separated atomic columns an atomically resolved image of the crystal is possible.

At this point it should however be noted that the exact image details as they are finally recorded in the detector plane strongly depend on the imaging conditions at the moment of the recording, especially the defocus from the specimen plane. Therefore such high-resolution TEM images alone should only be seen as qualitative images while analytical statements about certain properties, for example the exact displacement of single atomic columns, can only be made if they go along with computational methods which try to reconstruct the wave front as it exited the specimen.[182–184] Such methods have not been applied to the data shown in this work as this level of detail is not necessary for its interpretation.

4.2.2 Electron diffraction

It was already mentioned in the section before that a crystal lattice acts as a diffraction grating for electron waves, which means that most of the beam intensity that entered a crystalline specimen leaves it under a set of well-defined angles with respect to the optical axis due to Bragg diffraction. Also from geometrical optics it is known that in the back focal plane of a lens all waves that have entered the lens at the same angle meet in the same point as drawn in the *back focal* or *diffraction plane* of the objective lens in Figure 4.2b. Physically that means that the $\vec{k}$ vectors that

contributed to the phase front arriving at the objective lens are spatially mapped in the back focal plane, which is mathematically the Fourier transform of the phase front. Therefore this plane is also called *Fourier plane*. For a set of well-defined entrance angles or $\vec{k}$ vectors as those in the diffracted waves from a crystalline specimen this leads to a spot pattern in the diffraction plane of the lens.

By changing the focal length of the intermediate lens in a way that it projects the diffraction plane instead of the first intermediate image into the detector plane (cf. Figure 4.2b), the diffraction pattern can directly be imaged on the viewing screen or recorded by camera. In addition, a *selective area* (SA) *aperture* can be inserted into the first image plane such that only waves with origin in a certain region of the specimen contribute to the diffracted spots.

One rather technical use of the diffraction mode is to orient a crystalline specimen in a way that the beam direction is along one of the high symmetry axes, which is a basic condition for high-resolution imaging of the crystal structure. A more analytical use case is the determination of the crystal structure and orientation of a crystalline specimen. This is especially useful in cases where the specimen does not allow for high-resolution TEM imaging either because it is too thick or consists of overlapping materials of different crystal structure or orientation that cannot be oriented into a suitable zone axis.[181, 182]

Since the diffraction pattern resembles the Fourier transform of the crystal lattice almost the same can be achieved by doing a *fast Fourier transform* (FFT) of a high-resolution TEM image of the crystal structure. It is not exactly the same as the image is a two-dimensional projection of the three-dimensional crystal and therefore in the FFT the influence of the crystal lattice in z direction is missing. Nonetheless it is sufficiently close in most applications and often allows to extract structural information from images that do not provide enough contrast in the image itself. Also it is superior to the recorded diffraction pattern in some cases as the smallest possible SA aperture can only limit the regarded specimen area down to the order of some hundred nanometres. Here the FFT comes in handy for example in areas with different crystal structures in close vicinity as it can be applied to a field of view of arbitrary size.

4.2.3 Scanning transmission electron microscopy (STEM)

Scanning transmission electron microscopy (STEM) has a fundamentally different working principle compared to conventional transmission electron microscopy which was initially proposed by von Ardenne [196]. Here the specimen is illuminated with a convergent beam that is focussed into an as small as possible spot – the so-called *electron probe* – in the specimen plane. After the beam has traversed the specimen it is projected onto a setup of integrating detectors (cf. Section 4.1.3) which record the electrons that have left the sample at a certain range of angles. The image in

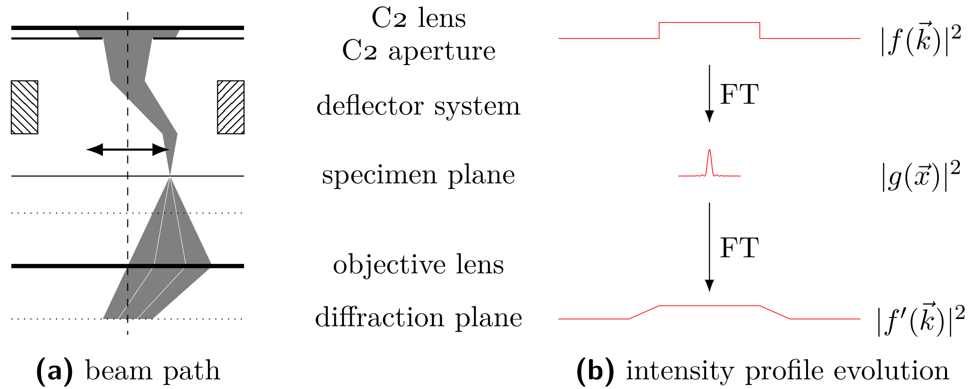

(a) beam path **(b)** intensity profile evolution

Figure 4.3: Schematic of (a) beam path and (b) intensity profile evolution in the STEM. (a): The conical beam whose convergence angle is determined by the C2 aperture is projected into a spot in the specimen plane and scanned by the deflector system. The exit cone which is broadened due to beam-sample interaction is projected back to the optical axis by the objective lens. The white lines within the exit cone mark the opening angle of the unbroadened cone. (b): By focussing the electron beam traversing the C2 aperture into a spot the rectangular intensity profile $f(\vec{k})$ is Fourier transformed (FT) into an Airy function $g(\vec{x})$ which, after interacting with the specimen, transforms back to a modified function $f'(\vec{k})$ of washed out rectangular shape.

this mode is achieved by scanning the electron probe in a grid pattern across the specimen and record the detector intensity for every probe position as one pixel of the final image. Therefore the image contrast arises just from the difference in recorded detector intensity of neighbouring pixels.

The technical principle of the scanning and the most important part of the beam path is depicted in Figure 4.3a. To achieve a focussed beam in the specimen plane the condensor system is used in convergent configuration (cf. Figure 4.1b) with the C2 aperture determining the convergence angle of the electron probe. The scanning is done with a deflector system which consists of a set of magnetic coils to shift the electron beam in the xy plane perpendicular to the optical axis. After traversing the specimen the beam diverges again and is additionally broadened due to scattering within the specimen. Seen from a wave optical point of view the specimen is illuminated by a convergent phase front that is superposed from a range of $\vec{k}$ vectors. The distribution $I_{\text{in}} = |f(\vec{k})|^2$ of those vectors is a rectangular function whose width depends on the diameter of the C2 aperture which determines the convergence angle of the electron probe. After interaction in the specimen the exiting beam cone contains a modified $\vec{k}$ vector distribution $I_{\text{out}} = |f'(\vec{k})|^2$ which then has to be measured.

Since the scanning system is built in a way that the electron probe traverses the specimen parallel to the optical axis the beam is projected back to the optical axis in the diffraction plane of the objective lens. The intensity profile in the diffraction plane is in first approximation the disc shaped image of the C2 aperture, this image is also known as *diffraction disc*. The further projection system of the microscope which projects the diffraction disk into the detector plane is operated in the same configuration as in the diffraction mode (cf. Figure 4.2b). It is not drawn in Figure 4.3a since it does basically only provide an additional scaling of the diffraction disc which is known as *camera length* setting. However, for the simplicity of the description it can be assumed that the detection system is located in the diffraction plane.[181, 182]

The detection system consists in most cases of a disc shaped *bright-field* (BF) detector concentrically surrounded by one or more ring shaped *dark field* (DF) detectors. The bright-field detector is placed with its center at the optical axis and its diameter is chosen such that it is primarily hit by the unscattered beam cone (cf. Figure 4.4a), hence specimen features that cause no or only light scattering appear bright and scatterers are dark in the image. The ring-shaped dark field detectors record electrons that have been scattered at a certain angle range with respect to the optical axis (Figure 4.4b). Accordingly, specimen areas that cause many electrons to be scattered into the angle range of the detector are imaged as bright features. More sophisticated detector designs as the differential phase contrast (DPC) system described in Section 4.3.1 give up on this simple rotational symmetric design to obtain additional information.[181]

For a high spatial resolution the diameter of the electron probe has to be as small as possible. Its intensity profile $|g(\vec{x})|^2$, also known as point spread function, is an Airy function since the beam profile in the focus point is the Fourier transform of the rectangular shaped intensity profile produced by the C2 aperture (cf. Figure 4.3b). The diameter, characterized by the full width at half maximum (FWHM) of the central maximum of the Airy function, depends on the diameter of the C2 aperture, the size and energy distribution of the electron source, and on the optical quality of the illumination system. This is contrary to TEM imaging where quality and resolution depend primarily on the projection system while the illumination system only has to provide sufficiently good illumination conditions. Current state of the art devices reach electron probe diameters down to 50 pm [197], whereas the typical probe diameter is in the order of 1 nm to 3 nm [198, 199] for the *Tecnai F30* used in this work.[181, 182]

The major strengths of scanning over conventional transmission electron microscopy are based in the serialized principle of scanning, i.e. that only a small spot on the specimen is illuminated at a time and the image is composed of the detector signals from these serially acquired illumination spots. While the image acquisition is serialized at the same time the data acquisition can be parallelized by recording the

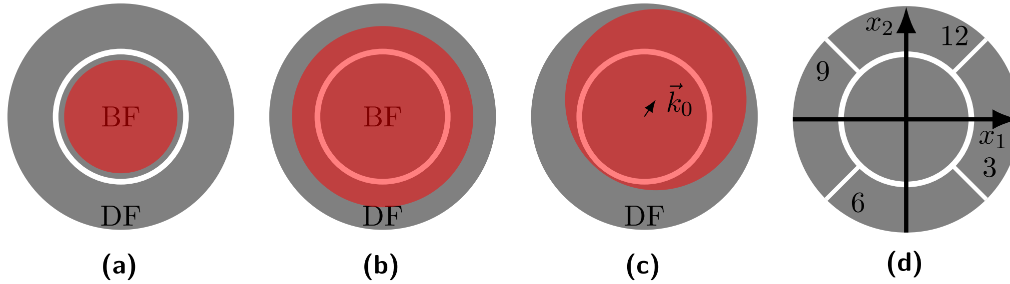

Figure 4.4: Comparison of a conventional circular STEM and the DPC detector. Without beam broadening (a) only the inner bright-field (BF) detector, with broadening (b) also the dark field (DF) ring is illuminated. An additional shift (c) by $\vec{k}_0$ does not change the intensity on the DF ring. A segmented DF ring (d) allows to detect the direction of the diffraction disc shift. The segments are numbered according to the numbers on a clock face, each pair of opposing segments defines an axis of a orthogonal coordinate system.

signal from several detectors at the same time to gain different types of information from the exact same specimen area. This is contrary to conventional transmission electron microscopy where the image generation is a parallel process but only one imaging technique can be employed at a time. Also, since the data acquisition in scanning transmission electron microscopy typically takes significantly longer – the exposure time of the CCD camera is typically in the order of a second while the recording of a good quality STEM image can easily be in the order of minutes – STEM imaging is affected stronger by device instabilities such as specimen drift or vibrations. On the other hand the imaging in STEM is not restricted to the detection of transmitted electrons, instead every effect that can be stimulated locally and for which a suitable detection system can be installed within the microscope – common methods are Auger and backscattered electrons, X-ray generation or cathodoluminescence – can be used to gain information about the specimen.[181] For this work, the analytical techniques differential phase contrast microscopy and energy dispersive X-ray spectroscopy have been used which will be explained in the following section.

4.3 Analytical Methods

4.3.1 Differential phase contrast microscopy (DPC)

Working principle

The description of the STEM contrast mechanism using conventional, rotation symmetric detectors as given in Section 4.2.3 is based on the assumption, that the

interaction of the electron probe with the specimen is dominated by unidirectional scattering which causes a broadening of the $\vec{k}$ vector distribution as depicted in Figure 4.4b. If the specimen contains electric or magnetic fields or has a thickness gradient the $\vec{k}$ vector distribution is shifted as a whole, corresponding to an addition of a constant $\vec{k}_0$ to the whole distribution: $I_{\text{out}} = |f'(\vec{k} - \vec{k}_0)|^2$. A simple shift of an unbroadened outgoing distribution (not drawn in Figure 4.4) would lead to a signal on the DF ring which is however indistinguishable from a disc broadening, while a shift of a broadened distribution as in Figure 4.4c would not necessarily cause an intensity change compared to the unshifted case (Figure 4.4b) since the overlap area of disc and detector ring is the same in both cases.

Breaking the circular symmetry by dividing the dark field detector into several individually addressable segments as shown exemplarily in Figure 4.4d enables the detector system to measure another degree of freedom: By comparing the signal intensities on the different sectors it gets possible to distinguish between unidirectionally scattered intensity and the shift of the whole diffraction disc. For electron microscopy this principle was theoretically proposed and experimentally realized in the 1970s.[200, 201] Since then it has been established as a technique for the characterization of magnetic structures.[201–204] Over the recent five years the method was also applied to characterize materials that contain internal electric fields,[197, 198, 205, 206] which is also the task it was utilized for in the course of this work to determine the spontaneous polarization of GaAs and GaP in Chapter 5.

The name *differential phase contrast* (DPC) microscopy for this technique is based on the fact that the signal measured by the detector and hence its contrast mechanism is proportional to the differential of the phase front of the exit beam cone. The detectors that are in use so far are custom made designs built for and retrofitted to existing instruments since only very recently the manufacturer *FEI* presented the first electron microscopes that can be equipped ex factory with a DPC system.[207] Among the used designs the four quadrant ring design drawn in Figure 4.4d, possibly with several concentric rings, is the most common detector configuration, however, different designs have been employed as well – some examples are shown and discussed in [208–210].

Data acquisition and analysis

In the instrument used in this work a custom built detector produced by *KE Developments* on order of *FEI* and Professor Zweck is used that consists of two concentric rings of four-quadrant detectors. The two-ring system was chosen to provide a greater flexibility concerning the samples and field strengths to measure, however, only the signals of one of the two detector rings are used at a time. The subsequent signal processing hardware was retrofitted to the microscope from partially off-the-shelf and partially custom-made electronics components, the data

acquisition software to control the whole scanning process and record images was developed in the work group initially by Uhlig [203] and revived by Lohr [198], where also the measurement setup is described in detail. The data processing, analysis and visualization of the measurement data is done using a software suite written for this purpose by Professor Zweck. The whole system has been calibrated for quantitative measurements of magnetic fields by Uhlig [203] and for electric fields first by Schregle [211] and Lohr [198] and in a more thorough way by Schwarzhuber [212]. Lohr [198] has also shown that the detector signal is linear over a wide range of deflection angles.

For the acquisition of a DPC dataset the electron probe is scanned across the specimen in a 1024^2 px grid and for every pixel the intensities on all four segments of the detector ring – in the following labelled $I_3(x, y)$, $I_6(x, y)$, $I_9(x, y)$ and $I_{12}(x, y)$ according to the numbers on a clock face – are acquired simultaneously with 16 bit resolution. To increase the *signal-to-noise ratio* (SNR) the recorded data is averaged over five consecutive measurements of 10 µs dwell time for every pixel. The resulting dataset of one measurement therefore contains four arrays of 1024^2 values each, one for every detector segment. By taking the intensity differences $\Delta I_{3,9}(x, y) = I_3(x, y) - I_9(x, y)$ and $\Delta I_{12,6}(x, y) = I_{12}(x, y) - I_6(x, y)$ of opposing sectors the part of the signal that is not caused by deflection but by other, unidirectional effects cancels out, leaving only the share in the signals that are due to a deflection of the electron probe, i.e. the $\vec{k}_0$ contribution to the whole signal.

The differences $\Delta I_{3,9}$ and $\Delta I_{12,6}$ represent then the vector components of the deflection vector $\vec{k}_0$ in the specimen plane perpendicular to the optical axis. If the deflection was caused by an electric or magnetic field then the sum of those vector components normalized by the sum $I_{\text{sum}}(x, y) = I_3(x, y)+I_6(x, y)+I_9(x, y)+I_{12}(x, y)$ of the signal intensities from all four segments is proportional to the field and the specimen thickness t the electron probe has traversed. In the electric field case this is

$$\frac{\Delta I_{3,9}(x, y)\hat{x}_1 + \Delta I_{12,6}(x, y)\hat{x}_2}{I_{\text{sum}}(x, y)} = \frac{1}{\kappa}\vec{E}_\perp(x, y)t(x, y) \tag{4.1}$$

with $\vec{E}_\perp$ being the field component of the electric field in the plane perpendicular to the optical axis and κ a device specific calibration factor that depends on the microscope and parameter settings used for the measurement. The normalization by I_{sum} is necessary since a change in overall intensity changes the difference signals $\Delta I_{3,9}$ and $\Delta I_{12,6}$ by the same factor, which can then be compensated by dividing by the sum intensity of all four detector segments.[198]

Solving Equation (4.1) for $\vec{E}_\perp$ yields the equation to calculate the electric field in the specimen from the acquired DPC data:

$$\vec{E}_\perp(x, y) = \kappa\frac{\Delta I_{3,9}(x, y)\hat{x}_1 + \Delta I_{12,6}(x, y)\hat{x}_2}{I_{\text{sum}}(x, y)t(x, y)}. \tag{4.2}$$

Here it should be noted that the formula originally given by Lohr [198] contains an additional term to take into account the gain of the amplifier chain, however, the later work by Schwarzhuber [212] showed that this factor is obsolete since it affects numerator and denominator of the fraction in the same way and hence cancels out. Above that he found out that for a given focal length of the objective lens κ does only depend on the camera length setting but not on the condensor aperture or amplification factors.[212]

The minimal measurable electric field depends strongly on the microscope settings used for the measurement as well as on the specimen thickness. With the parameters for which the setup has been calibrated it was determined to be in the order of $0.7\,\frac{\mathrm{V\,m}}{\mathrm{m}}$ which corresponds to $7\,\frac{\mathrm{MV}}{\mathrm{m}} = 7\,\frac{\mathrm{mV}}{\mathrm{nm}}$ for a specimen of 100 nm thickness with the set of microscope parameters that yield the best field resolution.[198, 211, 212]

In addition to the electric field determination it is possible to visualize a two-dimensional projection ρ' of the charge distribution that the electron beam has experienced on its way through the sample by taking the divergence of the electric field $\vec{E}_\perp$ as it was determined in Equation (4.2):

$$\rho'(x,y) \propto -\vec{\nabla} \cdot \vec{E}_\perp(x,y). \tag{4.3}$$

Such images which make it easy to see where charges accumulate in the sample will be called *charge distribution map* in the further reading.

Limitations

As attempts were made over the recent years to push the spatial resolution of DPC measurements down to atomically resolved imaging it turned out that the simple picture of having to measure just a $\vec{k}_0$ added to a broadened exit cone does no longer hold. Once the field – or more exactly the potential that causes the field – shows variations on a length scale comparable to the size of the electron probe this leads to a more fundamental redistribution of $\vec{k}$ vectors within the exit beam cone. In the detector plane this manifests itself in a redistribution of the intensity within the diffraction disc instead of a simple shift and since the ring detector omits a great portion of the $\vec{k}$ distribution the measured signal is then no longer proportional to the field acting on the electron probe. However, as the redistribution does on average still cause a shift of the centre of mass of the $\vec{k}$ distribution it can yet be detected by a segmented ring detector, but quantitative access is no longer possible with that setup.[197, 208, 213, 214]

To overcome this limitation several publications came to the conclusion that for a quantitative determination of fields at atomic or even sub-atomic length scales detector arrangements are necessary that provide a more fine-grained resolution of the $\vec{k}$ distribution. Proposed designs are either multiple segmented ring systems or pixelated detector arrays; the technical realization of both is still challenging in

terms of detector hardware as well as multi-channel signal acquisition and processing speed.[197, 208, 210, 213]

4.3.2 Energy dispersive X-ray spectroscopy (EDX)

If high energetic electrons enter a piece of matter they emit radiation in the X-ray range of the electromagnetic spectrum (1 pm to 250 pm), known as 'Bremsstrahlung', and, what is more important in this context, are able to knock out electrons from the low energy orbitals of the atoms they scatter with. As the missing electron gets replaced by one from a higher energy orbital it emits the difference in energy between its start and goal energy level as an X-ray photon. Since every atomic species has a unique distribution of discrete electron energy levels it also emits photons with a characteristic spectrum of energies. This property is used in energy dispersive X-ray spectroscopy (EDX, also referred to as EDXS or EDS) to identify the atom species contained in a material by their X-ray emission spectrum.[181, 182]

For this task the *Tecnai F30* is equipped with a commercially available *Bruker QUANTAX* EDX system with an *XFlash® 530* silicon drift detector [215, 216] with an energy resolution of 133 eV. Spatial resolution is provided in this context by using the STEM mode and exciting a small sample spot at a time which allows to assign the origin of the measured X-rays to the excitation spot or its close vicinity.

Unfortunately the whole process of both, X-ray generation and detection is quite ineffective: A specimen so thin that most of the electrons pass it without interacting at all is illuminated by an electron probe of preferably low intensity to achieve a high spatial resolution and statistically creates X-ray photons with a low probability. Of these rare photons only a small fraction arrives at the EDX detector that covers just a small solid angle around the specimen. For that reason EDX measurements in scanning transmission electron microscopy are typically a trade-off between spatial resolution, statistical significance and acquisition time. Since the recording times for substantiated measurements are in the order of several minutes, specimen drift in most cases limits the achievable acquisition time which puts also limitations on the other two factors.

4.4 Sample Preparation

Transmission electron microscopy requires the examined object to be 'electron transparent', i.e. it has to be thin enough that it can be traversed by high energetic electrons without experiencing significant absorption. Especially for imaging with high spatial resolution the general rule of thumb is that the specimen should be as thin as possible, typically well below 100 nm and in extreme cases even around 10 nm.[183] For samples which are in a bulk-like state as a result of their fabrication, for example planar epitaxial multi-layer structures, this typically requires extensive

specimen preparation either by thinning the bulk sample down to the required thickness by several grinding and polishing steps or by cutting thin lamellae from the material by focussed ion beam milling (FIB). Both methods are rather time-consuming with preparation times in the order of hours to days.[181, 182]

For nanowires, the situation is much easier in most cases. Since they are already of electron transparent thickness it is often sufficient to just remove the nanowires from their growth substrate and transfer them to a supportive structure. For the TEM measurements the supportive structure has to serve several purposes: It fixes the nanowires by van der Waals interaction, acts as electric conductor to direct charges towards the sample holder and therefore prevents charging of the irradiated specimen positions, and provides a carrier object that can easily be handled and fits into the specimen mount of the TEM sample holder. Above that it is desirable that the structure is mechanically stable under electron beam irradiation to prevent specimen drift during the measurement and it should influence the imaging as least as possible by causing only a weak background signal.

The supportive structures used for the measurements presented in this work are thin carbon films which are themselves disposed onto a copper grid for mechanical stability. The nanowires were transferred to these carbon coated grids by just wiping the grid over the as-grown sample. By doing so nanowires are randomly broken off the growth substrate and stick to the carbon film due to van der Waals force.

5 Spontaneous Polarization in the Wurtzite Phase of III–V Nanowires

In the following chapter, differential phase contrast microscopy as described in Section 4.3.1 has been employed to detect the spontaneous polarization of the wurtzite crystal phases of GaAs and GaP. These are, as shown in Section 3.2, both III–V semiconductors that grow typically in the non-polar zincblende crystal structure while their wurtzite form is in general only available in nanowires made of these materials. Hence the spontaneous polarization in the wurtzite phase of these materials has only been predicted theoretically but was not observed experimentally, yet. In addition, a simple simulation and a mathematical model of how the electron beam interacts with the detector geometry of the DPC system are developed to aid the interpretation of the experimental results.

The measurements presented in this chapter have been performed on GaAs nanowires grown by molecular beam epitaxy and on GaP nanowires that have been grown in metal-organic vapour-phase epitaxy. The former were produced by Joachim Hubmann in the MBE group of Professor Bougeard at *Universität Regensburg* while the latter were grown by Simone Assali from *Technische Universiteit Eindhoven*. A short description of the growth parameters can be found in Appendix A.

The results on the GaAs nanowires have been published in Applied Physics Letters [217], however, as will be shown in Sections 5.1.4 and 5.2.4, quantitative measurements of electric fields and hence of the polarization with DPC contain some pitfalls that were not expected at the time of publication. Therefore the quantitative value should be viewed critically since it is not possible to estimate its accuracy.

5.1 Detection and Quantification of the Spontaneous Polarization

5.1.1 Prerequisites

All measurements shown in this chapter have been performed with the respective nanowire oriented with a $\langle 11\bar{2}0\rangle$ (corresponding to $\langle 1\bar{1}0\rangle$ in the cubic indexing system) parallel to the electron beam as sketched in Figure 5.1. This orientation is beneficial for several reasons:

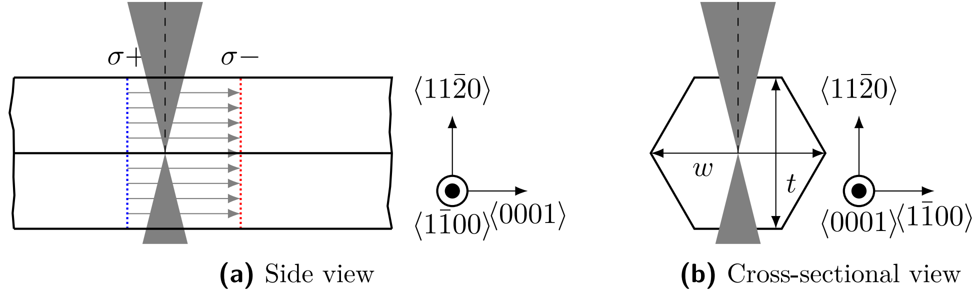

(a) Side view

(b) Cross-sectional view

Figure 5.1: Schematic sketch of the orientation of the nanowires towards the electron beam's optical axis. In both images the electron beam is visualized as a grey cone with the optical axis drawn as dashed line. (a) shows the side view of a segment of a nanowire that contains two layers of opposing charge $\sigma+$ and $\sigma-$ with an electric field in between them. The electron beam traverses this arrangement perpendicular to the electric field lines. In the cross-sectional view (b) the thickness t that is traversed by the electron beam and the width w that can be measured from the recorded images are indicated.

The polarization charge sheets are thought to form in {0001} planes (cf. Section 3.2.2) which means the electric field caused by these charge sheets is expected to build up along the [0001] direction (cf. Figure 5.1a). Since it is only possible to measure the vector component $\vec{E}_{\perp}$ perpendicular to the electric field it is advisable to irradiate the specimen with the electron beam perpendicular to the expected electric field direction to maximize its impact on the beam. The basic situation is sketched in Figure 5.1a for two clearly separated charge layers. To measure the spontaneous polarization within the crystal this condition is even more of importance since the separation of the single charge planes in III–V materials is well below 0.5 nm which is smaller than the electron probe size in the order of 1 nm to 5 nm. Therefore imaging of the polarization planes can only be achieved if the electron beam travels parallel to the charge planes.

The condition described above would basically be fulfilled for an arbitrary rotation of the nanowire around its [0001] axis. However, thickness gradients in the specimen cause the same signals in the DPC measurement as fields do. It is therefore useful to have a specimen that is free of such thickness gradients or where at least their shape is known. For most semiconductor nanowires, especially those presented here, this is easily achieved since it is known that they are of regular hexagonal shape with in most cases ⟨11$\bar{2}$0⟩ side facets.[218–221] This means that by orienting the nanowire in a ⟨11$\bar{2}$0⟩ zone axis it exhibits plane-parallel top and bottom surfaces in its central part that are entered by the electron beam perpendicularly, as can be seen in Figure 5.1b. In addition the specimen thickness t, which is needed for the

field quantification, can simply be calculated through geometric considerations from the imaged width w (cf. Figure 5.1b) as $t = \frac{\sqrt{3}}{2}w$ in this arrangement.

Another convenient side effect is that for high-resolution TEM imaging, which is employed accompanying to the DPC measurements to determine the crystal structure of the examined nanowires, the same zone axis orientation is chosen since this allows the most clear distinction between wurtzite and zincblende phase as well as between the two twinned orientations of zincblende (cf. Section 3.1.3).

5.1.2 GaAs nanowires

The first detection of spontaneous polarization that will be presented here stems from the tip of a GaAs nanowire which is shown in Figure 5.2. The nanowire, which was grown in the so-called 'pseudo-Ga catalyzed growth mode' [57, 222] is about 5.5 µm long with mostly zincblende crystal structure. Figure 5.2a displays the topmost part of the nanowire which, as a result of how the growth process was terminated, has a wurtzite crystal structure segment of about 400 nm at its upper end. The zone where the crystal structure switches can be recognized as streaky pattern near the lower image border of Figure 5.2a. At the very top of the wire sits a gold droplet which remains after all the gallium from the catalyst droplet has been consumed. The upper end where the crystal starts to get narrower was examined with HR-TEM (Figure 5.2b) to exactly determine the crystal structure: The left part exhibits the typical stripe pattern stemming from the $ABAB$ stacking order of the wurtzite crystal structure before the structure switches back to zincblende which is, however, interrupted by several defect planes.

Polarization detection

By looking at the same spot with DPC microscopy the charging situation is revealed: In the charge distribution map in Figure 5.3 which depicts integrated charge density $\rho' \propto -\vec{\nabla} \cdot \vec{E}_{\perp}$ (Equation (4.3)) the grey value is proportional to the charge state of the respective feature. In this representation uncharged regions appear in neutral grey while features that exhibit significant positive or negative charge appear brighter or darker.

It can easily be seen that the structural situation as depicted in Figure 5.2b is reproduced in the structure of the charge distribution. While the wurtzite region in the left half of the image features a streaky pattern of alternating bright and dark lines, corresponding to an alternation of positive and negative charges, the zincblende region appears as neutral albeit noisy grey. From the superimposed linescan profile it can clearly be seen that both, the wurtzite alternations as well as the noise in the zincblende areas oscillate around the zero line of the plot.

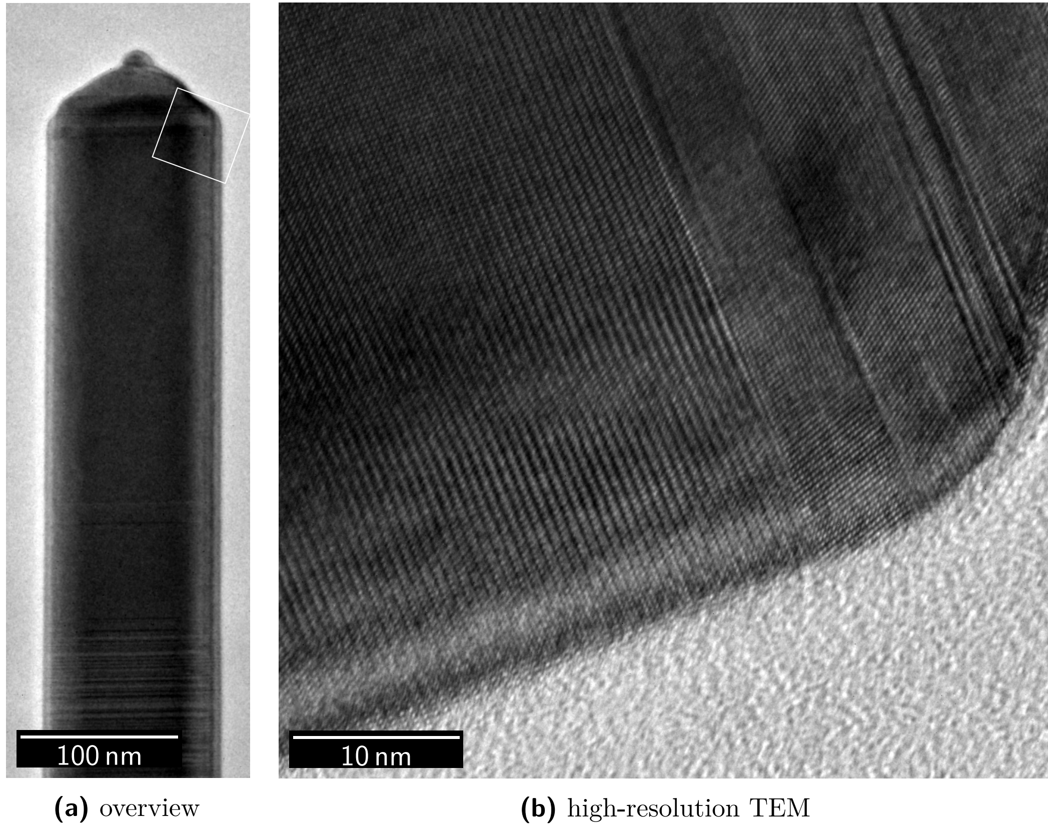

(a) overview **(b)** high-resolution TEM

Figure 5.2: TEM images of the tip of the GaAs nanowire where the measurements concerning the spontaneous polarization have been taken. (a) shows an overview of roughly the upper 400 nm of the wire with the crystal structure intermixing zone visible as streaky pattern close to the lower edge of the image and the gold droplet at the very top. The white square marks the area where the high-resolution TEM micrograph (b) was taken. Coming from the left edge there is first a region of wurtzite crystal structure, visible as clear stripe structure from the *ABAB* stacking, followed by a zincblende segment that is interrupted by several defect layers.

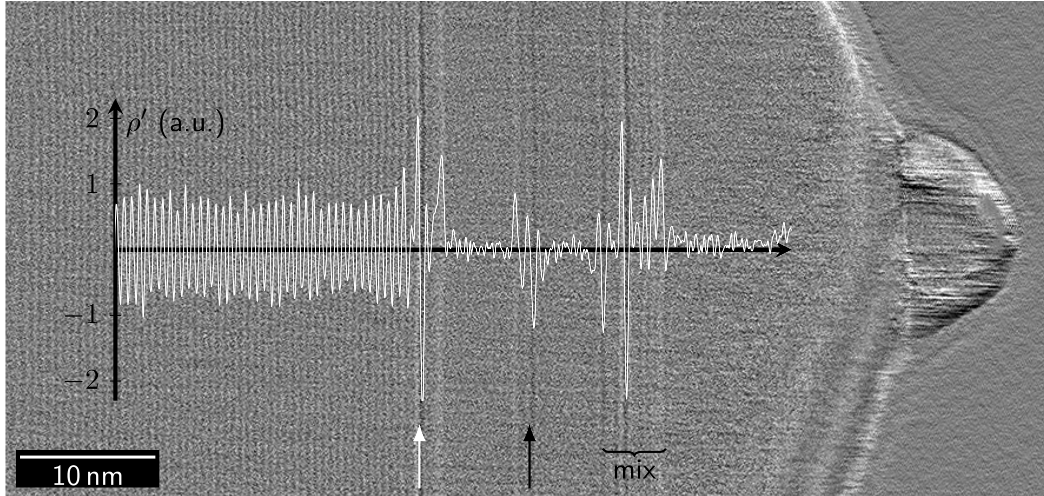

Figure 5.3: Charge distribution map of the GaAs nanowire tip at the transition from wurtzite to zincblende. A linescan profile is superimposed the image to allow for a more distinct judgement of the intensity variations. The wurtzite area on the left is characterized by alternating bright and dark stripes while the zincblende segments are of noisy but homogeneous grey with the defect planes in the zincblende part exhibiting rather random intensity fluctuations. The features at the specimen edge and within the gold droplet are artefacts due to electron optical distortions which are caused by the specimen surface curvature at the specimen edges. For the arrows and the brace annotation refer to the text.

However, additional features show up at the crystal structure interfaces that are not visible in the HR-TEM micrograph Figure 5.2b: the single defect line as well as the multiple, closely related defects that are indicated in Figure 5.3 by a black arrow and the black brace labelled 'mix', respectively, do not appear as distinct features but as a series of intensity variations without a clear correlation. Special attention should be turned to the interface between the wurtzite and the zincblende region, indicated by the white arrow, where two interesting aspects arise: the interface itself which is at the position of the arrow is accompanied by a brighter seam line that reaches approximately 1.5 nm into the zincblende and the charge density directly at the wurtzite-zincblende interface appears to be about twice as high as within the wurtzite.

The latter can easily be explained by comparing the size of the electron probe with the lattice constant of the examined crystal structure. The form of the electron probe is, as already mentioned in Section 4.2.3, an Airy disc with a FWHM in the order of 1 nm to 3 nm while the lattice plane spacing h_{hex} and hence also the

spacing of the charge planes in the wurtzite phase of GaAs is in the order of 0.3 nm (cf. Table 3.1). This means that at every image pixel the electron probe is averaging over several positive-negative transitions in the wurtzite crystal phase while the averaging effect is less strong at the interface where the electron probe sees partially the alternating charge structure of wurtzite and in part the uncharged zincblende. Hence it can be concluded that the positive-negative oscillation directly at the interface comes closest to the real charge accumulation. This means at the same time that it is not possible to extract the strength of the spontaneous polarization directly from the electric fields measured in the wurtzite phase since they will also be affected by this averaging effect. Besides that several publications have shown that one limitation of the four-quadrant detector setup used in this work is that it does not allow for quantitative field measurements under conditions where the potential landscape to be probed has significant variation on the length scale of the electron probe diameter, as already described in Section 4.3.1.[197, 208, 213, 214]

With the knowledge of this interaction of electron probe and charge plane spacing also the other features mentioned in the paragraph above get explicable: Whenever several charge planes are in close vicinity – closer than the probe diameter – but not in periodic order they are sampled with the probe profile as weight function which then is imaged as a charge distribution with nearly arbitrary progression.

Determination of the internal electric field and polarization strength

Since it is not possible to derive the spontaneous polarization directly from DPC data gained from the wurtzite crystal phase a different approach has to be taken where the measured electric field is not diminished by averaging effects. Ideally this was a capacitor-like structure with two oppositely charged planes with a constant electric field between them which would eliminate the problem of averaging as well as the limitations due to the curvature of the potential landscape. A candidate for such a structure are closely related twin defects in the zincblende crystal phase. It was argued in Section 3.1.4 (see especially Figure 3.7) that the smallest possible segment of wurtzite is formed by the twin stacking fault in zincblende, where the stacking order reverses from ABC to CBA or vice versa, which lets expect either one single charge sheet or two of opposing charge.

This type of arrangement can be found in the same nanowire from which already the data presented above was taken. Figure 5.4a shows a TEM micrograph of two twin defects about 35 nm apart. The fast Fourier transform of the image is presented in Figure 5.4b and exhibits the typical spot pattern of a twinned zincblende crystal structure with the spots corresponding to the (111) and $(\bar{1}\bar{1}\bar{1})$ planes annotated, which both stacking orders have in common since they are the basal plane of the growth direction. The other spots are not labelled, however the rather faint spots are highlighted with red and white circles. It is obvious that the (111)–$(\bar{1}\bar{1}\bar{1})$ axis

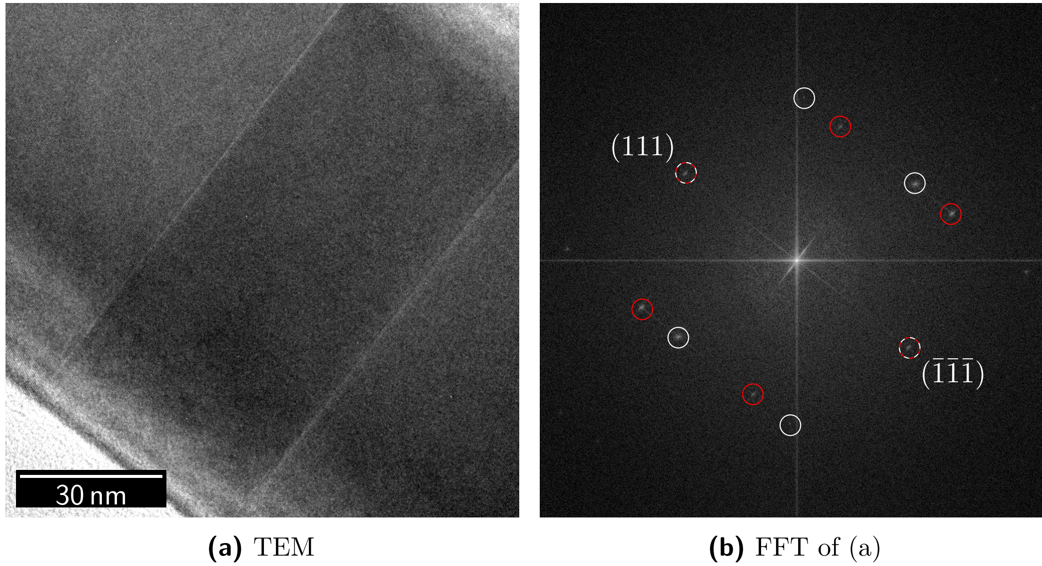

(a) TEM **(b)** FFT of (a)

Figure 5.4: Segment from the center part of the same nanowire as in Figure 5.2. In the micrograph (a) two twin boundaries about 35 nm apart are visible. The corresponding fast Fourier transform (b) confirms this by showing the typical doubled zincblende ($1\bar{1}0$) spot pattern. There the spots resulting from different crystal orientations in (a) are marked by red and white circles, respectively (see text for further explanation). The spots that both patterns have in common are labelled with crystal plane indices ((111) and ($\bar{1}\bar{1}\bar{1}$)) and marked by circles in alternating red-white.

acts as a mirror plane between the two spot patterns, where, as a result of the inversion of the stacking order, every spot of one colour is mirrored by a spot of the other colour. In this case the red ones originate from the central segment of the double twin structure in Figure 5.4a while the white ones belong to the two outer sections.

Looking at the charge distribution map (Figure 5.5a) of the same feature it can be seen that the left boundary has a contrast darker and the right one brighter than neutral grey, which indicates that either of the two defects represents a single sheet charge of one polarity. The DPC data has been taken only from the central part of the nanowire cross-section, where it exhibits plane-parallel top and bottom facets to avoid the influence of the prismatic side facets which would misleadingly be interpreted as electric field, as shortly described in Section 5.1.1. This arrangement resembles a capacitor with two plates of opposing charge and a dielectric in between. The fact that the separation of the charge sheets is less than half the nanowire diameter lets expect a homogeneous electric field in the region between them.

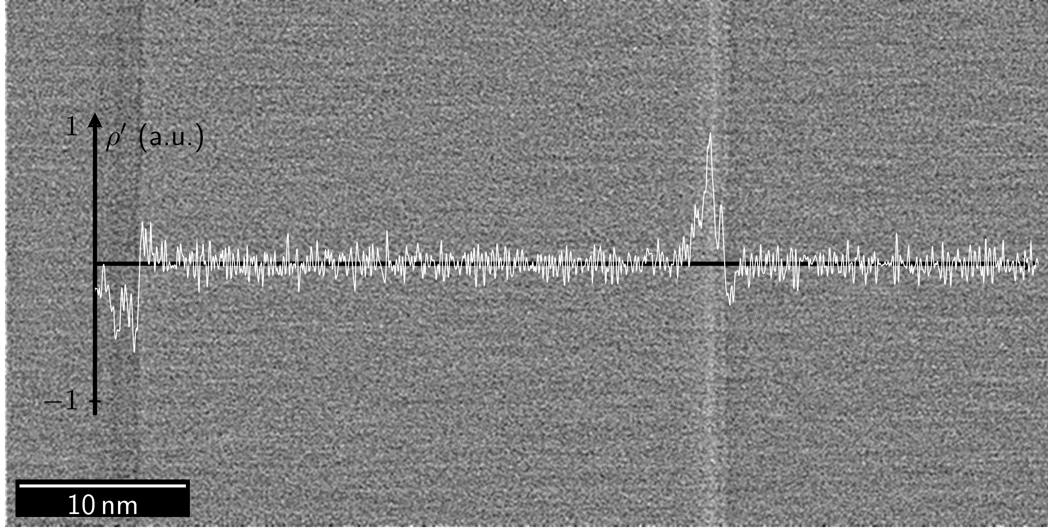

(a) charge distribution map

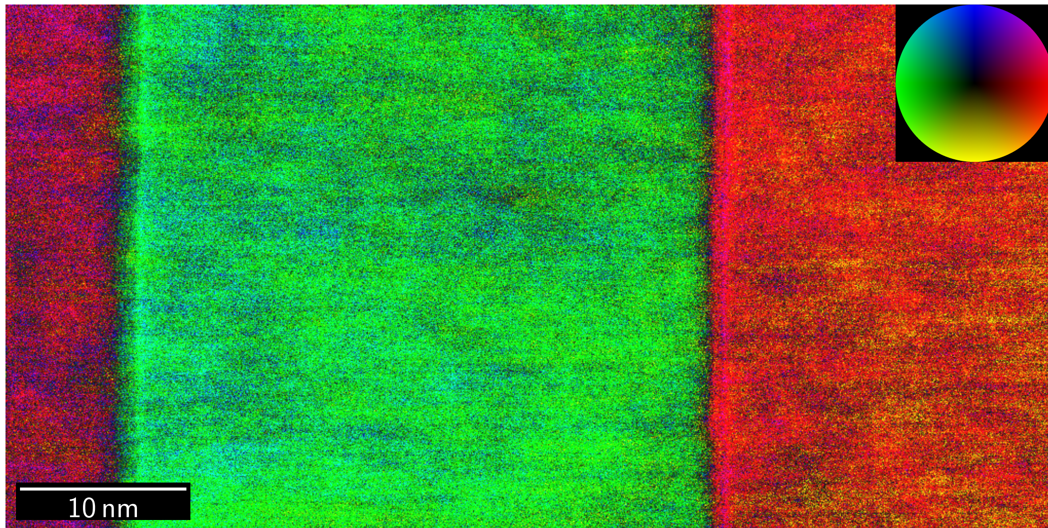

(b) field map

Figure 5.5: DPC imaging of the double twin defect: charge distribution map (a) with superimposed intensity profile showing the opposite charging of the defect planes and (b) depicting the electric field strength and direction according to the inset colour wheel. In the colour wheel the field direction is encoded as colour while the relative field strength is given by the brightness of that colour.

The assumption is confirmed immediately and in quite an obvious way through the colour coded map of the electric field depicted in Figure 5.5b where the colour and brightness represent the field direction and strength, respectively. In the map, which shows the electric field situation of the very same sample spot as the charge distribution map Figure 5.5a, it is clearly visible that the electric field inside and outside of the double twin structure points in opposite directions. Besides that it can at this point also be concluded that each twin defect carries only a single charge sheet since otherwise, if it carried two opposing sheets, the electric field would point into the same direction on both sides of the twin plane with only a small counter field in the opposite direction within the defect itself.

For a quantitative evaluation of the electric field line scan profiles across the double twin structure were taken from the difference data files containing the $\Delta I_{3,9}$ and $\Delta I_{12,6}$ data as well as the I_{sum} data file that are displayed in Figure 5.7. To reduce the noise level every data point was averaged over a width of 300 px which is feasible since the data does only vary along the line but can be considered constant perpendicular to it. The data gained from these line scans are plotted in Figure 5.6d. Comparing Figures 5.6a and 5.6b as well as their data plots it can be seen that by chance the specimen was oriented with respect to the detector coordinate axes in a way that the field is nearly parallel to one of the detector axes so that Figure 5.6b is nearly unaffected by the field and almost the whole field information is contained in Figure 5.6a. It can also be seen that both do not have a flat base line but contain a slope that is more pronounced in the $\Delta I_{12,6}$ than in the $\Delta I_{3,9}$ plot. This can be attributed to drift and non-linearities in the scanning system which cause the diffraction disc to slightly drift on the detector and manifest as an intensity gradient or 'shading' that is barely visible in the images but will later show up as a constant slope in the electric field. The data plot for I_{sum} does also show a slope of roughly the same magnitude as the $\Delta I_{12,6}$ curve, however, the per cent change and hence its influence on the later field determination will be much smaller since its base level is two orders of magnitude larger.

To quantify the electric field the calibration factor κ and the specimen thickness t are to be known in addition to the difference and sum signals. Since the dataset presented here has been recorded with the microscope parameters given by Lohr [198] also the calibration factor given there was used. However, since at a recalibration done by Schwarzhuber [212] it turned out that the calibration setup built by Schregle [211], who had given $\kappa = 38\,225/42\,\frac{\text{V m}}{\text{m}}$, was off by 25 % due to a fabrication inaccuracy, the calibration factor was modified accordingly to $\kappa = 38\,225/34\,\frac{\text{V m}}{\text{m}} \approx 1100\,\frac{\text{V m}}{\text{m}}$ to compensate for this erroneous calibration. Finally, the specimen thickness that was traversed by the electron beam was determined to be $t = (111 \pm 5)\,\text{nm}$ by the method described in Section 5.1.1.

Plugging all the data described into Equation (4.2) yields the electric field profile across the double twin structure which is presented in Figure 5.8. The error bars

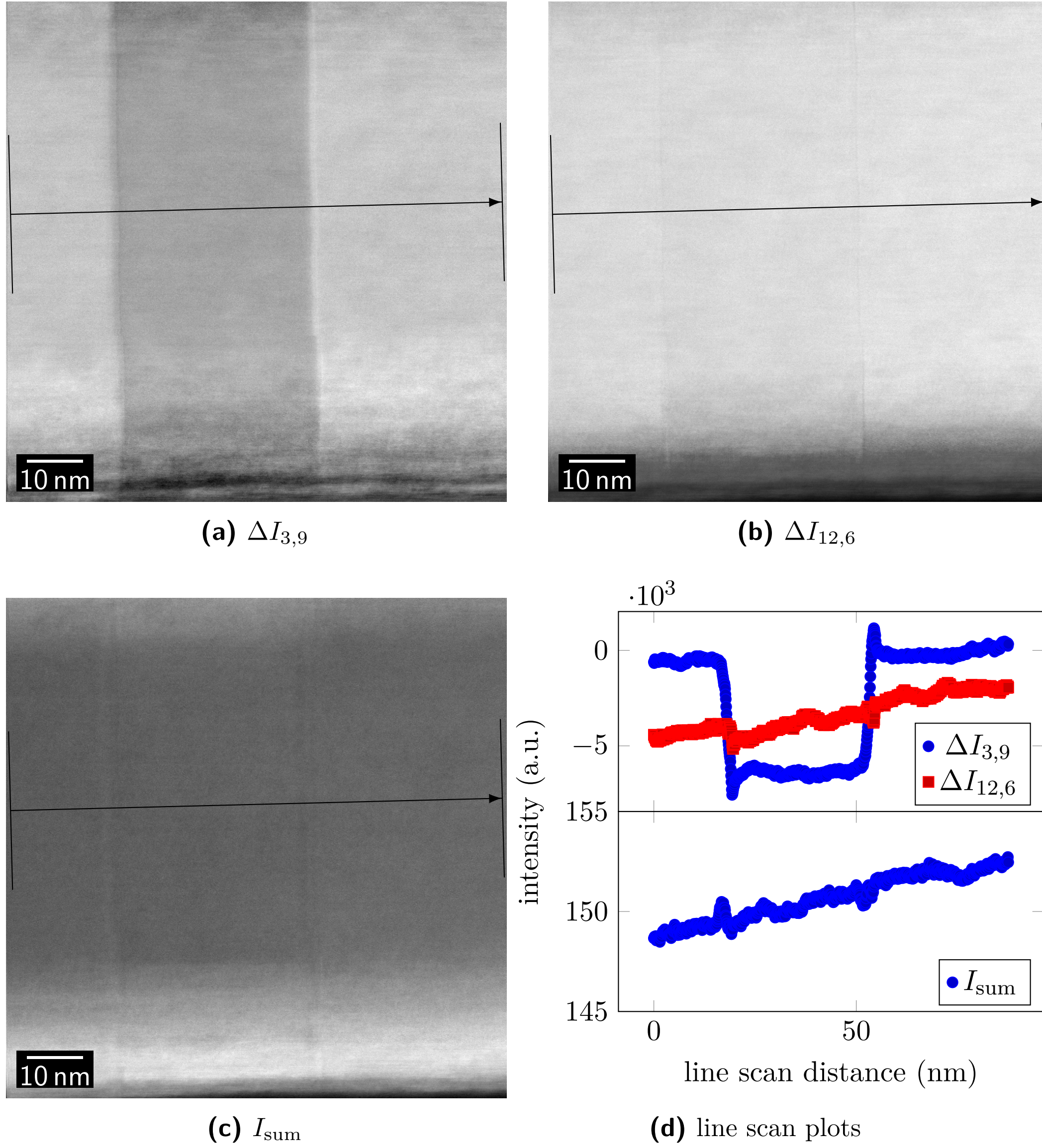

Figure 5.7: Raw difference ((a) and (b)) and sum intensity (c) data images of the double twin structure in GaAs. The arrows in the images denote the line and averaging width – indicated by the vertical bars at both ends – where the intensity profiles in (d) were taken from.

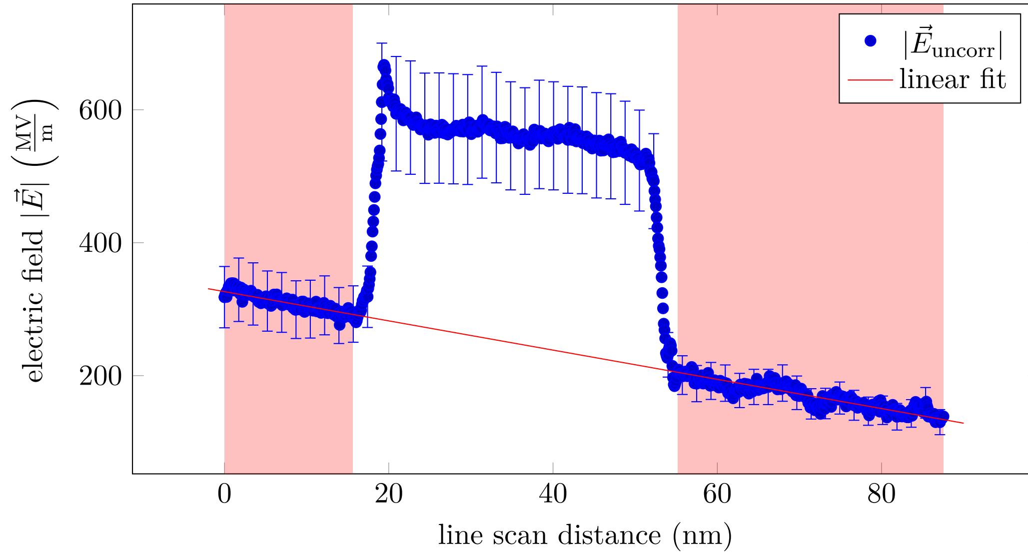

Figure 5.8: Uncorrected electric field across the double twin structure. The error bars contain the uncertainty of the DPC system and of the specimen thickness determination. Since the data is affected by an obvious slope stemming from drift in the optical system of the microscope, a linear fit was applied to the data highlighted by the red areas to create a bottom line.

correspond to an error of 14.5 % resulting from 10 % error margin of the DPC system and 4.5 % of the thickness determination. There are two aspects in this plot that attract attention: The whole plot curve is sloped and it is not close to zero as one would expect it since the field should cross the zero line at the position of the twin defects. The latter has two reasons: First, the DPC system is only capable of measuring relative electric fields, i.e. the value that is interpreted as zero field depends on how exact the diffraction disc was centered on the detector in field-free conditions. Second, since the form of Equation (4.2) produces the absolute value of the electric field it appears appropriate to shift the raw difference curves (cf. Figure 5.6d) completely either into the positive or negative by applying a constant offset, otherwise the resulting field curve would be hard to interpret. In this case this was only necessary for the $\Delta I_{3,9}$ curve which was shifted into the negative by an offset of -1500 before feeding it into Equation (4.2).

The slope is, as already mentioned before, a result of the scanning system and is superimposed to both the inside and the outside regions of the double twin structure in the same manner. Since only the height of the steps at the twin boundaries is the quantity of interest, this does not affect the quantitative result but complicates the evaluation. To remove the slope and create a constant base line a linear fit

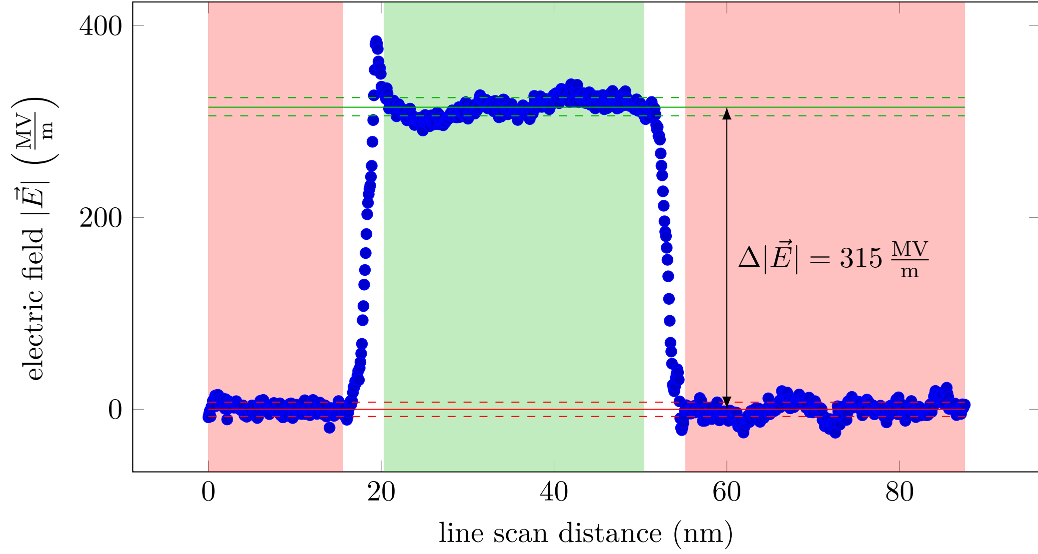

Figure 5.9: Plot of the electric field across the double twin structure after slope removal. The areas highlighted in red and green correspond to the accordingly coloured areas shown in Figure 5.5b and the red and green solid lines indicate the mean value of the electric field within the respective areas with their standard deviation indicated by dashed lines.

was applied to the outer regions which are highlighted with red background in Figure 5.8 and the fit values were subtracted from the whole data curve. In the resulting graph, which is depicted in Figure 5.9, the regions inside and outside of the double twin structure are highlighted with green and red background, respectively, in correspondence to the electric field map. Directly around each twin boundary a 5 nm wide segment is excluded where measurement artefacts such as the overshoot at around 19 nm appear. To derive the step height from the plot the mean values were taken from the region highlighted in green as well as the two red ones combined. Those values are indicated by the solid green and red lines with their standard deviation shown as dashed lines. This yields a difference of the mean electric field inside and outside the double twin structure of $\Delta|\vec{E}_{\text{mean}}| = (315 \pm 17)\ \frac{\text{MV}}{\text{m}}$. Adding up the error margin of the DPC system and the thickness determination of 14.5 % this results in an electric field difference $\Delta|\vec{E}| = (315 \pm 70)\ \frac{\text{MV}}{\text{m}}$ between inside and outside the double twin structure.

Due to the separation of the two twin defects of about 35 nm being significantly smaller than the size of the charge plane which is more than 100 nm it can be assumed that this structure behaves like a parallel plate capacitor filled with a dielectric material – GaAs in this case. The electric field inside such a capacitor

can, in the absence of an additional external electric field, be described as

$$E = \frac{1}{\varepsilon_0 \varepsilon_r} P \tag{5.1}$$

with the vacuum permittivity $\varepsilon_0 = 8.85 \cdot 10^{-12}\,\frac{\mathrm{F}}{\mathrm{m}}$, $\varepsilon_r$the relative permittivity of the dielectric, and P the polarization strength of the capacitor plates. The only polarization that can be expected at the twin boundaries is the spontaneous polarization P_{sp} since the crystal is unstrained and therefore piezoelectric polarization can be excluded (cf. Section 3.2.2). Hence the spontaneous polarization can be derived from the measured electric field by

$$P_{\mathrm{sp}} = \varepsilon_0 \varepsilon_r |\vec{E}| \tag{5.2}$$

with $\varepsilon_{r,\mathrm{GaAs}} = 13.17$ being the relative permittivity of GaAs.[223] For the electric field derived for the double twin structure this yields finally a spontaneous polarization of

$$P_{\mathrm{sp,GaAs}} = (0.037 \pm 0.008)\,\frac{\mathrm{C}}{\mathrm{m}^2}. \tag{5.3}$$

The value differs from the result published in Bauer *et al.* [217] which is based on the same measurement for two reasons: In a recalibration of the DPC system done after the publication it turned out that the electric field that was used for the calibration was off by 25 % due to fabrication tolerances in the calibration setup and it also turned out that the influence of the amplifier chain that was assumed at the time of the publication cancels out, which changes the result by an additional factor of 9.7 (cf. Section 4.3.1).

In comparison with the values of $P_{\mathrm{sp,GaAs}} \approx 0.003\,\frac{\mathrm{C}}{\mathrm{m}^2}$ given in the literature [98, 147], which have been obtained by DFT calculations (see Section 3.2.4) it turns out that the value measured by DPC is about one order of magnitude larger than the theoretical predictions. We will leave this result uncommented for now and will pick it up again in Section 5.1.4 for further discussion.

5.1.3 GaP nanowires

A second example to be presented here are GaP nanowires grown via MOVPE by Simone Assali from *TU Eindhoven*. By a special growth process which is shortly described in Appendix A.2 it is possible to grow a series with segments of zincblende crystal phase with up to 10 nm length into nanowires of otherwise wurtzite structure. A high-resolution TEM overview of the full length of the segment series containing 13 zincblende segments in total is depicted in Figure B.1 in the Appendix. However, since the zincblende segments get subsequently thinner over the course of the segmented growth, only the first few ones are thick enough to perform measurements with sufficient statistics on them.

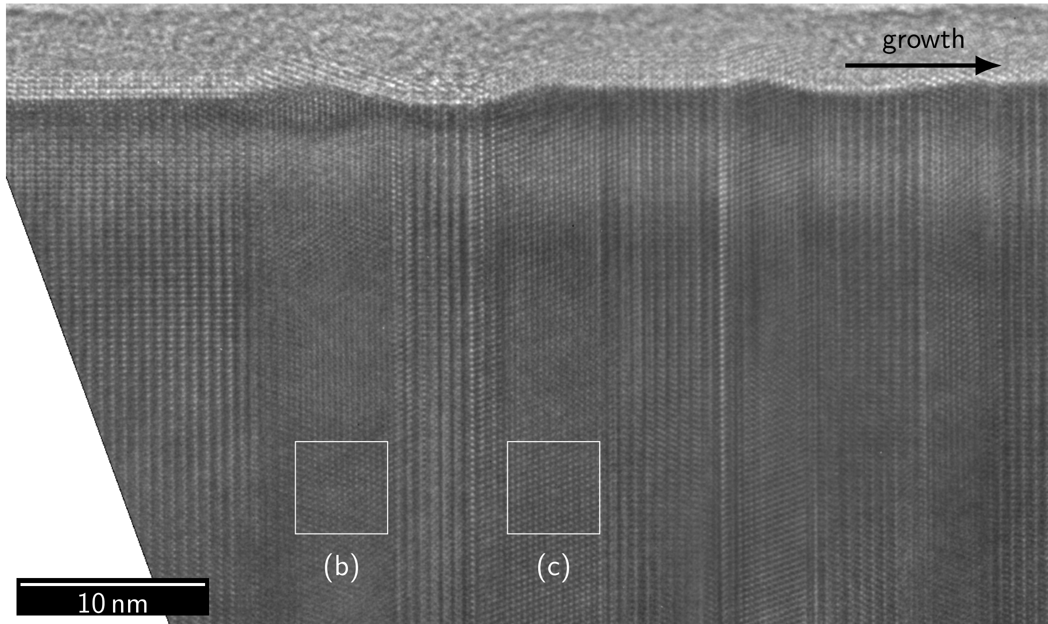

(a) high-resolution TEM

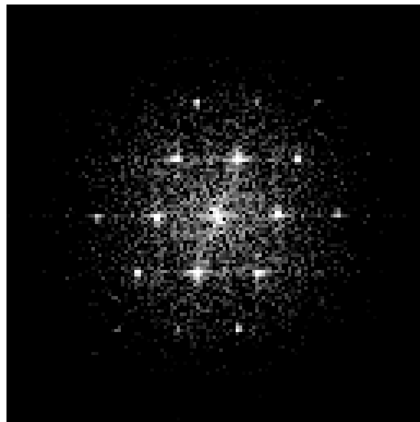

(b) FFT of left square

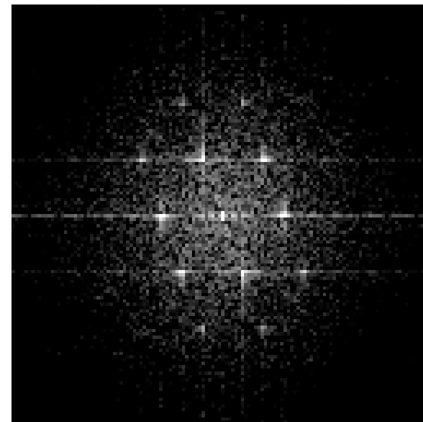

(c) FFT of right square

Figure 5.10: High-resolution TEM micrograph of the beginning of the zincblende segment region in the otherwise wurtzite GaP nanowire. In (a) the first four zincblende segments in growth direction are depicted. (b) and (c) are the fast Fourier transforms of the two square annotations in (a) showing that the first two zincblende segments have opposite stacking order.

Figure 5.10a contains a high-resolution TEM micrograph of the beginning of such a segment series with the first four zincblende segments, which are from left to right, i.e. along the growth direction, 9 nm, 8 nm, 5 nm, and 4 nm thick separated by 4 nm to 6 nm thick segments of wurtzite. From the white squares drawn in the first two zincblende segments fast Fourier transforms (Figures 5.10b and 5.10c) have been taken from which it can be derived that the stacking in those two segments is of opposite order, since the spot patterns are mirror-inverted towards each other.

A second point that stands out is that the specimen edge is not straight but kinks up and down either at the zincblende-wurtzite interfaces or within the zincblende segments. This lets expect that also the side facets of the nanowire are not perfectly plane-parallel but have a similar topography which should result in a thickness modulation as well as artefacts in the DPC signals due to the prismatic surface structure. The former argument can be rebutted since the thickness variation is in the order of 1 nm and hence only about 1 % of the overall nanowire thickness which was determined to be (110 ± 10) nm. In Figure 5.10a the variation is just misleadingly exaggerated by the display window that shows only the outermost portion of the nanowire width. The second issue should also be easily addressable as the DPC signal caused by prismatic structures is proportional to the slope of the thickness variation.[205] Since the outer surface seems to be not continuously rounded but a set of facets angled towards each other, this should in the DPC signal at worst result in a series of plateaus that superimposes the features resulting from the electric field itself.

A mapping of the electric field across the first five zincblende segments depicted in Figure 5.11 reveals a field within the zincblende segments parallel to the growth direction and a very weak field pointing opposite in the wurtzite parts. It should be noted here that compared to the GaAs data the GaP DPC dataset presented here has been recorded with a C2 aperture of smaller diameter (see Sections 4.1.2 and 4.2.3) in place which results in a wider electron probe which averages away the ripples normally seen in the wurtzite crystal phase. The averaging has the advantage that the DPC signal in the wurtzite segments can be considered field-free and hence can serve as reference level for the field determination. Other measurements performed on these nanowires with a smaller beam diameter, which are not shown in this work, do show the same oscillating charge density in the wurtzite parts of the crystal as described for GaAs. The full parameter sets used for the DPC measurements presented in this work on both materials are summarized in Table B.1 for comparison.

To determine the internal electric field the same steps as described for GaAs in Section 5.1.2 have been performed on a line scan profile extracted from the DPC raw data along the line drawn in Figure 5.11. Since the processing was done in analogy to the GaAs case the respective raw data images and plots (Figures B.2 to B.4) have been placed in Appendix B.2. The resulting field plot using a calibration

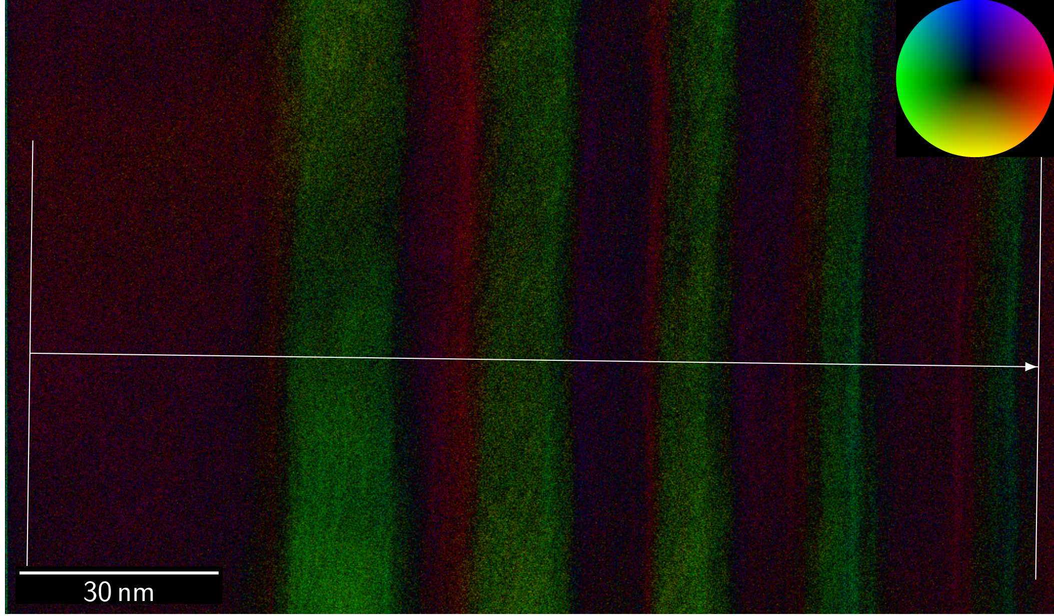

Figure 5.11: Colour-coded map of the electric field situation across the first five zincblende segments of the GaP nanowire. Field strength and direction are encoded in brightness and colour, respectively, according to the colour wheel insert in the upper right corner. The white arrow with the bars at both ends denotes the position and averaging width of the line scan profile that was taken from the raw data for field quantification.

factor $\kappa = 935$ and specimen thickness $t = (110 \pm 10)\,\mathrm{nm}$ (cf. Table B.1) is shown in Figure 5.12. As can be seen there only the first two zincblende segments (highlighted with green background) are wide enough to exhibit a clearly recognizable bottom line while the segments further right do have a V-shaped form which is due to their width being close to the electron probe size. Therefore only the first two segments are used to determine the internal electric field. The difference in the mean values between wurtzite and zincblende can be determined from the plot to be $|\Delta\vec{E}_{\mathrm{mean}}| = (1650 \pm 280)\,\frac{\mathrm{MV}}{\mathrm{m}}$, which results together with the errors from DPC and thickness determination in $\Delta|\vec{E}_{\mathrm{wz,zb}}| = (1700 \pm 500)\,\frac{\mathrm{MV}}{\mathrm{m}}$. However, since the field was not determined between two adjacent zincblende segments separated by a twin plane but between zincblende segment and wurtzite, where the wurtzite was averaged down to zero by the recording technique, $\Delta|\vec{E}_{\mathrm{wz,zb}}|$ covers only half of the full field amplitude which is then $\Delta|\vec{E}| = (3400 \pm 1000)\,\frac{\mathrm{MV}}{\mathrm{m}}$. With $\varepsilon_{r,\mathrm{GaP}} = 11.11$ [224, 225]

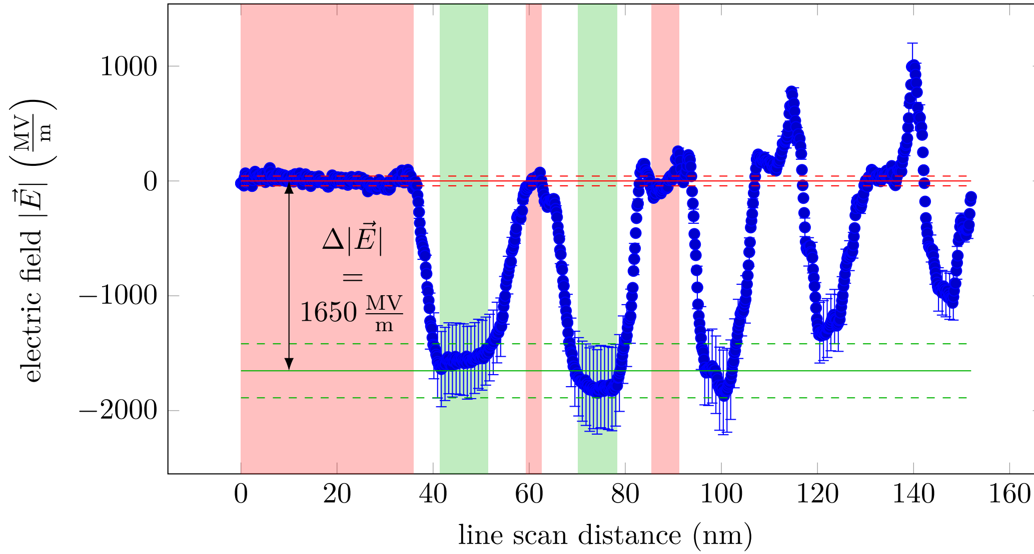

Figure 5.12: Electric field plot across the first five zincblende segments of the GaP nanowire. The error bars correspond to an error of 20 % and are smaller than the plot symbols close to the zero line. Also only every fifth data point is drawn with an error bar to make the plot less crammed, hence the two upward spikes close to the right side of the plot do by chance not have error bars on them. Red and green lines denote the average upper and lower levels of the electric field with their standard deviation indicated by dashed lines in the same colour. The data regions where the averages have been taken from are highlighted with a background in the respective colour.

this yields a spontaneous polarization

$$P_{\mathrm{sp,GaP}} = (0.32 \pm 0.09)\,\frac{\mathrm{C}}{\mathrm{m}^2}. \tag{5.4}$$

Compared to the values found in the literature [98, 147, 152] of 0.003 $\frac{\mathrm{C}}{\mathrm{m}^2}$ to 0.008 $\frac{\mathrm{C}}{\mathrm{m}^2}$ (see Section 3.2.4) the result determined by DPC is off by two orders of magnitude and hence even further than in the GaAs case.

5.1.4 Discussion

Looking at the results presented in the sections above, the questions that arise are on the one hand whether the oscillating behaviour of the DPC signal is really caused by charge sheets – and not simply by the crystal structure itself – and on the other

hand why the measured internal electric fields and polarization strengths are so far off the literature values. Those questions will be addressed in the following.

DPC contrast formation in the wurtzite structure

To challenge the assumption that the image contrast in the wurtzite phase is just a result of the crystal structure, i.e. the spatial arrangement of the atoms, it makes sense to have a look at the conditions that are required for crystal structure imaging by scanning transmission electron microscopy.

If the convergent electron beam probe enters a crystalline specimen it is affected by Bragg diffraction in the same way as a parallel electron beam. However, it does not generate the typical Bragg diffraction pattern with delta-peak like spots known from plane wave diffraction, but a pattern that is in first order a convolution of the circular STEM diffraction disc with the Bragg spot pattern. The result is a so-called *convergent electron beam diffraction* (CBED) pattern consisting in first approximation of a arrangement of circular intensity discs with their centers at the positions where the spots are located in the Bragg diffraction pattern (for an example, see Figure 5.14). The radius $r_{\mathrm{disc}} = \theta \cdot L$ of the intensity discs in the detector plane is determined by the product of the camera length L and the convergence semi-angle θ which itself depends on the diameter of the C2 aperture (see Sections 4.1.2 and 4.2.3). Their separation s_{hkl} can be derived from the Bragg equation for small diffraction angles and for the first diffraction order to be $s_{hkl} = \frac{\lambda \cdot L}{d_{hkl}}$ with $\lambda_e = 1.57\,\mathrm{pm}$ being the wavelength of electrons at 300 keV and d_{hkl} the lattice plane separation of the crystal direction $[hkl]$ causing the respective diffraction spot.[181, 182]

A necessary condition to achieve phase contrast and hence crystal structure resolved imaging according to Williams and Carter [181] is that the zero and first order discs overlap on the detector area which means that the separation s_{hkl} has to be smaller than twice the radius r_{disc} or

$$\frac{s_{hkl}}{r_{\mathrm{disc}}} = \frac{\lambda}{d_{hkl} \cdot \theta} < 2. \tag{5.5}$$

For the measurements shown in this work C2 apertures with convergence semi-angles of either $\theta_{\text{‘}3\text{’}} = 1.5\,\mathrm{mrad}$ (C2 aperture number ‘3’, see also Table B.1) or $\theta_{\text{‘}2\text{’}} = 0.5\,\mathrm{mrad}$ (C2 aperture number ‘2’) have been used. The lattice spacings of interest are the values for h_{hex} for the lattice plane separation in [0001] direction of wurtzite, which can be taken from Table 3.1 to be in the order of 0.3 nm for both, GaAs and GaP. Entered into Equation (5.5) this yields $\frac{s_{hkl}}{r_{\mathrm{disc}}} = 3.3$ for the C2 aperture ‘3’ with the larger convergence angle of 1.5 mrad which means that the separation between the diffracted discs is more than three times the radius of the discs. This is in contradiction to the assumption that the contrast is primarily resulting from the crystal structure via a phase contrast mechanism.

Another influence that cannot be excluded for sure is a possible redistribution of intensity within the diffraction disc, resulting in a non-homogeneous brightness of the disc. However, as has been shown by Müller *et al.* [197] and Galioit [213], this does qualitatively produce the same result as a simple shift of the diffraction disc. Instead, it does only inhibit a quantitative access to the polarization strength directly in the wurtzite structure which is already hampered by the averaging effect caused by the interplay of electron probe size and lattice plane spacing as described in Section 5.1.2.

Since the two points discussed above have either been invalidated or do not have an influence on the qualitative results, it can be concluded that the oscillatory behaviour of the DPC signal is really caused by the charge planes introduced by the spontaneous polarization.

Considerations on the quantitative field measurements

Concerning the quantitative measurement of the internal electric fields and the resulting values for the spontaneous polarization it has to be stated that those are one to two orders of magnitude above the values found in the literature. They are therefore comparable to or even exceed the values that are given for the spontaneous polarization of the III-Nitrides, the model material system for polarization effects. Since the measured values appear highly improbable from this perspective, it has to be discussed why they are that large and if they are realistic.

A first hint about what could be of influence here can be drawn from the intensity distribution in the detector plane. The works done on quantitative DPC and setup calibration[211, 212] were performed under the assumption that the diffraction disc in the detector plane has not experienced a significant change in size or intensity distribution but basically only a uniform reduction in intensity due to absorption.

However, it turns out that this criterion does not hold for the nanowire samples presented in Section 5.1. Figure 5.13 depicts a typical example of how the intensity distribution looks like in the detector plane with a nanowire specimen in place. For this purpose an image of the 'diffraction disc' or the remains thereof was taken using the CCD camera of the microscope which normally is used to record images in non-scanning mode. In the image the original diffraction disc resulting from electrons that have not scattered within the specimen can be seen as circular shape shifted slightly left below the image center and brighter than the remaining features. Superimposed is a more diffuse pattern that spreads considerably wider than the disc itself and is caused by *dynamical diffraction* which occurs when electrons are scattered elastically multiple times on their way through a crystalline specimen.[181, 226] Dynamical diffraction does not make a significant contribution to the intensity distribution for typical specimens which are prepared to be only some tens of nanometres thick in the investig-

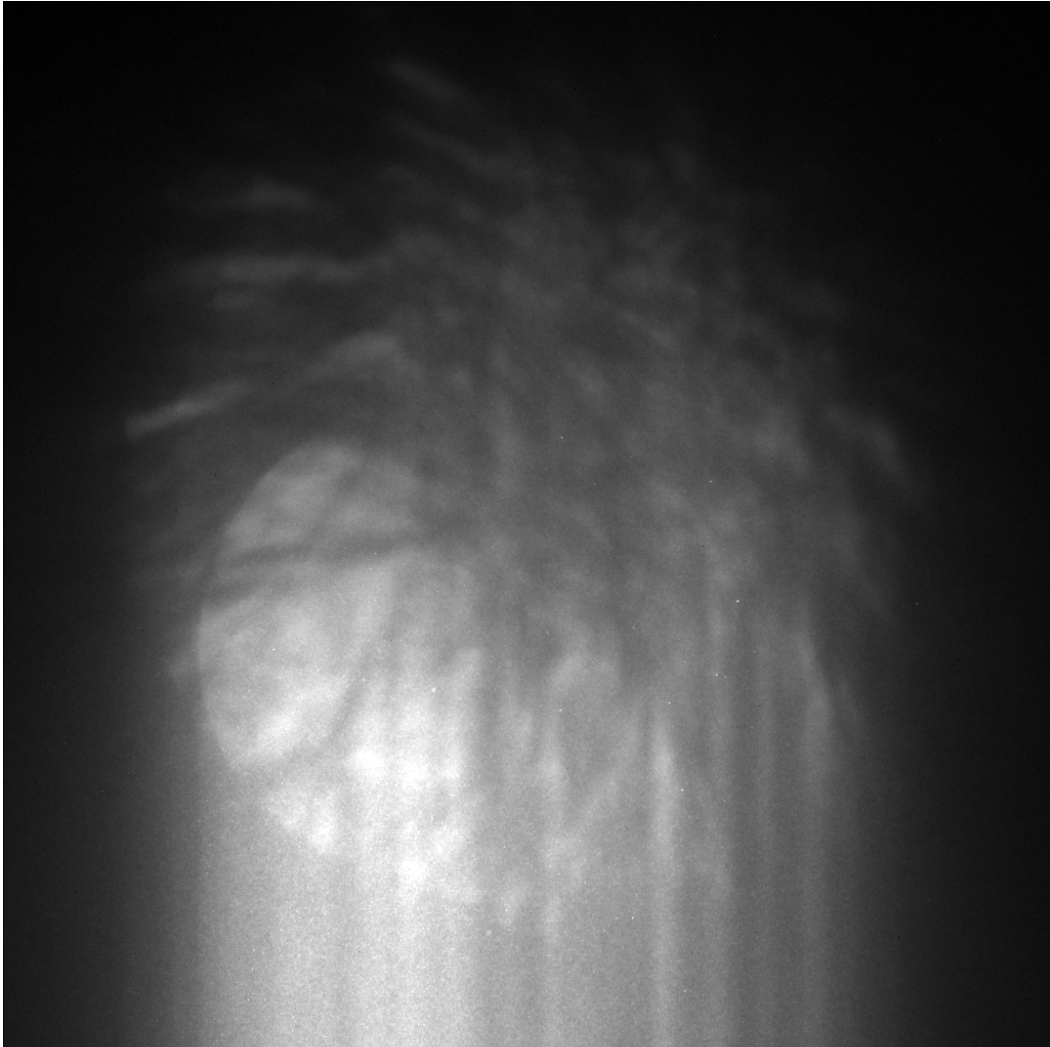

Figure 5.13: Typical intensity distribution of the 'diffraction disc' recorded on CCD camera in the detector plane after the beam has traversed a nanowire specimen. The original diffraction formed by electrons that have not been scattered within the specimen is still partially visible as brighter circular shape left below the image center which is superimposed by a diffuse pattern due to dynamical diffraction. The vertical bright streaks in the lower image half are smear artefacts resulting from the readout cycle of the CCD camera.

ated region, but at the thickness of the nanowires measured here it apparently does.

It should be noted that in Figure 5.13 there is a displacement between the centers of mass of what was identified as the original diffraction disc and the dynamical diffraction pattern. Also the dynamical pattern exhibits a significant asymmetry as it has concise, filament-like extensions towards the left edge and lower left corner of the image which do not show up towards the upper right corner. Both are an effect of the fact that the specimen was not aligned exactly in zone axis. For a perfectly aligned specimen the pattern from the dynamical diffraction would be axially symmetric and contain basically the symmetry of the crystal structure it was caused by, however, with a strong variation in intensity. Above that, the centers of mass of both, diffraction disc and dynamical diffraction pattern, would be at the same position.

In conclusion that means that for the specimens presented in this section the measurements were performed under conditions where there was no sharply defined and uniformly bright diffraction disc in the detector plane. Instead it was a considerably wider, diffuse intensity distribution that has significant fluctuations which contain an axial symmetry. This brings up the additional question whether the signal that was measured is really due to electric field within the sample or if it could instead be a result of intensity variations in the diffraction disc that are caused by the crystal structure. To address this issue as well as the one concerning the large measured fields, the influence of the intensity distribution within the diffraction disc pattern on the DPC detector is examined in a more theoretical way in the following section.

5.2 Factors Influencing Quantitative DPC Measurements

5.2.1 Simulation setup

For this purpose the elements depicted in Figure 5.14 were generated: a single detector segment (Figure 5.14a) as well as five diffraction disc patterns (Figures 5.14b to 5.14f). Here Figures 5.14e and 5.14f are simple diffraction discs (cf. Section 4.2.3) which both have constant brightness over their whole area but differ by their radius and brightness level. They are designed to have the same integral intensity I_0 which means that the ratio of their brightness – which relates to the current density j in electron microscopical terms – is inversely proportional to the square of their radii. Figure 5.14e serves as the reference here to which the other patterns are related and is therefore labelled 'reference disc' or simply 'reference' in the following, while Figure 5.14f is increased in radius by 10 % which results in a reduction of the brightness to 83 %.

Figures 5.14b to 5.14d are simplified CBED patterns as explained in Section 5.1.4 which have been generated by putting circles with the radius of the reference disc

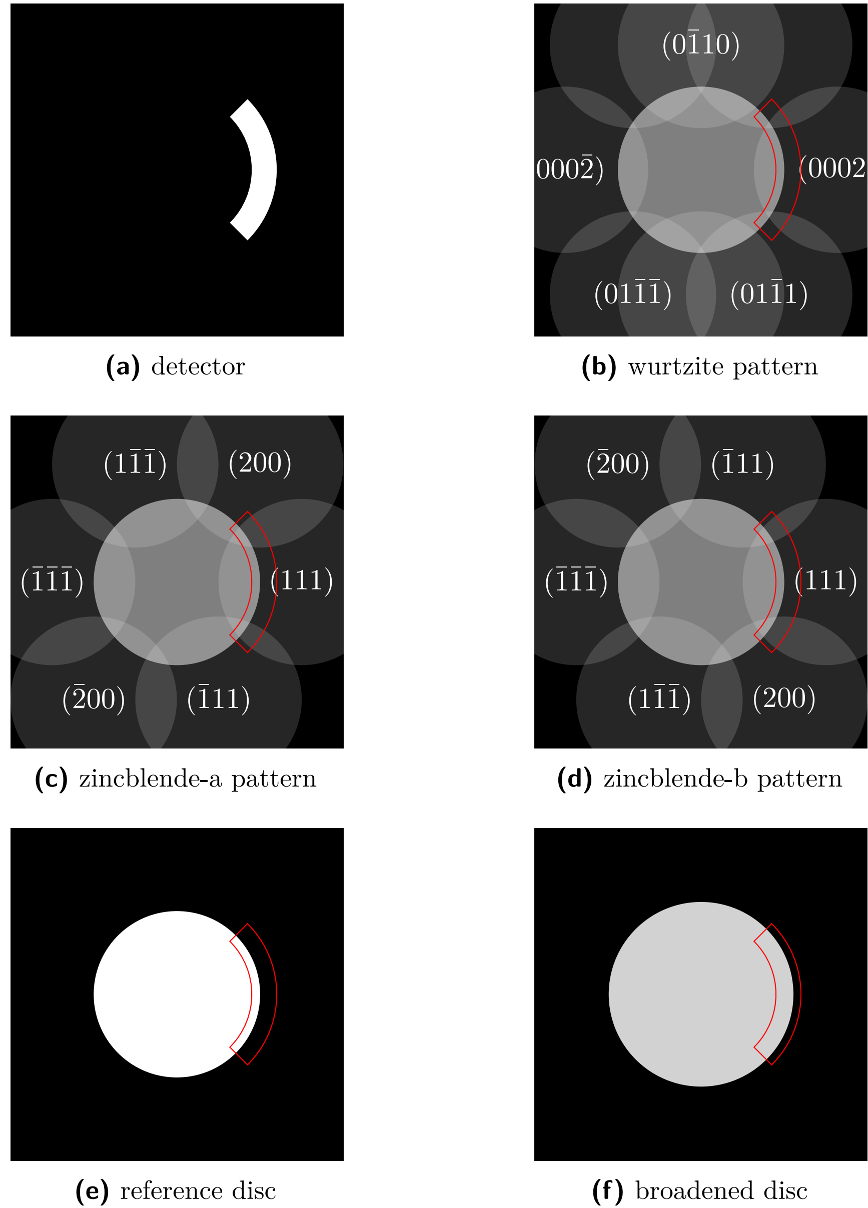

(a) detector **(b)** wurtzite pattern

(c) zincblende-a pattern **(d)** zincblende-b pattern

(e) reference disc **(f)** broadened disc

Figure 5.14: Datasets used for the simulation of the DPC signal: (a) single detector segment, (b) to (d) crystal structure patterns for wurtzite and the two twinned orientations of zincblende, as well as a reference (e) and a broadened (f) diffraction disc. To make them better visible in print the side discs of the crystal structure patterns have been increased in intensity compared to the actual simulation data. The detector area is indicated in (b) through (f) as red frame to give an idea of the spatial relationship.

at the spot positions of wurtzite (5.14b) and zincblende (5.14c and 5.14d). The two zincblende patterns represent the two twin orientations of zincblende which can be converted into each other by mirroring on the $(\bar{1}\bar{1}\bar{1})$–(111) axis and will be referred to as zincblende-a (short zba) and zincblende-b (zbb). The structural data of the patterns was taken from Williams and Carter [181]. In all three cases the brightness of the central disc is 50 % of the reference disc while the surrounding first order diffraction discs have 5 % brightness each. The brightness values are chosen arbitrarily as they are not thought to fully reproduce the complex dynamical diffraction pattern exemplarily shown in Figure 5.13, but they shall just reflect its basic symmetry and have a zero order beam that contains most of the intensity. Since the detector integrates over a fair angular and radial range, it appears reasonable to do this simplification and still keep the ability to draw conclusions about the general tendencies. Also summing up the intensities of the zero and first order discs does not yield a brightness of 100 % which can be justified by the fact that a small portion of the intensity would be contained in higher order diffracted beams that are not considered in the generated patterns as they are too far off the center to be recorded by the detector.

In the simulation two operations are performed on each of the images 5.14b to 5.14f: First the detector segment is rotated by angles φ_{rot} around the image center in 15° steps in a full circle and for each step the intensity of the respective pattern within the detector area is summed up. Afterwards the pattern is shifted by a small amount $\vec{k}_0 = 2.4\,\%$ of the reference disc radius in the direction of the (0001)/(111) axis, which corresponds to the direction in which the polarization fields within the crystal are expected. Transferred to the microscope used, where the radius of the diffraction disc corresponds to a $\vec{k}$ distribution with a convergence semiangle of 0.2 mrad to 3.5 mrad, this shift amount correlates to a deflection of some microradians which is comparable to the deflections typically occurring in real measurements.[212] The shift step is done three times up to a total shift of $3\vec{k}_0 = 7.2\,\%$ of the reference disc radius and for each shift value the detector rotation measurement is repeated on the shifted image.

The determined values plotted against the rotation angles are shown in Figure C.1 in Appendix C. Difference data is generated from these datasets by taking values from rotation angles $\varphi_{\text{rot}} \in \frac{360° \cdot n}{4} + \varphi_{\text{offset}}$, with $n \in \{1, 2, 3, 4\}$ and $\varphi_{\text{offset}} = [0°, 90°[$, and calculating the difference of those values which differ by 180°. The resulting $\Delta I_{3,9}$ and $\Delta I_{12,6}$ are then used to calculate for every rotation and shift state the displacement amplitude – corresponding to field strength in a real measurement – according to Equation (4.2) as well as the deflection angle $\varphi_{\text{rot,meas}} = \text{atan}\,(\Delta I_{12,6}/\Delta I_{3,9})$ with respect to the detector axes that the 'measurement' yields.

The intention behind the rotation is to check whether there is a geometrical influence in a way that a change in the angular relation of the crystal structure orientation with respect to the detector axes can change the measured field. This

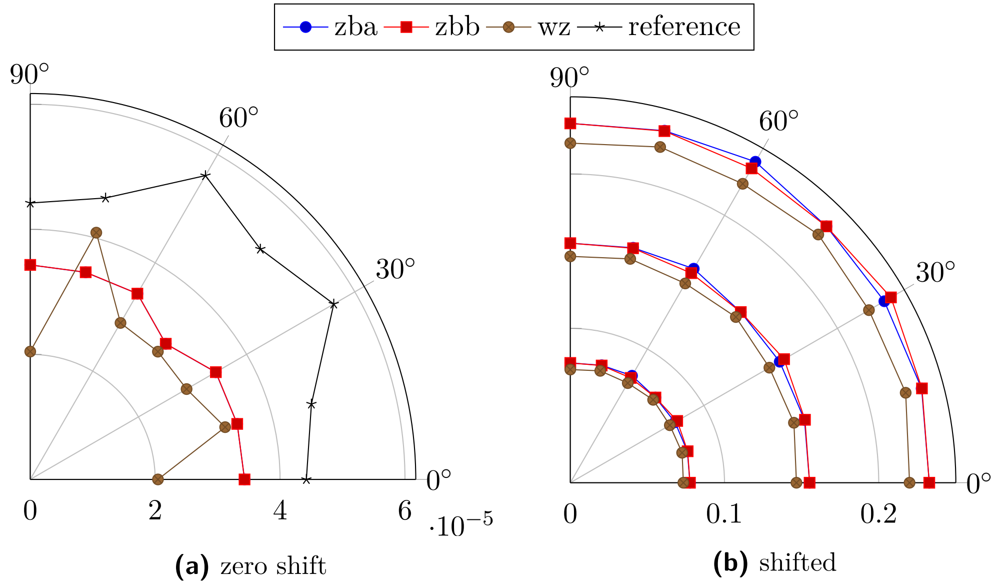

(a) zero shift **(b)** shifted

Figure 5.15: The measured beam deflection plotted against the rotation angle between detector and the intensity pattern in the detector plane for the three crystal structure patterns and the reference disc. Only the first quadrant is plotted since the values are periodic every 90°. (a) is the situation at zero shift while (b) shows the angular dependence of the measured deflection for the patterns shifted by $1\vec{k}_s$, $2\vec{k}_s$, and $3\vec{k}_s$ which appear as concentric rings. The curves belonging to one pattern are all drawn in the same colour with bigger radii corresponding to bigger shifts. In (b) the reference disc curve has been omitted. Note also the different scaling of the radial axes between the two plots.

is of relevance for two reasons: First, the nanowires are oriented randomly on the specimen grid and hence towards the detector axes and second, the electron optics between the specimen and the detector introduce an arbitrary rotation of the diffraction disc with respect to the specimen orientation (compare Section 4.1.2) – that means that both the orientation of the diffraction disc pattern as well as the direction of a diffraction disc shift can be oriented arbitrarily towards the detector axes. The shift part addresses the question if and how the field dependency itself behaves differently when the intensity profile in the detector plane is no longer a simple, step-function–like circular intensity profile.

5.2.2 Influence of crystal structure on the DPC signal

The first result of the simulation is the relationship of measured deflection and the angular orientation between crystal structure pattern and detector which is plotted

in Figure 5.15 for the non-shifted case (5.15a) and the three shifted cases (5.15b).

As can be seen in Figure 5.15a, the simulation seems to measure a deflection even if the respective diffraction disc pattern has not been shifted not only for the crystal structure patterns but also for the reference disc, which should not have any angular dependence at all since it is a simple circle. The seeming shift of the reference disc can be explained as an artefact of the simulation method: The used patterns (Figure 5.14) have been generated once as pixel graphics and were then rotated and shifted by the respective amounts using an image manipulation program. As the rotation of pixel graphics is not possible without interpolation for angles other than 90°, the rotation steps introduce a slight inaccuracy. With this argument the apparent deflection of the crystal structure patterns for zero shift can be attributed to that image manipulation artefact. Besides that it is especially notable that the zero shift curves for the twinned zincblende patterns are identical, which means that the DPC measurement should not produce a fake deflection signal between two segments of twinned zincblende that is in reality a result of the crystal structure symmetries.

Also in the case of the shifted patterns in Figure 5.15b, there is no significant angular dependence visible, since the plot curves for all three shifts are basically concentric rings for all three crystal structures. There is only a slight deviation between zincblende-a and zincblende-b for certain orientations (30° and 60°) which is in that case a result of the mirror symmetry of the two structures. It is however in the range of 2 % of the actual deflection and should therefore not make a significant influence in the measured field signals. The wurtzite structure does not show any surprising behaviour in those plots except that its deflection strength seems to be slightly weaker than that of the zincblende patterns, which will be discussed below.

In addition it has to be checked whether the interplay between the symmetries of the detector and the crystal structure could cause the DPC system to measure a shift into a direction that deviates from the actual shift direction. For this, the measured deflection angle $\varphi_{\text{rot,meas}} = \operatorname{atan}\left(\Delta I_{12,6}/\Delta I_{3,9}\right)$ has been determined from the simulation data and by taking $|\varphi_{\text{rot}} - \varphi_{\text{rot,meas}}|$, the deviation of the measured deflection direction from the actual one ($|\varphi_{\text{rot}}|$), it can be checked by how far they deviate. $|\varphi_{\text{rot}} - \varphi_{\text{rot,meas}}|$ is plotted against $|\varphi_{\text{rot}}|$ in Figure 5.16. As can be seen there, this deviation is in the order of 1°, i.e. the direction of the deflection is measured quite precisely even under the influence of a symmetric pattern within the diffraction disc.

Finally, it was already touched shortly that in Figure 5.15b the wurtzite plot exhibits slightly smaller measured deflections compared to the zincblende patterns although all of them have been shifted by the same spatial amount and hence should result in the same measured shift. To further investigate this, the measured deflections are plotted against the pattern shift distance for the three crystal structure patterns and the two simple discs of different intensity in Figure 5.17.

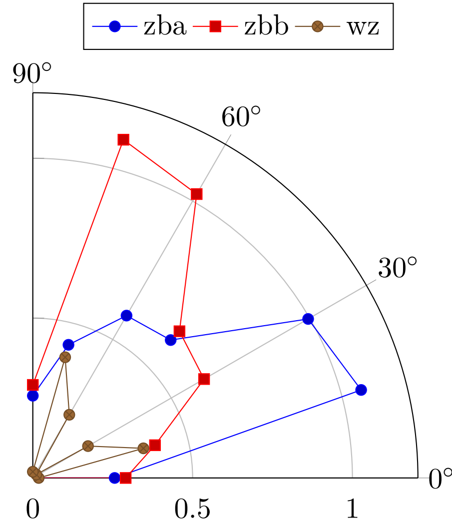

Figure 5.16: Plot of $|\varphi_{\text{rot}} - \varphi_{\text{rot,meas}}|$, the deviation of the measured rotation angle $\varphi_{\text{rot,meas}}$ from the factual angle φ_{rot} against φ_{rot}. Since the values are periodic in 90° only one quadrant is drawn.

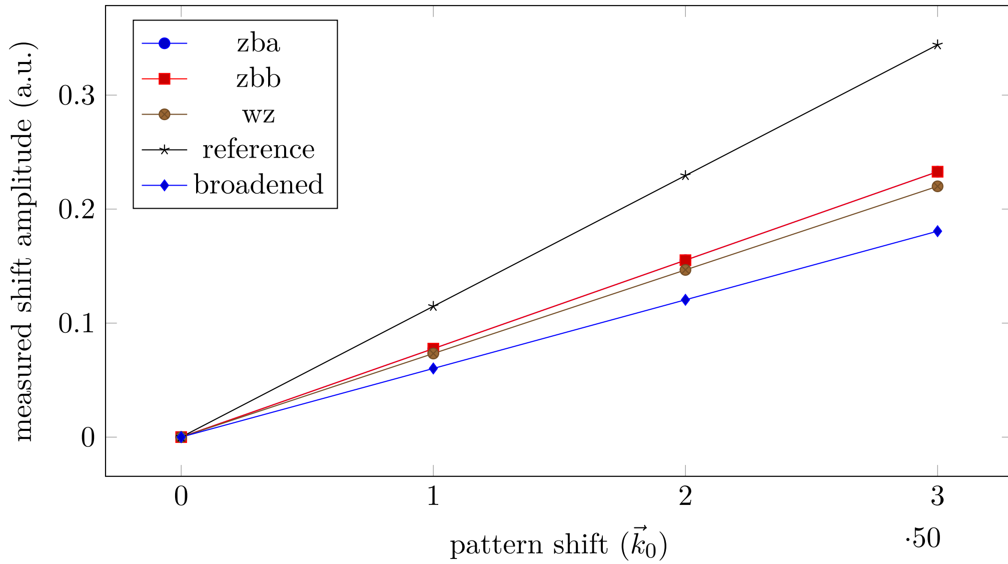

Figure 5.17: Deflection 'measured' from the simulation data for $\varphi_{\text{rot}} = 0$ plotted versus the amount of $\vec{k}_s$ the patterns were shifted. The zincblende-a curve is not visible since it is covered by the identical zincblende-b one.

Under the assumption that a quantitative measurement is not affected by variations of the diffraction disc as they should cancel out by the normalization with the sum signal I_{sum} in Equation (4.2), one would expect all curves to be identical since the same shift should always produce the same 'measured' shift. It is, however, immediately obvious that the different patterns produce considerably deviating deflection measurements for the same shift amount not only for variations of the crystal structure patterns but also and especially for the two simple discs. There, a change of 10 % in radius and 17 % in intensity results in a deviation in measured deflection by nearly 50 %. Such kind of irreproducibility basically puts quantitative DPC measurements into question as a whole.

5.2.3 An analytical approach to diffraction disc broadening

Since the simulation results were not able to shed light onto the question about the overly high measured fields but did reveal that also a simple change in diffraction disc radius has a considerable influence on the measured deflection, we will approach the problem analytically for the simple case of a circular diffraction disc.

For this purpose, we assume a diffraction disc that has an outer radius R_{d} and can be shifted within the polar $r\phi$ plane by the shift vector $\vec{k}_0 = (k_0, \vartheta)$, hence it has the form

$$r^2 = R_{\mathrm{d}}^2 + 2R_{\mathrm{d}}k_0\cos(\phi - \vartheta). \tag{5.6}$$

If the disc has a current density j_0 evenly distributed over a radius $R_{\mathrm{d},0}$ it carries a total intensity

$$I_0 = j_0 \int_0^{2\pi}\int_0^{r} r'dr'd\phi = j_0\pi R_{\mathrm{d},0}^2. \tag{5.7}$$

In addition we define a ring-shaped detector with an inner hole of radius $R_{\mathrm{h}} < R_{\mathrm{d}}$ and an outer radius large enough that the outer edge of the diffraction disc will always be within the detector. Then the illuminated area of a full ring detector is given by

$$I_{\mathrm{sum}} = j_0 \int_0^{2\pi}\int_{R_{\mathrm{h}}}^{r} r'dr'd\phi = j_0\pi\left(R_{\mathrm{d},0}^2 - R_{\mathrm{h}}^2\right) \tag{5.8}$$

as long as the shift amplitude $k_0 \leq R_{\mathrm{d}} - R_{\mathrm{h}}$. It is named I_{sum} since it is identical with the sum signal on the DPC detector as defined in Section 4.3.1 and Figure 4.4. If the current density j_0 scales with the radius of the disc R_d in a way that the total disc intensity I_0 stays constant, as it was the prerequisite for the two diffraction discs in the simulation described in Section 5.2.1, we can express the current density

$$j = \frac{I_0}{\pi R_{\mathrm{d}}^2} \tag{5.9}$$

as a function of the total intensity and the disc radius and hence rewrite I_{sum} as

$$I_{\mathrm{sum}} = I_0 \left(1 - \left(\frac{R_{\mathrm{h}}}{R_{\mathrm{d}}}\right)^2\right). \tag{5.10}$$

It is notable at that point that I_{sum} is *not* constant then if the disc radius scales according to Equation (5.9) but there is a non-linear, monotonously increasing redistribution of intensity onto the detector ring for increasing R_{d}.

For a segmented detector the integration from Equation (5.8) over ϕ is not carried out over the whole 2π range but for $\frac{2(n-1)-1}{4}\pi \leq \phi \leq \frac{2n-1}{4}\pi$ with $n \in \{1, 2, 3, 4\}$, yielding quadrants that each extend by ±45° around the positive and negative x_1 and x_2 axis of the detector ring as drawn in Figure 4.4d:

$$\begin{aligned} I_n &= \frac{j}{2} \int\limits_{\frac{2(n-1)-1}{4}\pi}^{\frac{2n-1}{4}\pi} R_{\mathrm{d}}^2 + 2R_{\mathrm{d}}k_0 \cos(\phi - \vartheta) - R_{\mathrm{h}}^2 d\phi = \\ &= \underbrace{\frac{j\pi}{4}\left(R_{\mathrm{d},0}^2 - R_{\mathrm{h}}^2\right)}_{=\frac{1}{4}I_{\mathrm{sum}}} + j\Big[R_{\mathrm{d}}k_0 \sin(\phi - \vartheta)\Big]_{\frac{2(n-1)-1}{4}\pi}^{\frac{2n-1}{4}\pi}. \end{aligned} \tag{5.11}$$

After fully working out the integration and remapping to the clock-face–like segment identifiers as they were defined in Section 4.3.1, the intensities on the single segments can be described as

$$\begin{aligned} I_{3,9} &= \frac{1}{4}I_{\mathrm{sum}} \pm \overbrace{jR_{\mathrm{d}}}^{=\frac{I_0}{\pi R_{\mathrm{d}}}} k_0 \cos\vartheta = \frac{1}{4}I_{\mathrm{sum}} \pm \frac{k_0 I_0}{\pi R_{\mathrm{d}}}\cos\vartheta \\ I_{12,6} &= \frac{1}{4}I_{\mathrm{sum}} \pm jR_{\mathrm{d}}k_0 \sin\vartheta = \frac{1}{4}I_{\mathrm{sum}} \pm \frac{k_0 I_0}{\pi R_{\mathrm{d}}}\sin\vartheta \end{aligned} \tag{5.12}$$

and the difference intensities as

$$\begin{aligned} \Delta I_{3,9} &= I_3 - I_9 = \frac{2k_0 I_0}{\pi R_{\mathrm{d}}}\cos\vartheta \\ \Delta I_{12,6} &= I_{12} - I_6 = \frac{2k_0 I_0}{\pi R_{\mathrm{d}}}\sin\vartheta. \end{aligned} \tag{5.13}$$

From Equation (5.13) it can easily be seen that the magnitude of the deflection signal vector is given by

$$|\vec{\Delta I}| = \sqrt{\Delta I_{3,9}{}^2 + \Delta I_{12,6}{}^2} = \frac{2k_0 I_0}{\pi R_{\mathrm{d}}} \tag{5.14}$$

which is – as expected – linear in k_0. Differentiating Equation (5.14) with respect to k_0 yields the proportionality factor between a certain measured deflection signal and the causative disc shift to be

$$\frac{d|\vec{\Delta I}|}{dk_0} = \frac{2I_0}{\pi R_\mathrm{d}}. \tag{5.15}$$

This means for a real measurement, where k_0 is to be determined, that the measured deflection strength $|\vec{\Delta I}|$ had to be multiplied with $\frac{\pi R_\mathrm{d}}{2I_0}$ to get k_0. For the real measurement in the electron microscope this proportionality factor can be calibrated by applying a defined deflection and measuring the resulting signal response.[198, 211, 212] However, the factor as derived in Equation (5.15) does depend on I_0 and R_d which are not necessarily the same for calibration process and the actual measurement.

Dependence of the calibration factor on the disc-detector overlap

The influence of a changing I_0 was also recognized by Lohr [198] and Schregle [211] and can – for a given set of microscope parameters for which the calibration was done – be either caused by a change in gun brightness, for example because of ageing, or absorption of intensity by the specimen. To compensate for that, they normalized both, the calibration and the real measurement, with their respective sum intensity, i.e. the intensity on the whole detector ring. Regarding the calibration measurement one gets a calibration factor

$$\kappa_k = \frac{\pi R_\mathrm{d,cal} I_\mathrm{sum,cal}}{2I_0} = \tag{5.16}$$

$$= \frac{\pi^2 R_\mathrm{d,cal} j_\mathrm{cal} \left(R_\mathrm{d,cal}^2 - R_\mathrm{h}^2\right)}{2\pi j_\mathrm{cal} R_\mathrm{d,cal}^2} = \tag{5.17}$$

$$= \frac{\pi \left(R_\mathrm{d,cal}^2 - R_\mathrm{h}^2\right)}{2R_\mathrm{d,cal}}. \tag{5.18}$$

This normalized calibration factor is now independent of any changes in intensity or current density, however, it does still depend on the disc radius – now in a more complicated manner – and in addition on the relation between the radii of the diffraction disc and the inner hole of the detector ring. The relation gets more clear when expressing the disc radius in terms of the inner radius of the detector ring $R_\mathrm{d} = \alpha R_\mathrm{h}$ with $\alpha > 1$

$$\kappa_k = \frac{\pi R_\mathrm{h}}{2} \frac{(\alpha_\mathrm{cal}^2 - 1)}{\alpha_\mathrm{cal}}. \tag{5.19}$$

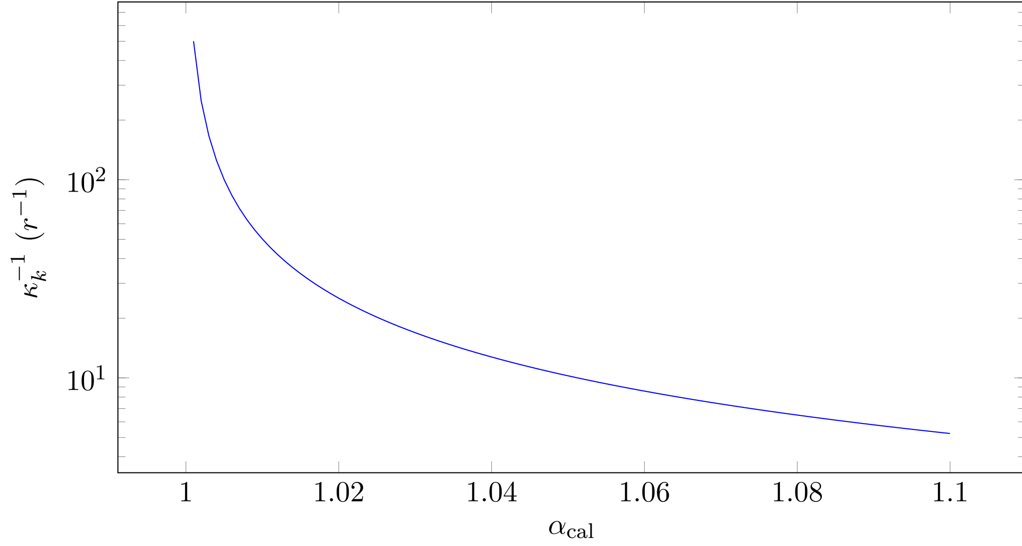

Figure 5.18: The detector response function κ_k^{-1} plotted against the dimensionless parameter α_{cal} which describes the ratio of the diffraction disc radius R_{d} and the inner rim radius R_{h} of the ring detector.

The inverse calibration factor κ_k^{-1} can be understood as the detector response function, i.e. how strong the signal measured by the detector varies for a specific shift $\vec{k}_0$ and is plotted in Figure 5.18. It is very strong for a small overlap between disc and detector where α is close to one and drops by nearly two orders of magnitude already for overlaps in the one-percent range. This tendency, which was confirmed experimentally by Schwarzhuber [212], means that there is an obvious trade-off between high sensitivity to measure already small disc shifts and a measurement range wide enough that the disc does stay on the detector even when maximally shifted.

Quantification under the influence of a changed diffraction disc radius

Performing a quantitative measurement with this setup means to determine the shift $k_{0,\mathrm{meas}}$ from a given difference signal vector $\vec{\Delta I}$ according to Equation (5.14) and sum signal I_{sum} using the calibration factor κ_k:

$$k_{0,\mathrm{meas}} = \kappa_k \cdot \frac{|\vec{\Delta I}|}{I_{\mathrm{sum,meas}}} = \kappa_k \cdot \frac{2I_0}{\pi R_{\mathrm{d,meas}} I_{\mathrm{sum,meas}}} k_0. \tag{5.20}$$

The $\frac{|\vec{\Delta I}|}{I_{\mathrm{sum,meas}}}$ part can be transformed in analogy to Equations (5.16) to (5.19), which results in

$$k_{0,\mathrm{meas}} = \overbrace{\frac{\pi R_{\mathrm{h}}}{2} \frac{(\alpha_{\mathrm{cal}}^2 - 1)}{\alpha_{\mathrm{cal}}}}^{=\kappa_k} \cdot \overbrace{\frac{2}{\pi R_{\mathrm{h}}} \frac{\alpha_{\mathrm{meas}}}{(\alpha_{\mathrm{meas}}^2 - 1)} k_0}^{=\frac{|\vec{\Delta I}|}{I_{\mathrm{sum,meas}}}} = \tag{5.21}$$

$$= \frac{(\alpha_{\mathrm{cal}}^2 - 1)\,\alpha_{\mathrm{meas}}}{\alpha_{\mathrm{cal}}(\alpha_{\mathrm{meas}}^2 - 1)} k_0. \tag{5.22}$$

It is immediately obvious that the left and right side of Equation (5.22) can only be equal if α_{meas} equals α_{cal}, which means that the diffraction disc must not change its radius between calibration and measurement. Such a change can either happen by using microscope settings that result in a different diffraction disc radius or by scattering that causes a broadening of the diffraction disc. The former can easily happen for example if the specimen is not at the same height with respect to the objective lens system, resulting in a different focal length and hence convergence angle of the electron probe which can be either larger or smaller compared to the calibration case. The latter happens through electron-specimen interaction as described in Section 4.2.3 and Figure 4.3b, but does in many cases cause only a negligible change in radius and a slight blurring of the disc edge, which is however not true for the nanowires considered in this work, as was shown in Figure 5.13.

Based on Equation (5.19) we can derive the ratio

$$\frac{k_{0,\mathrm{meas}}}{k_0} = \frac{(\alpha_{\mathrm{cal}}^2 - 1)\,\alpha_{\mathrm{meas}}}{\alpha_{\mathrm{cal}}(\alpha_{\mathrm{meas}}^2 - 1)} \tag{5.23}$$

that can be used as a quality factor of how the measured shift deviates from the actual shift and which is plotted against α_{meas} in Figure 5.19 for different values of α_{cal}. All plotted curves intersect with the horizontal line at $k_{0,\mathrm{meas}}/k_0 = 1$ where $\alpha_{\mathrm{meas}} = \alpha_{\mathrm{cal}}$, i.e. the ideal, deviation-free measurement condition is fulfilled. If $\alpha_{\mathrm{meas}} > \alpha_{\mathrm{cal}}$ and hence also the disc radius is has increased, then the measured shift is underestimated while it is overestimated for a decreased radius ($\alpha_{\mathrm{meas}} < \alpha_{\mathrm{cal}}$). An overestimation can basically be of arbitrary strength since the function diverges as α_{meas} approaches 1 where the overlap between disc and detector vanishes, while an underestimation can be expected to be less extreme over a wide range of α_{meas}. From that it can be derived that the dynamic diffraction induced broadening of the disc as shown in Figure 5.13 cannot be the main reason for the measured electric fields and polarizations in Sections 5.1.2 and 5.1.3 being too large, since the broadening would cause a reduction, not an increase of the measured fields.

Another reason for the high fields might be based on intensity fluctuations within the dynamic diffraction patterns that could be misinterpreted as too large fields if

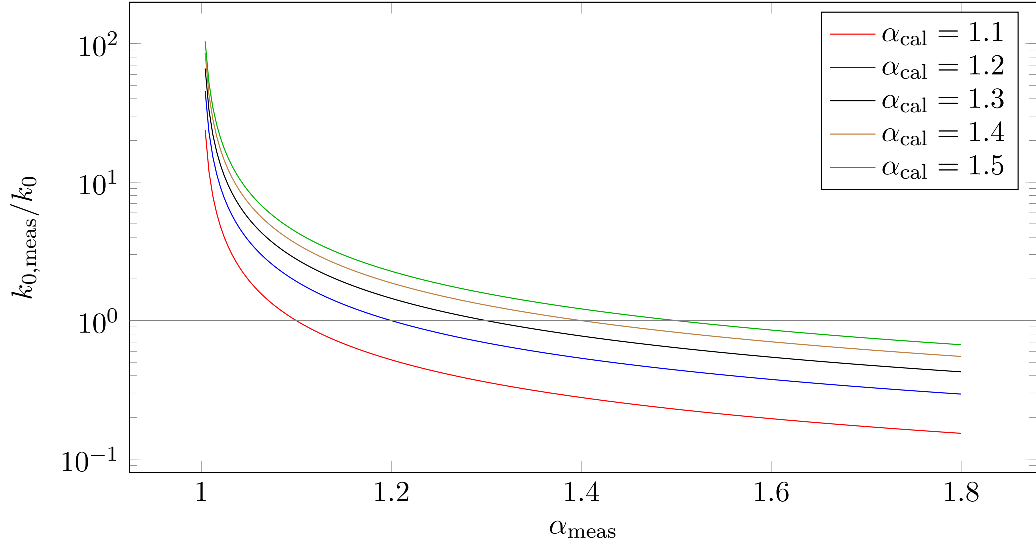

Figure 5.19: The quality factor $k_{0,\mathrm{meas}}/k_0$ plotted against the ratio of diffraction disc radius R_d and inner rim radius R_h of the ring detector at measurement time (α_{meas}) for different values of the same ratio at calibration time (α_{cal}). The horizontal line at $k_{0,\mathrm{meas}}/k_0 = 1$ denotes the ideal case where $\alpha_{\mathrm{meas}} = \alpha_{\mathrm{cal}}$.

their structure coincides unfavourably with the detector geometry. However, this question has to remain unresolved within this work since it goes beyond the simple model developed in this section.

5.2.4 Implications for quantitative DPC

The results presented above show the pitfalls involved with the usage of a segmented ring detector for quantitative DPC measurements. Those are by and large a result of the fact that the single detector segments do not provide any spatially resolved signal. Hence they can not discriminate in the first place between intensity changes due to a reduced overall intensity I_0 (cf. Equation (5.7)) and due to a change in the disc radius (Equations (5.8) and (5.10)) which changes the amount of intensity that is cut out of the signal through the inner hole. This means that quantitative measurements are extremely sensitive to small differences of the disc radius between the calibration and the actual measurements. To eliminate this, additionally recording the signal of the bright field detector would be useful, which is located within the DPC detector ring (see Figure 4.4) and therefore receives most of the intensity cut out by the ring detector hole. Recording the bright field signal for both, calibration and measurement, and comparing the ratios of signal that has been measured on the outer ring and on the bright field detector should give a good estimate of how the

diffraction disc radius has changed. This should provide a good fix for situations where the diffraction disc does still have a basically constant intensity profile with only slight broadening and blurring on the outer edge.

This would, however, not provide a fix for specimens what cause major distortions on the diffraction disc as the ones presented in Section 5.1 for which a simple ring detector setup does not provide suitable spatial resolution. Instead, detectors would be needed that are capable to image the intensity distribution within the detector plane spatially resolved as already proposed for other reasons in some publications.[197, 208, 210, 213] With such a detector a full image of the diffraction disc pattern in the detector plane would be recorded for every image pixel of the real space image. The diffraction disc pattern shift could then be determined for each image pixel using pattern recognition techniques as it was shown already for measurements on CBED patterns by Müller *et al.* [227, 228]. However, this is still a challenging task in terms of data recording, storing, and processing.

5.3 Summary

In this chapter a direct detection of spontaneous polarization in the wurtzite crystal phase of the non-Nitride III–V-semiconductors GaAs and GaP has been shown experimentally using differential phase contrast (DPC) microscopy. The findings are affirmed by simulations considering a possible interplay of the involved crystal symmetries and the DPC detector geometry. Above that a quantification of the spontaneous polarization has been tried which, however, yields results that are one to two orders of magnitude above the values given in the literature.

Motivated by the deviation of the quantitative values from the theoretical ones, the interplay of the electron beam and the four quadrant DPC detector has been modelled mathematically and it was possible to identify experimental limitations with respect to quantitative measurements that are inherent to this detector design. Based on these findings an approach is proposed to mitigate these limitations for measurements on specimens that comply to certain conditions. For specimens that do not fulfil these conditions – as the nanowires examined in this chapter – it turns out that they are not reliably accessible to quantitative DPC measurements with the detector setup used in this work.

6 Characterization of MnAs Nanocrystals

This chapter describes the characterization of nanowires where manganese (Mn) has been supplied during different stages of the MBE growth process of GaAs nanowires with the aim to achieve a material with ferromagnetic properties as shortly described in Section 6.1. Most of the characterization was done using energy dispersive X-ray spectroscopy (EDX) (cf. Section 4.3.2) with the goal to identify, where manganese can be found in the nanowires crystal and to find out which compound it forms there. Additionally high-resolution TEM and selective area (SA) electron diffraction (cf. Section 4.2.2) have been employed on some compounds.

The growth of these samples has been performed by Joachim Hubmann from the MBE group of Professor Bougeard at *Universität Regensburg* in close feedback with the characterizations partly presented here. The results from this chapter have been published in Nano Letters [229]. A more in-depth description of the growth process, the material systems of the magnetic semiconductors gallium manganese arsenide ((Ga,Mn)As) and manganese arsenide (MnAs) as well as further characterizations of the presented samples with other than TEM based methods can be found in the dissertation of Joachim Hubmann [230]. The general parameters used for the sample growth can be found in Appendix A.3 while in the following only parameters will be given that are directly necessary for the understanding of the presented data.

6.1 Motivation

Manganese-based semiconductors such as (Ga,Mn)As and MnAs play an important role in the field of spintronics where their properties allow to inject and detect spin polarized electrons in more 'conventional' semiconductors such as GaAs.[231, 232] MnAs is especially favourable here in terms of future spintronics devices since it has a Curie temperature above room temperature at 315 K [233] while the record Curie temperatures of (Ga,Mn)As are at 173 K [232] which imposes some limitation for computing devices built on (Ga,Mn)As-based structures. The combination of these materials with semiconductor nanowires with their natural, quasi–two-dimensional structure could provide access to spin phenomena in one dimensional structures.[234]

However, growing such structures is rather complicated since the growth of (Ga,Mn)As and MnAs takes place at temperatures around 250 °C which is significantly lower compared to the temperatures above 500 °C that are necessary in the *vapour-liquid-solid* growth as described in Section 2.1.3 and inhibits the direct controlled growth of such materials into the nanowire crystal.[56, 218, 222, 235, 236] Instead, growth processes have been developed where first a conventional III–V semiconductor core nanowire is grown in a standard growth procedure and subsequently grow a shell of either (Ga,Mn)As or MnAs is deposited around it in a growth process that uses more or less standard parameters for two-dimensional layer growth.[56, 218, 222, 235] A second option are methods where the III–V material is 'doped' with manganese at doping concentrations of several percent that leads to the precipitation of MnAs clusters within the otherwise undoped crystal [234] which is known also from two-dimensional (Ga,Mn)As layers grown at elevated temperatures [237, 238] or on the side facets of the nanowire [239, 240].

The samples presented here belong to a growth study that was aimed at the development of a growth procedure that yields MnAs-containing, MBE-grown GaAs nanowires similar to the results shown by Radovanovic *et al.* [234], Yatago *et al.* [239] and Hara *et al.* [240] which were using CVD techniques.

6.2 Characterization

In the following, three approaches will be shown that were performed in order to incorporate manganese into the GaAs crystal: the addition of manganese *during* the nanowire growth and *after* the growth had been stopped as well as growing with additional additional manganese and subsequent *growth termination under an arsenic atmosphere.*

6.2.1 Mn supply during and after growth

For the first case an approximately 300 nm long GaAs nanowire stub was grown before manganese was supplied in parallel to gallium and arsenic during the further growth process with the intention to accumulate manganese in concentrations high enough to force the precipitation of MnAs clusters. The growth was terminated in this case by just shutting down all three material sources which should have conserved – as far as this is possible under the drastically changed pressure and temperature between the growth chamber and ambient conditions – the catalyst droplet at the nanowire tip in the same state as during the growth process.

A bright-field STEM image of a nanowire from this sample is shown in Figure 6.1a, where two things are of interest: First, the catalyst droplet is not spherical as it is usually known from nanowires grown in the self-catalysed growth method (cf. Section 2.1.3), but has some edged shape, resembling a cube that was attached to

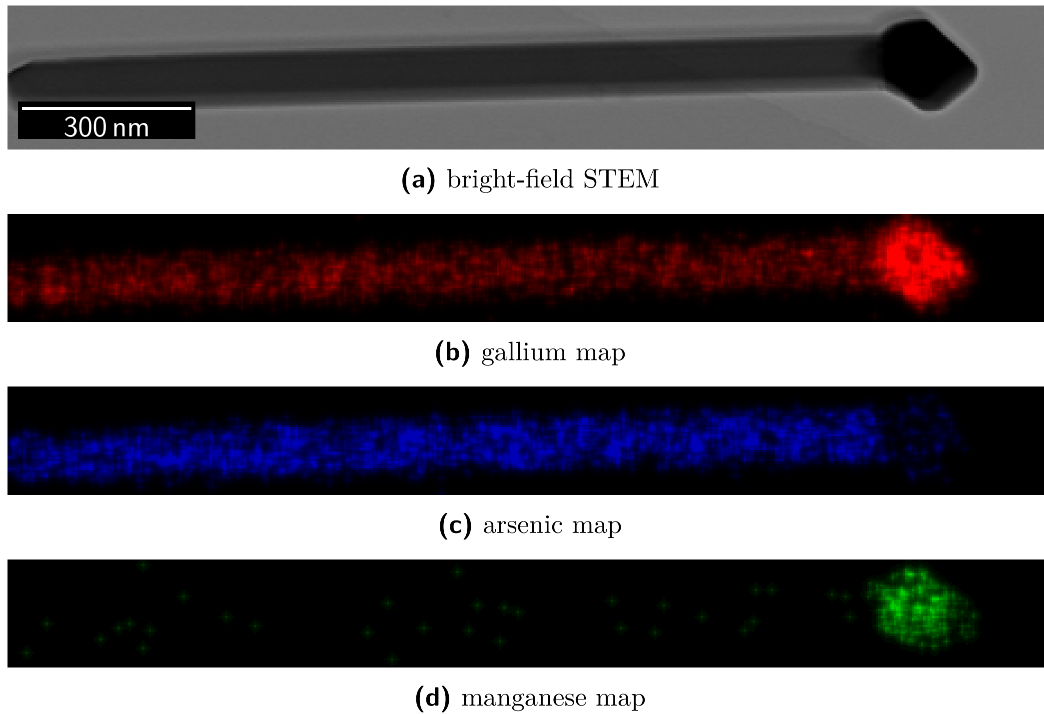

(a) bright-field STEM

(b) gallium map

(c) arsenic map

(d) manganese map

Figure 6.1: Compositional characterization of a nanowire where manganese was supplied additionally to gallium and arsenic during growth. The bright-field STEM image (a) shows the overall morphology with a somehow edged catalyst droplet. In the EDX maps of gallium (b), arsenic (c), and manganese (d) it can be seen that the droplet consists solely of gallium and manganese and that manganese is not found elsewhere in the nanowire crystal. Different brightnesses of the gallium and arsenic maps in the nanowire body are due to the fact that each image is normalized to the brightest image feature which is the droplet in case of gallium but the body in case of arsenic.

the nanowire top with one corner. The second, less obvious thing is, that there is no apparent transition visible where the additional manganese supply has started which one could expect since the manganese could possibly influence the thermodynamics of the catalyst droplet and its function in helping to incorporate material from the vapour phase into the crystal. However, this does apparently not happen, since also the length of the nanowire is comparable to such ones that have been grown under similar conditions without manganese addition. Above that, the nanowires do also not differ from such grown without manganese in terms of stacking fault occurrence.

Looking at the elemental maps Figures 6.1b to 6.1d one can see that manganese is only found in the catalyst droplet while it does not exceed noise level in the nanowire body. All three maps together show that the nanowire itself consists only of gallium and arsenic, while the droplet is gallium and manganese, but does not contain arsenic. This means that not only did the manganese not influence the nanowire growth, but that it also did not get incorporated into the nanowire crystal. Instead, it seems as if it just accumulated in the droplet and was carried up the nanowire during the growth process, ending up with a catalyst droplet that is some Mn-Ga compound.

Also, the shape of this particular droplet – it should be mentioned here that the droplet forms in this sample do show a rather wide variation where the nanowire shown here is on the one end of the range and droplets with a spherical outer shape are the other end – suggests that the compound has adopted some crystalline state. This can be backed by looking at the interface between the nanowire crystal and the droplet with conventional TEM, as shown in Figure 6.2. For the image Figure 6.2a the specimen was not oriented in a proper zone axis for high-resolution TEM imaging, bun nonetheless it was sufficiently oriented to image the periodicity of the GaAs crystal in the left image half, as can be seen from the fast Fourier transform in Figure 6.2b. Taking a fast Fourier transform also from the droplet side of the image (Figure 6.2c) reveals two faint spots (marked by white arrows) that give an hint on a periodic order in the droplet that has a totally different periodicity and orientation. This is not surprising since the Mn-Ga system is known to form crystalline structures of different Mn_xGa_y compositions.[241–243] Other nanowires with a spherical droplet do show such crystalline parts as well, which leads to the assumption that in this case the Mn-Ga compound did not fully crystallize but retained a liquid gallium or Mn-Ga droplet around the Mn_xGa_y crystal.

To check whether the manganese aggregation can only happen during the growth process, a second sample was grown with basically the same growth parameters but without the additional manganese during the growth. Instead, the manganese cell was opened after the growth itself was stopped and exposed the sample to manganese atmosphere for some time. This procedure yields basically the same results as the one described before, i.e. manganese is only found within the droplet which can either be fully or partially crystallized. The partial crystallization of

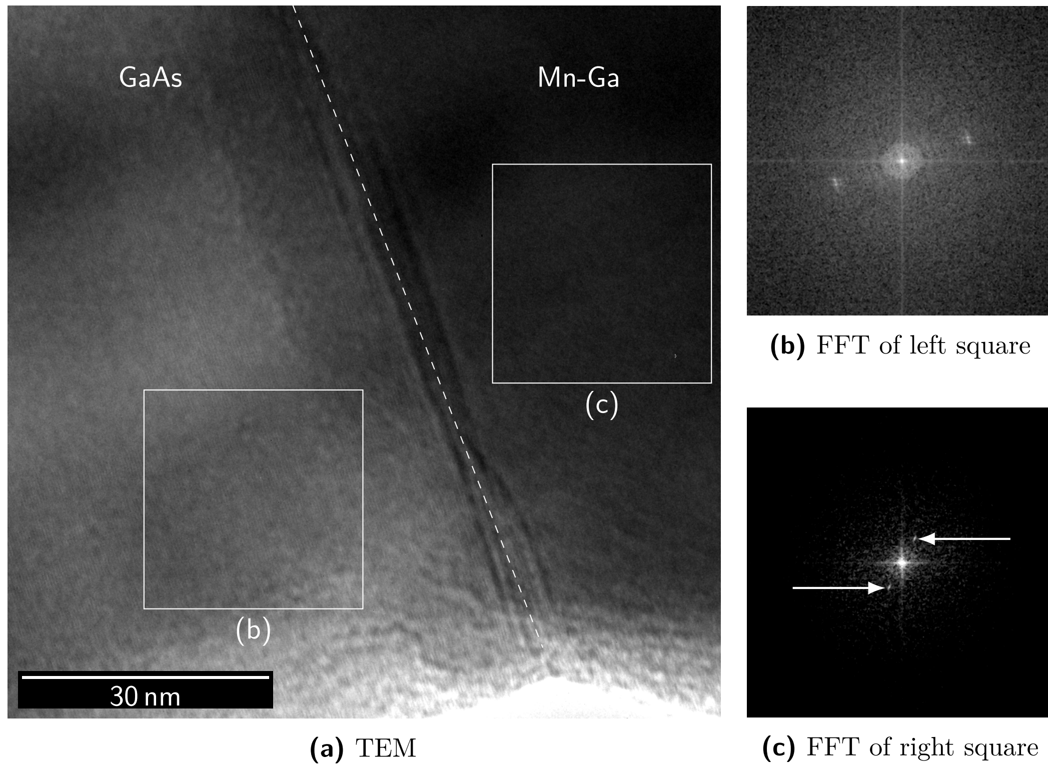

(a) TEM

(b) FFT of left square

(c) FFT of right square

Figure 6.2: TEM image of the interface between the nanowire crystal and the Mn-Ga droplet. The dashed line in (a) denotes the interface between the nanowire crystal at the left and the droplet on the right. Although the nanowire was not oriented into a zone axis suitable for high-resolution TEM imaging, the image does contain some periodic structures as can be seen from the fast Fourier transforms (b) and (c) (indicated with arrows since the reflexes are very weak), taken from the respective square frames in (a).

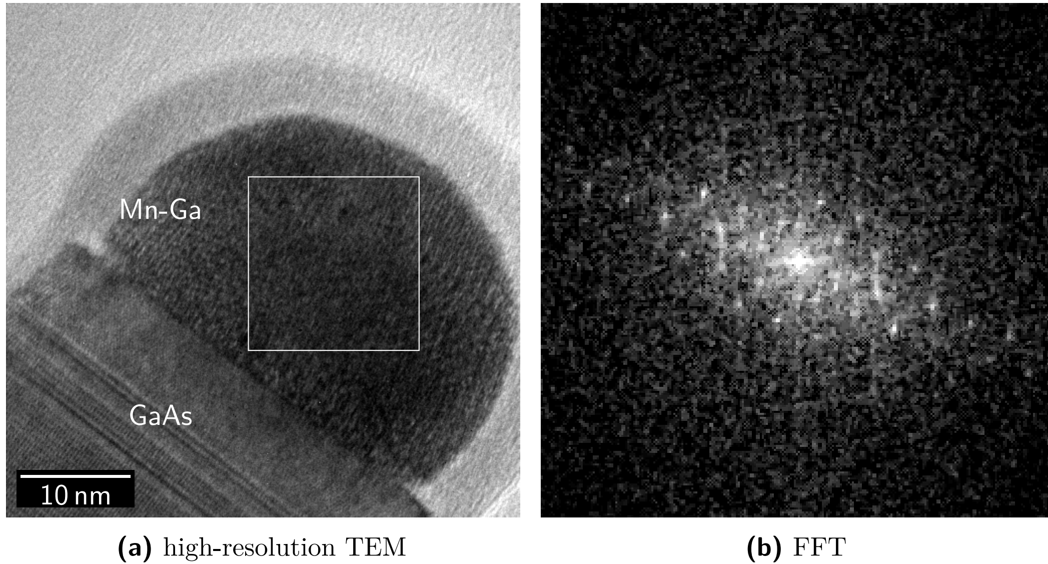

(a) high-resolution TEM **(b)** FFT

Figure 6.3: High-resolution TEM of the droplet of a nanowire where manganese was applied after the nanowire growth itself was finished. The droplet consists of an inner core consisting of a solidified Mn-Ga compound and an outer, presumably liquid, shell. The crystalline state of the core is verified in (b) by the fast Fourier transform taken from the white square in (a).

the droplet can be seen very clearly in Figure 6.3 where the crystallized core and the still liquid shell can clearly be told apart and the fast Fourier transform of the core shows a clear spot pattern as the signature of a crystalline object. In general it can be said here, that the morphological variations that occur among the nanowires of one of the two samples are larger than the variations between the samples.

Quantitative EDX would be needed to further investigate which Mn_xGa_y compound is formed exactly. However, those are inhibited or pointless for several reasons: The method developed by Cliff and Lorimer [244] which is typically used for the quantification of EDX measurements in the TEM does, among other things, depend strongly on the take-off angle of the measured X-ray radiation with respect to the specimen surface, which has to be known for a precise quantification. This is achievable quite precisely for specimens with planar surfaces but obviously not easily determined for a particle of arbitrary shape and would hence cause significant, not quantifiable error margins. Even if this issue could be solved or minimized then there was the problem that it cannot be determined for sure whether and by what amount the Mn_xGa_y was coated with some liquid gallium or Mn-Ga which would further impair a precise quantification of the elemental composition in the Mn_xGa_y crystal.

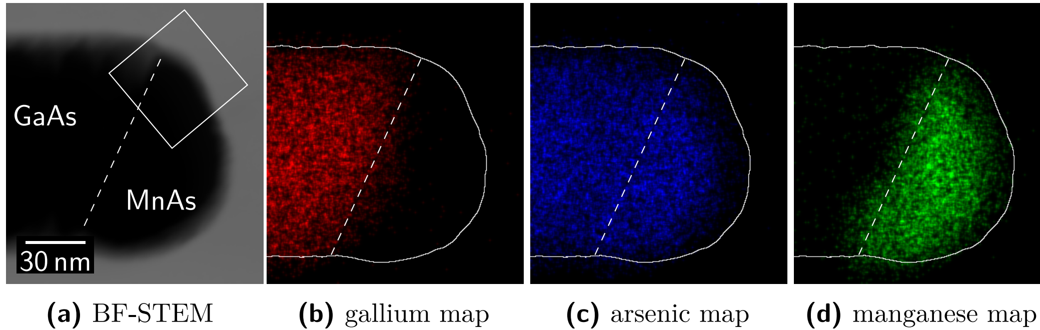

(a) BF-STEM **(b)** gallium map **(c)** arsenic map **(d)** manganese map

Figure 6.4: Bright-field-STEM image (a) and EDX maps (b) to (d) of a nanowire that was treated with the after-growth termination in arsenic atmosphere. The dashed white line in all four images indicates the interface between the crystal and the droplet. In the EDX maps the outline of the nanowire is drawn in white as a guide to the eye. The white square denotes the spot where the TEM image in Figure 6.5 was taken.

However, this is finally only a side aspect since the discovery of Mn_xGa_y does not add a solution to the search for the incorporation of manganese into the GaAs crystal.

Instead, it can be concluded from the results of these two samples that manganese does neither solve in the GaAs crystal nor deposit on the nanowire sidewalls in significant amounts as long as there is a liquid gallium droplet available to solve in, as was also already seen by Gas *et al.* [236]. Above that, the solved manganese seems to not influence the GaAs nanowire growth at least for manganese concentrations up to 10 % and possibly even beyond.[230]

6.2.2 Growth termination under arsenic atmosphere

The finding that manganese does not solve in the GaAs crystal with a liquid gallium phase present ultimately guides the way towards how to achieve the growth of (Ga,Mn)As or MnAs segments. It is known that the gallium droplet can be fully consumed if the sample is kept long enough in the growth reactor under an arsenic atmosphere until all the gallium has been bound by arsenic and included into the crystal.[56, 222, 245] Doing the same with a droplet that contains some amount of manganese should either at some point force the manganese to be included into the GaAs crystal matrix forming (Ga,Mn)As or, if the droplet is fully depleted of gallium, the manganese should remain which then could form MnAs together with the arsenic from the vapour phase.

As can be seen from the EDX elemental maps in Figure 6.4 this did basically work as intended: At the nanowire tip gallium can only be detected below the interface between the nanowire body and the droplet while manganese is only found

in the droplet, but not in the body. Arsenic is found in both parts and the fact that the arsenic map does not change its brightness at the interface between body and droplet already does suggest that its concentration did not change. In fact, it looks like the gallium has just been replaced with manganese at the interface, which lets suspect that arsenic is contained in both compounds in the same stoichiometric concentration. This is a first indication that the particle on the nanowire top could be MnAs which has the same stoichiometry as GaAs just with gallium replaced by manganese. Unfortunately, this argument has to stay hand-waving, since a quantitative EDX measurement to confirm the atomic composition is unfortunately prevented by the same factors that were already presented in Section 6.2.1.

Looking at the nanowire tip with high-resolution TEM reveals the crystalline nature of the MnAs particle. In Figure 6.5 it can be seen that the MnAs part exhibits a regular stripe pattern comparable to the one of the wurtzite GaAs that is visible in the top left corner of the image. The fact, that the (0001) lattice planes along both, MnAs and GaAs could be imaged at the same time means that both crystals share a common basal plane and are possibly even the same crystal orientation. The latter can be expected since MnAs is known to grow in wurtzite crystal structure with its (0001) plane on the (111)B surface of GaAs.[246–250]

In two-dimensional layer growth, the lattice mismatch in the a-direction of about $-6.6\,\%$ of MnAs compared to GaAs ($a_{\mathrm{MnAs}} = 0.3725\,\mathrm{nm}$ [251], $a_{\mathrm{hex,GaAs}} = 0.3988\,\mathrm{nm}$) leads to strongly disturbed layers when MnAs is grown on GaAs, which should not be expected in the case of nanowires since these do not suffer from lattice mismatch in the same amount as layer growth does.[83] The dislocations that appear in the lower left corner of Figure 6.5 are therefore at first surprising. However, since the interface between GaAs and MnAs is obviously not along a single (0001) plane but tilted towards the nanowire axis as can be seen in Figure 6.4, also the lattice mismatch in c-direction comes into play, which is $-13\,\%$ ($c_{\mathrm{MnAs}} = 0.5713\,\mathrm{nm}$ [251] compared to $c_{\mathrm{GaAs}} = 0.656\,\mathrm{nm}$) and could force the MnAs crystal to relief strain by introducing dislocations. It should, however, be said that this is not necessarily true for the nanocrystals on all nanowires of that sample, since the spectrum of their morphologies spans from a more or less half-spherical shape as shown here to about 20 nm thick discs on the nanowire top. Accordingly, also their contact interface to the GaAs crystal and hence their lattice adaptation varies among the morphological cases.

As a final check for the orientation of both crystals towards each other, selective-area electron diffraction of a MnAs crystal and the topmost part of the GaAs nanowire have been performed, which is depicted in Figure 6.6. The resulting diffraction pattern is confusing at first glance since it contains contributions of the wurtzite diffraction patterns of the wurtzite MnAs and both, the wurtzite and zincblende phase of GaAs. For clarity the important spots, i.e. the (0002), $(0\bar{1}10)$ and $(2\bar{1}10)$ spots of the wurtzite patterns are labelled in white for clarification.

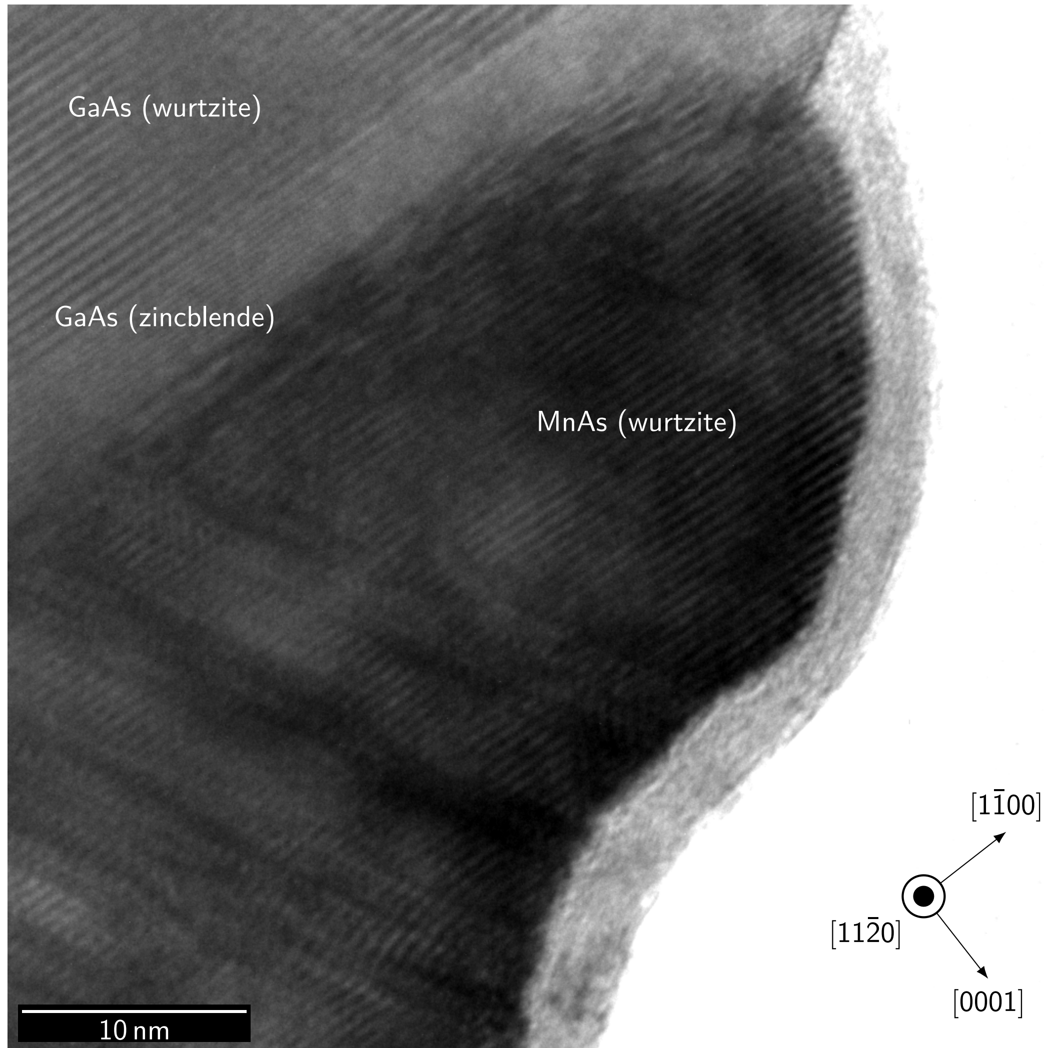

Figure 6.5: High-resolution TEM micrograph of the crystalline MnAs droplet taken at the spot indicated in Figure 6.4a from a nanowire that was grown in with growth termination under arsenic atmosphere. The growth direction is from top left to bottom right where the GaAs crystal terminates with a wurtzite segment and a small zincblende segment that is then topped by the wurtzite MnAs crystal, which has several dislocation lines in the lower left part of the image. The approximately 2 nm wide grey seam around the MnAs crystal is a remnant gallium or Mn-Ga compound that did not crystallize either because the arsenic treatment after the growth was not maintained long enough or because the compound reached a critical concentration that inhibits further growth.

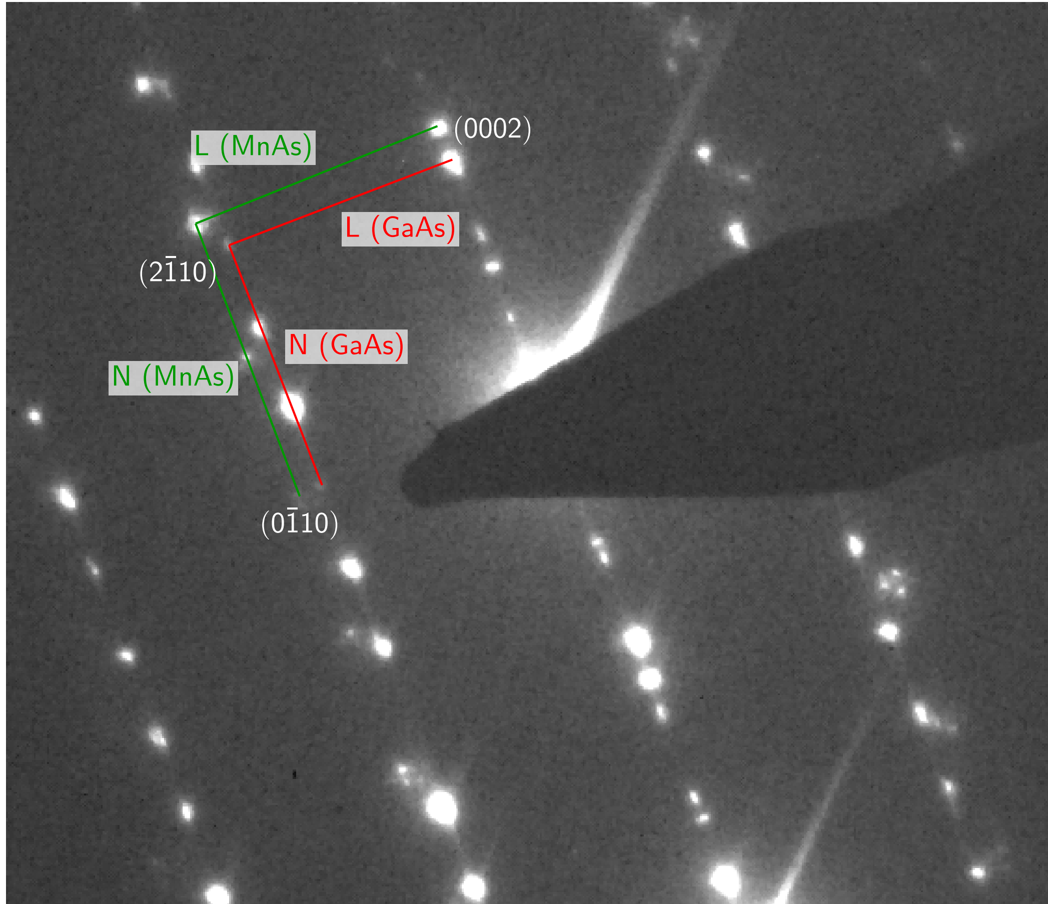

Figure 6.6: Selective-area diffraction pattern of the topmost part of a nanowire with the MnAs crystal on top. To be able to record this pattern, the zero order beam is blocked by a beam stop, visible as triangular dark structure that enters the image from the top right edge and protrudes to the image center. The diffraction pattern is a superposition of the different diffraction patterns involved, i.e. those of zincblende and wurtzite GaAs as well as wurtzite MnAs. The red and green annotations indicate for wurtzite GaAs and wurtzite MnAs, respectively, the reciprocal lattice plane spacings in (0002) (labelled 'N') and (0$\bar{1}$10) direction ('L').

These labelled spots are appearing twice in close vicinity, where the ones closer to the blanked zero order spot belong to the GaAs crystal lattice and the ones further apart to the MnAs lattice with its smaller lattice and hence wider spot separation in reciprocal space. From this it can be concluded that both crystal lattices are oriented in parallel, i.e. $(0002)_{\mathrm{GaAs}} \parallel (0002)_{\mathrm{MnAs}}$ and $(0\bar{1}10)_{\mathrm{GaAs}} \parallel (0\bar{1}10)_{\mathrm{MnAs}}$.

The lines annotated ‘N’ and ‘L’ indicate the spot separation in the (0002) and $(0\bar{1}10)$ direction, respectively, for GaAs in red and MnAs in green (see Williams and Carter [181] for further details on the labels and their meaning). Using the separations of the GaAs reflexes, which belong to known lattice constants, as a reference, it is possible to calculate the MnAs lattice constants as

$$\begin{aligned} a_{\mathrm{MnAs}} &= \frac{L_{\mathrm{GaAs}}}{L_{\mathrm{MnAs}}} a_{\mathrm{hex,GaAs}} = (0.88 \pm 0.08) \cdot 0.3988\,\mathrm{nm} = (0.35 \pm 0.03)\,\mathrm{nm} \\ c_{\mathrm{MnAs}} &= \frac{N_{\mathrm{GaAs}}}{N_{\mathrm{MnAs}}} c_{\mathrm{GaAs}} = (0.90 \pm 0.09) \cdot 0.656\,\mathrm{nm} = (0.59 \pm 0.06)\,\mathrm{nm} \end{aligned} \tag{6.1}$$

which is in good agreement with the values published by Tanaka *et al.* [251].

In conclusion, all measurements presented in this section support the assumption that the particles on the nanowire top are MnAs nanocrystals. Further evidence has been provided by SQUID measurements performed by Helmut Körner at the magnetism group of Professor Back (*Universität Regensburg*) which show that the sample is ferromagnetic up to the typical MnAs Curie temperature of 313 K.[230]

6.3 Summary

In this chapter the characterization of manganese-containing GaAs nanowires accompanying over several iterations the development of a growth process to grow MnAs nanocrystals on the tip of GaAs nanowires has been documented. The MnAs nanocrystals that were finally achieved have been characterized using energy dispersive X-ray spectroscopy, high-resolution TEM and selective-area electron diffraction, which did show that they are pure MnAs and grow in wurtzite structure epitaxially related to the underlying GaAs nanowire crystal.

The dissertation of Joachim Hubmann [230] describes further characterizations done on these nanocrystals using magnetic force microscopy (MFM) and SQUID. These reveal that the crystals contain only one single magnetic domain and are ferromagnetic up to the MnAs Curie temperature. Above that, the growth process was further extended to grow nanowires that have multiple isolated MnAs nanocrystals on their side facets.

7 Conclusion and Outlook

Within this thesis transmission electron microscopy has been used to characterize properties of GaAs and GaP nanowires as well as MnAs nanocrystals grown on top of GaAs nanowires.

The main part of this work contains the first direct experimental detection of the spontaneous polarization in the wurtzite phase of GaAs and GaP nanowires using differential phase contrast (DPC) microscopy. With this technique it was possible to visualize the charge sheets that are generated within the wurtzite phase of the two semiconductor materials as well as their absence in the zincblende phase. The additional attempt to quantify the electric fields present within the specimen and with this also the spontaneous polarization did, however, for both materials yield results which are far enough from the values found in the literature that they appear implausible.

Based on these findings, several aspects of the signal generation in the DPC system have been analysed and their impact on quantitative DPC measurements have been discussed. The simulation and analytical model that were employed for this task were able to confirm, that the signals measured in DPC are caused by a beam deflection within the specimen and not due to an unfavourable interplay of the crystal symmetry and the detector geometry. On the other side the analysis also brought to light several limitations to quantitative DPC measurements which are caused by the four-quadrant detector design used in this work. To avoid those issues experimental conditions have been formulated under which a meaningful quantitative DPC measurement is prevented at all and for those conditions where a quantitative measurement seems still applicable, measures have been proposed to mitigate the issues experienced in this work.

The second part of the experimental work was the characterization of GaAs nanowires where manganese was added using different process schemes with the aim to grow ferromagnetic (Ga,Mn)As or MnAs. The characterization was performed in close cooperation with the MBE group, providing direct feedback for subsequent growth runs. In this study it was possible to clarify how the incorporation of manganese into the GaAs crystal takes place under the presence of liquid gallium. This did finally lead to the development of a growth process that allows to grow ferromagnetic MnAs nanocrystals onto the top of GaAs nanowires, which was evidenced using several characteristic properties.

There are of course also points that had to remain open or lead the way to

further research activities: Since it was not possible to quantify the spontaneous polarization, this is yet to be done and considering the results achieved in this work, realization of this task might at least require a deeper understanding of quantitative DPC measurements. Above that it may need the development of new DPC detector systems that are capable of recording the diffraction disc with sufficient resolution to cope with specimens that cause significant intensity redistributions within the diffraction disc. Activities are already going on in that direction at the electron microscopy group of Professor Zweck. The research work on the nanowires with MnAs nanocrystals is only at the beginning since, now that they are available and can be grown in a controlled way, the electric and magnetic characterization of such nanowires can begin, working towards the creation of nanowire-based spintronic devices. However, those tasks go far beyond the scope of the work at hand and are left for future scientists to build on the results of this thesis and related works.

Appendix

A Growth Parameters

A.1 MBE-grown pure GaAs Nanowires

The data presented for GaAs nanowires in the polarization measurements was taken from a GaAs nanowire sample that was grown by solid source MBE with gold as a catalyst in the so-called 'pseudo-Ga catalyzed growth mode' as described by Soda *et al.* [57] (see also [222]) on a GaAs (111)B substrate covered with a 0.5 Å gold layer. The growth took place at a substrate temperature of 528 °C with a gallium growth rate of 2.8 $\frac{\text{Å}}{\text{s}}$ and an As_4 beam equivalent pressure of $3.2 \cdot 10^{-6}$ Torr. This results in nanowires that are pure zincblende with occasional stacking faults (distances between some 10 nm and several 100 nm) in their main body. The foot and body regions show a more disturbed picture, which can be attributed to unstable growth conditions in the early and the termination stage of the growth process that lead to a change in crystal phase.[57] Especially in the case of growth termination this results in a segment of some hundred nanometres wurtzite which was used in Section 5.1.2 to image the spontaneous polarization.[217]

A.2 MOVPE-grown GaP Nanowires

The GaP nanowires have been grown in a low-pressure, close-coupled showerhead (CCS) MOVPE reactor using a growth process as described in the supplementary information of [151]. With this process it is possible to grow stacking-fault free wurtzite nanowires of several microns length as well as zincblende segments of up to 12 nm. The growth of longer zincblende segments is also possible, however, then randomly distributed stacking faults and finally an uncorrelated mixture of both crystal phases occur.[151, 252]

The (111)B substrate is pre-patterned via nanoimprint lithography prior to growth with gold patches of 100 nm diameter and 500 nm pitch. On this substrate the initial stage of the growth is done with parameters for wurtzite growth (cf. Table A.1) at 750 °C with a low V/III ratio of 23 and additional supply of HCl which inhibits lateral growth. To grow zincblende segments into the nanowire, first the gallium supply as well as the additional HCl are switched off and the temperature lowered to 600 °C and the growth is continued for up to 3 s at a high V/III ratio of 452

Table A.1: Growth parameters used in the MOVPE growth of GaP nanowires to achieve wurtzite and zincblende crystal structure. The flow rates χ of the precursor gases trimethylgallium (TMG), PH_3 and HCl are given as dimensionless molar fraction of the total gas flow into the growth reactor.[151, 252]

Crystal Phase	t_{growth} °C	$t_{\text{substrate}}$ °C	χ_{TMG}	χ_{PH_3}	III/V	χ_{HCl}
Wurtzite	750	314 ± 4	$7.4 \cdot 10^{-5}$	$1.7 \cdot 10^{-3}$	23	$1.2 \cdot 10^{-4}$
Zincblende	600	491 ± 3	$4.0 \cdot 10^{-5}$	$1.8 \cdot 10^{-2}$	452	—

to form a zincblende segment. After that the gallium supply is stopped and the parameters are set back to wurtzite conditions. This sequence is repeated several times to create an alternating arrangement of wurtzite and zincblende segments.[151, 252]

A.3 MBE-Grown GaAs Nanowires with additional Mn

All samples presented in Chapter 6 have been grown in the self-catalysed growth method (cf. Section 2.1.3) on (111) oriented silicon substrate wafers with a thin native SiO_2 oxide layer. The growth temperature was set to 600 °C throughout all three samples and the gallium growth rates have been varied between $0.15\,\frac{\text{Å}}{\text{s}}$ and $0.4\,\frac{\text{Å}}{\text{s}}$ in order to achieve manganese doping concentrations in the order of 5 % to 16 % at a manganese growth rate of $0.04\,\frac{\text{Å}}{\text{s}}$. The beam equivalent pressure of As_4 was set to have an As_4/Ga ratio of 1.3 to 1.5. Since the exact way of how manganese was applied to the sample differs between the individual samples, this part is described on occurrence in Chapter 6.

B Field Determination Data

B.1 Experimental parameters

Table B.1: Measurement and specimen parameters used for the DPC measurements and field quantifications on GaAs and GaP nanowires. The figures given for 'gun lens', 'spot size' and 'C2 aperture' are labels that were assigned to those parameters by the microscope manufacturer. They are printed in quotes since – except for the C2 aperture diameter – their absolute quantities are not known but they are relevant for the reproducibility of the measurements.

Parameter		GaAs	GaP
acceleration voltage	kV	300	
gun lens	a.u.	'3'	
spot size	a.u.	'9'	
C2 aperture	a.u.	'3'	'2'
C2 lens (intensity)	%	37.993	37.386
objective lens	%	96.916	96.219
probe convergence semi-angle θ	mrad	1.5	0.5
camera length L	m	0.380	1.51
calibration factor κ	$\frac{\mathrm{V\,m}}{\mathrm{m}}$	1100	935
specimen thickness t	nm	111 ± 5	110 ± 10

B.2 GaP Raw Data

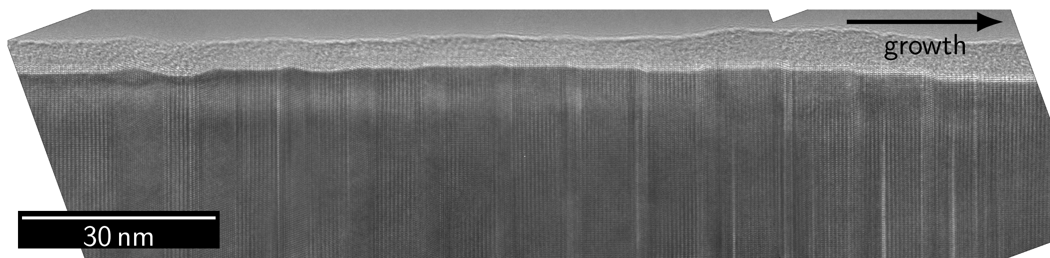

Figure B.1: High-resolution TEM overview over the segmented area of the GaP nanowire.

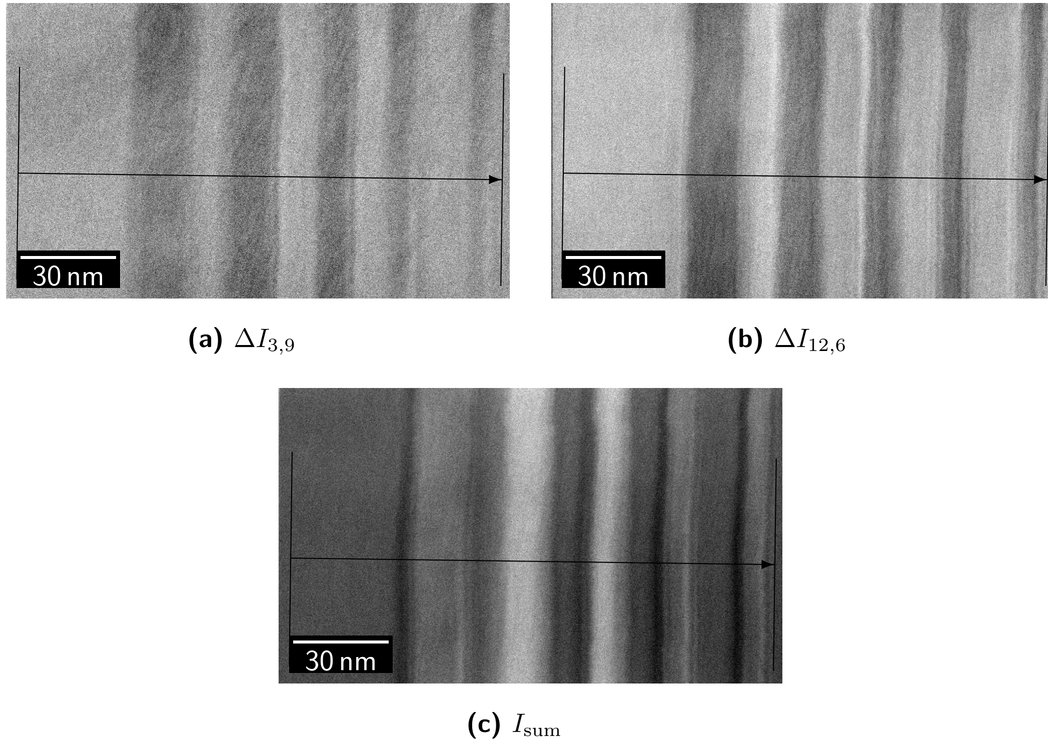

(a) $\Delta I_{3,9}$

(b) $\Delta I_{12,6}$

(c) I_{sum}

Figure B.2: Raw difference ((a) and (b)) and sum intensity (c) data images of the double multi-segment structure in GaP. The arrows in the images denote the line and averaging width – indicated by the vertical bars at both ends – where the intensity profiles in Figure B.3 were taken from.

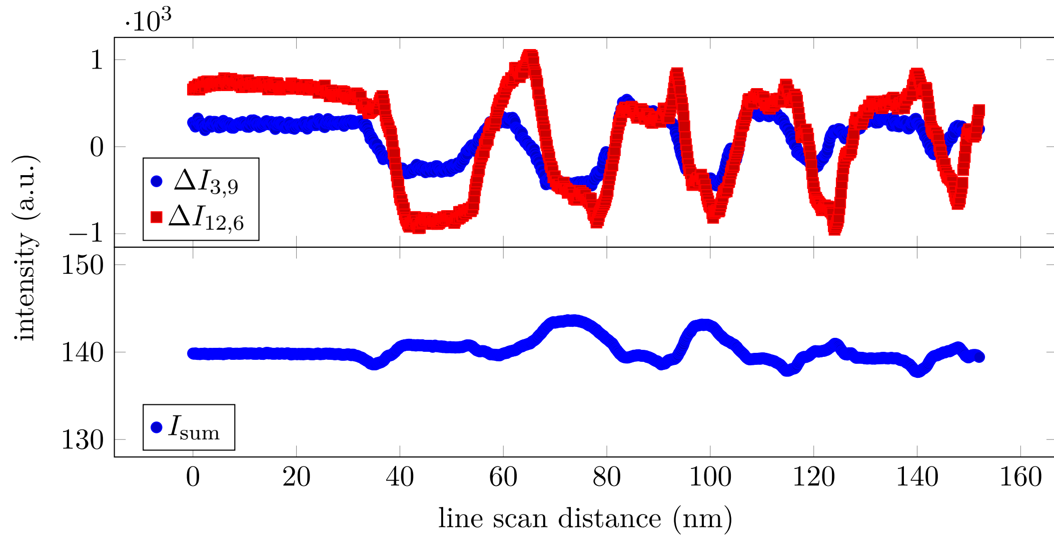

Figure B.3: Plots of the intensity profiles taken from the raw data images in Figure B.2.

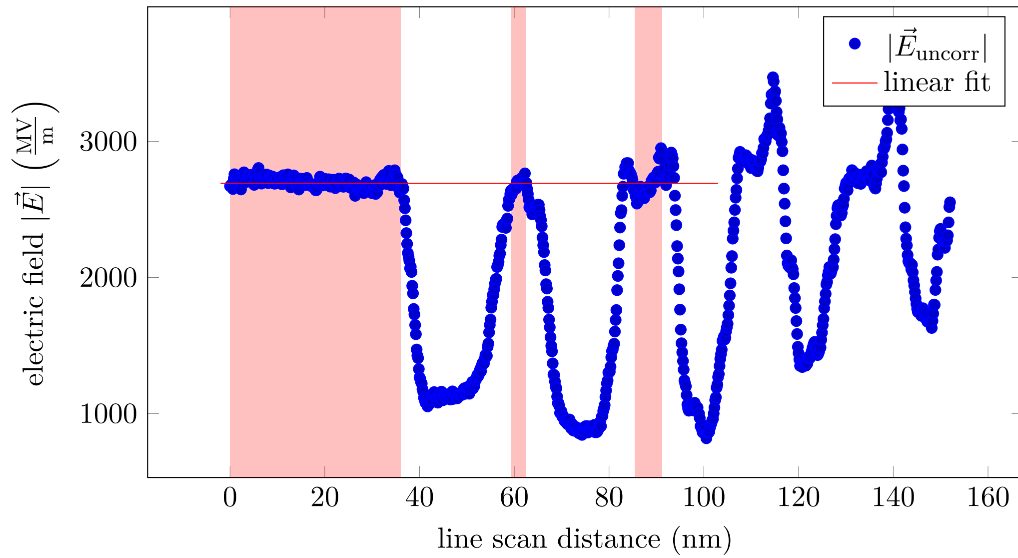

Figure B.4: Uncorrected electric field plot of the GaP nanowire. The data range where the linear fit was taken from are highlighted with red background.

C Simulation Data

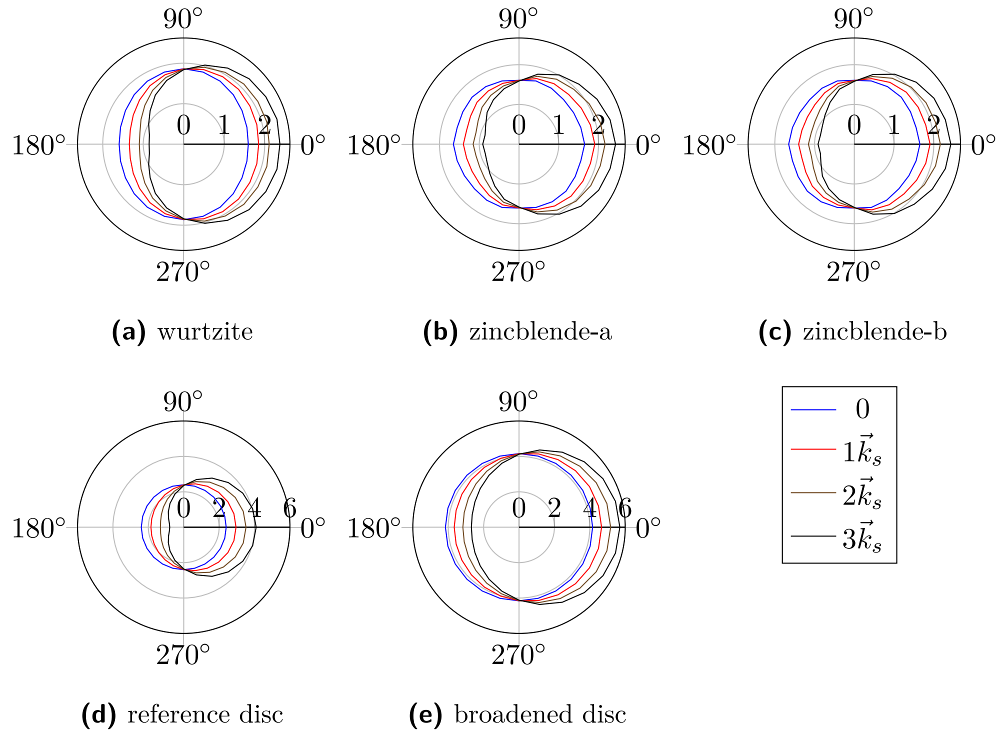

Figure C.1: Simulated intensity on a single detector segment as shown in Figure 5.14 plotted against the angle between the detector and the respective diffraction disc pattern for the different shift vectors. Note that the radial scale of the crystal patterns (a) to (c) is different from the simple discs (d) and (e).

Bibliography

[1] Y. Wu, Y. Cui, L. Huynh, C. J. Barrelet, D. C. Bell and C. M. Lieber. 'Controlled Growth and Structures of Molecular-Scale Silicon Nanowires'. In: *Nano Letters* 4.3 (2004), pp. 433–436. DOI: 10.1021/nl035162i.

[2] N. P. Dasgupta, J. Sun, C. Liu, S. Brittman, S. C. Andrews, J. Lim, H. Gao, R. Yan and P. Yang. '25th Anniversary Article: Semiconductor Nanowires – Synthesis, Characterization, and Applications'. In: *Advanced Materials* 26.14 (2014), pp. 2137–2184. DOI: 10.1002/adma.201305929.

[3] Y. Xia, P. Yang, Y. Sun, Y. Wu, B. Mayers, B. Gates, Y. Yin, F. Kim and H. Yan. 'One-Dimensional Nanostructures: Synthesis, Characterization, and Applications'. In: *Advanced Materials* 15.5 (2003), pp. 353–389. DOI: 10.1002/adma.200390087.

[4] P. D. Dapkus. 'A critical comparison of MOCVD and MBE for heterojunction devices'. In: *Journal of Crystal Growth* 68.1 (1984), pp. 345–355. DOI: 10.1016/0022-0248(84)90436-6.

[5] G. J. Davies and D. Williams. 'III–V MBE Growth Systems'. In: *The Technology and Physics of Molecular Beam Epitaxy.* Ed. by E. H. C. Parker. New York and London: Plenum, 1985. Chap. 2, pp. 15–46.

[6] J. D. Grange. 'The Growth of the MBE III–V Compounds and Alloys'. In: *The Technology and Physics of Molecular Beam Epitaxy.* Ed. by E. H. C. Parker. New York and London: Plenum, 1985. Chap. 3, pp. 47–59.

[7] T. F. Kuech. 'Metal-organic vapor phase epitaxy of compound semiconductors'. In: *Materials Science Reports* 2.1 (1987), pp. 1–49. DOI: 10.1016/0920-2307(87)90002-8.

[8] A. Wickenden, D. Koleske, R. Henry, M. Twigg and M. Fatemi. 'Resistivity control in unintentionally doped GaN films grown by MOCVD'. In: *Journal of Crystal Growth* 260.1–2 (2004), pp. 54–62. DOI: 10.1016/j.jcrysgro.2003.08.024.

[9] E. P. A. M. Bakkers, M. T. Borgström and M. A. Verheijen. 'Epitaxial Growth of III-V Nanowires on Group IV Substrates'. In: *MRS Bulletin* 32.2 (2007), pp. 117–122. DOI: 10.1557/mrs2007.43.

[10] K. Tomioka, M. Yoshimura and T. Fukui. ‘A III-V nanowire channel on silicon for high-performance vertical transistors’. In: *Nature* 488.7410 (2012), pp. 189–192. DOI: 10.1038/nature11293.

[11] Z. Mi and Y.-L. Chang. ‘III-V compound semiconductor nanostructures on silicon: epitaxial growth, properties, and applications in light emitting diodes and lasers’. In: *Journal of Nanophotonics* 3.1 (2009), pp. 031602–19. DOI: 10.1117/1.3081051.

[12] V. Dhaka, T. Haggren, H. Jussila, H. Jiang, E. Kauppinen, T. Huhtio, M. Sopanen and H. Lipsanen. ‘High Quality GaAs Nanowires Grown on Glass Substrates’. In: *Nano Letters* 12.4 (2012), pp. 1912–1918. DOI: 10.1021/nl204314z.

[13] Z. Yufeng, L. Xinhua, W. Wenbo, Z. Bukang, D. Huahua, S. Tongfei, Z. Xuesong, L. Ning and W. Yuqi. ‘Growth and properties of GaAs nanowires on fused quartz substrate’. In: *Journal of Semiconductors* 35.9 (2014), p. 093002. DOI: 10.1088/1674-4926/35/9/093002.

[14] P. K. Mohseni, A. Behnam, J. D. Wood, X. Zhao, K. J. Yu, N. C. Wang, A. Rockett, J. A. Rogers, J. W. Lyding, E. Pop and X. Li. ‘Monolithic III-V Nanowire Solar Cells on Graphene via Direct van der Waals Epitaxy’. In: *Advanced Materials* 26.22 (2014), pp. 3755–3760. DOI: 10.1002/adma.201305909.

[15] J. Wallentin, D. Kriegner, J. Stangl and M. T. Borgström. ‘Au-Seeded Growth of Vertical and in-Plane III–V Nanowires on Graphite Substrates’. In: *Nano Letters* 14.4 (2014), pp. 1707–1713. DOI: 10.1021/nl403411w.

[16] M. Heurlin, M. H. Magnusson, D. Lindgren, M. Ek, L. R. Wallenberg, K. Deppert and L. Samuelson. ‘Continuous gas-phase synthesis of nanowires with tunable properties’. In: *Nature* 492.7427 (2012), pp. 90–94. DOI: 10.1038/nature11652.

[17] K. W. Kolasinski. ‘Catalytic growth of nanowires: Vapor-liquid-solid, vapor-solid-solid, solution-liquid-solid and solid-liquid-solid growth’. In: *Current Opinion in Solid State and Materials Science* 10.3-4 (2006), pp. 182–191. DOI: 10.1016/j.cossms.2007.03.002.

[18] B. A. Wacaser, K. A. Dick, J. Johansson, M. T. Borgström, K. Deppert and L. Samuelson. ‘Preferential Interface Nucleation: An Expansion of the VLS Growth Mechanism for Nanowires’. In: *Advanced Materials* 21.2 (2009), pp. 153–165. DOI: 10.1002/adma.200800440.

[19] B. Mandl, J. Stangl, E. Hilner, A. A. Zakharov, K. Hillerich, A. W. Dey, L. Samuelson, G. Bauer, K. Deppert and A. Mikkelsen. 'Growth Mechanism of Self-Catalyzed Group III-V Nanowires'. In: *Nano Letters* 10.10 (2010), pp. 4443–4449. DOI: 10.1021/nl1022699.

[20] A. Govindaraj and C. N. R. Rao. 'Nanotubes and Nanowires'. In: *The Chemistry of Nanomaterials. Synthesis, Properties and Applications in 2 Volumes*. Ed. by C. N. R. Rao, A. Müller and A. K. Cheetham. Weinheim: Wiley-VCH, 2005. Chap. 8, pp. 208–284. DOI: 10.1002/352760247X.ch8.

[21] K. A. Bertness, A. W. Sanders, D. M. Rourke, T. E. Harvey, A. Roshko and N. A. Sanford. 'Controlled nucleation of GaN nanowires grown with molecular beam epitaxy'. In: *Advanced Functional Materials* 20.17 (2010), pp. 2911–2915. DOI: 10.1002/adfm.201000381.

[22] K. Cui, S. Fathololoumi, M. G. Kibria, G. A. Botton and Z. Mi. 'Molecular beam epitaxial growth and characterization of catalyst-free InN/$In_xGa_{1-x}N$ core/shell nanowire heterostructures on Si(111) substrates'. In: *Nanotechnology* 23.8 (2012), pp. 085205–. DOI: 10.1088/0957-4484/23/8/085205.

[23] D. Rudolph, S. Hertenberger, S. Bolte, W. Paosangthong, D. Spirkoska, M. Döblinger, M. Bichler, J. J. Finley, G. Abstreiter and G. Koblmüller. 'Direct Observation of a Noncatalytic Growth Regime for GaAs Nanowires'. In: *Nano Letters* 11.9 (2011), pp. 3848–3854. DOI: 10.1021/nl2019382.

[24] F. Jabeen, V. Grillo, S. Rubini and F. Martelli. 'Self-catalyzed growth of GaAs nanowires on cleaved Si by molecular beam epitaxy'. In: *Nanotechnology* 19.27 (2008), p. 275711. DOI: 10.1088/0957-4484/19/27/275711.

[25] K. Ikejiri, J. Noborisaka, S. Hara, J. Motohisa and T. Fukui. 'Mechanism of catalyst-free growth of GaAs nanowires by selective area MOVPE'. In: *Journal of Crystal Growth* 298 (2007), pp. 616–619. DOI: 10.1016/j.jcrysgro.2006.10.179.

[26] K. Ikejiri, T. Sato, H. Yoshida, K. Hiruma, J. Motohisa, S. Hara and T. Fukui. 'Growth characteristics of GaAs nanowires obtained by selective area metal-organic vapour-phase epitaxy'. In: *Nanotechnology* 19.26 (2008), p. 265604. DOI: 10.1088/0957-4484/19/26/265604.

[27] J. Noborisaka, J. Motohisa and T. Fukui. 'Catalyst-free growth of GaAs nanowires by selective-area metalorganic vapor-phase epitaxy'. In: *Applied Physics Letters* 86.21 (2005), p. 213102. DOI: 10.1063/1.1935038.

[28] S. Hertenberger, D. Rudolph, S. Bolte, M. Döblinger, M. Bichler, D. Spirkoska, J. J. Finley, G. Abstreiter and G. Koblmüller. 'Absence of vapor-liquid-solid growth during molecular beam epitaxy of self-induced InAs nanowires on Si'. In: *Applied Physics Letters* 98.12 (2011), p. 123114. DOI: 10.1063/1.3567496.

[29] C. Chèze, L. Geelhaar, B. Jenichen and H. Riechert. 'Different growth rates for catalyst-induced and self-induced GaN nanowires'. In: *Applied Physics Letters* 97.15 (2010), p. 153105. DOI: 10.1063/1.3488010.

[30] E. Calleja, M. A. Sánchez-García, F. J. Sánchez, F. Calle, F. B. Naranjo, E. Muñoz, U. Jahn and K. Ploog. 'Luminescence properties and defects in GaN nanocolumns grown by molecular beam epitaxy'. In: *Physical Review B* 62 (24 2000), pp. 16826–16834. DOI: 10.1103/PhysRevB.62.16826.

[31] T. Gotschke, T. Schumann, F. Limbach, T. Stoica and R. Calarco. 'Influence of the adatom diffusion on selective growth of GaN nanowire regular arrays'. In: *Applied Physics Letters* 98.10 (2011), pp. 103102–3. DOI: 10.1063/1.3559618.

[32] J. Johansson, B. A. Wacaser, K. A. Dick and W. Seifert. 'Growth related aspects of epitaxial nanowires'. In: *Nanotechnology* 17.11 (2006), S355–61. DOI: 10.1088/0957-4484/17/11/S21.

[33] K. A. Dick, K. Deppert, T. Mårtensson, B. Mandl, L. Samuelson and W. Seifert. 'Failure of the Vapor-Liquid-Solid Mechanism in Au-Assisted MOVPE Growth of InAs Nanowires'. In: *Nano Letters* 5.4 (2005), pp. 761–764. DOI: 10.1021/nl050301c.

[34] A. I. Persson, M. W. Larsson, S. Stenström, B. J. Ohlsson, L. Samuelson and L. R. Wallenberg. 'Solid-phase diffusion mechanism for GaAs nanowire growth'. In: *Nature Materials* 3 (2004), pp. 677–681. DOI: 10.1038/nmat1220.

[35] L. E. Jensen, M. T. Bjork, S. Jeppesen, A. I. Persson, B. J. Ohlsson and L. Samuelson. 'Role of Surface Diffusion in Chemical Beam Epitaxy of InAs Nanowires'. In: *Nano Letters* 4.10 (2004), pp. 1961–1964. DOI: 10.1021/nl048825k.

[36] R. S. Wagner and W. C. Ellis. 'Vapor-Liquid-Solid mechanism of single crystal growth'. In: *Applied Physics Letters* 4.5 (1964), pp. 89–90. DOI: 10.1063/1.1753975.

[37] R. S. Wagner, W. C. Ellis, K. A. Jackson and S. M. Arnold. 'Study of the Filamentary Growth of Silicon Crystals from the Vapor'. In: *Journal of Applied Physics* 35.10 (1964), pp. 2993–3000. DOI: 10.1063/1.1713143.

[38] E. I. Givargizov. 'Fundamental aspects of VLS growth'. In: *Journal of Crystal Growth* 31 (1975), pp. 20–30. DOI: 10.1016/0022-0248(75)90105-0.

[39] S. A. Fortuna and X. Li. 'Metal-catalyzed semiconductor nanowires: a review on the control of growth directions'. In: *Semiconductor Science and Technology* 25.2 (2010), pp. 024005–. DOI: 10.1088/0268-1242/25/2/024005.

[40] V. G. Dubrovskii, I. P. Soshnikov, G. E. Cirlin, A. A. Tonkikh, N. V. Samsonenko Yu. B.and Sibirev and V. M. Ustinov. 'On the non-monotonic lateral size dependence of the height of GaAs nanowhiskers grown by molecular beam epitaxy at high temperature'. In: *physica status solidi (b)* 241.7 (2004), R30–R33. DOI: 10.1002/pssb.200409042.

[41] V. G. Dubrovskii and N. V. Sibirev. 'Growth rate of a crystal facet of arbitrary size and growth kinetics of vertical nanowires'. In: *Physical Review E: Statistical, Nonlinear, and Soft Matter Physics* 70.3 (2004), p. 031604. DOI: 10.1103/PhysRevE.70.031604.

[42] V. G. Dubrovskii, G. E. Cirlin, I. P. Soshnikov, A. A. Tonkikh, N. V. Sibirev, Y. B. Samsonenko and V. M. Ustinov. 'Diffusion-induced growth of GaAs nanowhiskers during molecular beam epitaxy: Theory and experiment'. In: *Physical Review B* 71.20 (2005), pp. 205325–205331. DOI: 10.1103/PhysRevB.71.205325.

[43] V. G. Dubrovskii, N. V. Sibirev, G. E. Cirlin, J. C. Harmand and V. M. Ustinov. 'Theoretical analysis of the vapor-liquid-solid mechanism of nanowire growth during molecular beam epitaxy'. In: *Physical Review E: Statistical, Nonlinear, and Soft Matter Physics* 73.2, 021603 (2006), p. 021603. DOI: 10.1103/PhysRevE.73.021603.

[44] V. G. Dubrovskii and N. V. Sibirev. 'General form of the dependences of nanowire growth rate on the nanowire radius'. In: *Journal of Crystal Growth* 304 (2007), pp. 504–513. DOI: 10.1016/j.jcrysgro.2007.03.034.

[45] V. G. Dubrovskii, N. V. Sibirev, R. A. Suris, G. E. Cirlin, J. C. Harmand and V. M. Ustinov. 'Diffusion-controlled growth of semiconductor nanowires: Vapor pressure versus high vacuum deposition'. In: *Surface Science* 601 (2007), pp. 4395–4401. DOI: 10.1016/j.susc.2007.04.122.

[46] V. G. Dubrovskii and N. V. Sibirev. 'Growth thermodynamics of nanowires and its application to polytypism of zinc blende III-V nanowires'. In: *Physical Review B* 77.3, 035414 (2008), p. 035414. DOI: 10.1103/PhysRevB.77.035414.

[47] V. G. Dubrovskii, N. V. Sibirev, J. C. Harmand and F. Glas. 'Growth kinetics and crystal structure of semiconductor nanowires'. In: *Physical Review B: Condensed Matter and Materials Physics* 78.23, 235301 (2008), p. 235301. DOI: 10.1103/PhysRevB.78.235301.

[48] V. G. Dubrovskii, N. V. Sibirev, G. E. Cirlin, I. P. Soshnikov, W. H. Chen, R. Larde, E. Cadel, P. Pareige, T. Xu, B. Grandidier, J.-P. Nys, D. Stievenard, M. Moewe, L. C. Chuang and C. Chang-Hasnain. 'Gibbs-Thomson and diffusion-induced contributions to the growth rate of Si, InP, and GaAs

nanowires'. In: *Physical Review B* 79.20, 205316 (2009), p. 205316. DOI: 10.1103/PhysRevB.79.205316.

[49] V. G. Dubrovskii, G. E. Cirlin, N. V. Sibirev, F. Jabeen, J. C. Harmand and P. Werner. 'New Mode of Vapor-Liquid-Solid Nanowire Growth'. In: *Nano Letters* 11.3 (2011), pp. 1247–1253. DOI: 10.1021/nl104238d.

[50] J. C. Harmand, G. Patriarche, N. Péré-Laperne, M.-N. Mérat-Combes, L. Travers and F. Glas. 'Analysis of vapor-liquid-solid mechanism in Au-assisted GaAs nanowire growth'. In: *Applied Physics Letters* 87.20 (2005), p. 203101. DOI: 10.1063/1.2128487.

[51] J. C. Harmand, M. Tchernycheva, G. Patriarche, L. Travers, F. Glas and G. Cirlin. 'GaAs nanowires formed by Au-assisted molecular beam epitaxy: Effect of growth temperature'. In: *Journal of Crystal Growth* 301-302 (2007). 14th International Conference on Molecular Beam Epitaxy - MBE XIV, pp. 853–856. DOI: 10.1016/j.jcrysgro.2006.11.106.

[52] J.-C. Harmand, F. Glas and G. Patriarche. 'Growth kinetics of a single $InP_{1-x}As_x$ nanowire'. In: *Physical Review B* 81.23 (2010), pp. 235436–. DOI: 10.1103/PhysRevB.81.235436.

[53] F. Glas, J.-C. Harmand and G. Patriarche. 'Why Does Wurtzite Form in Nanowires of III-V Zinc Blende Semiconductors?' In: *Physical Review Letters* 99.14 (2007), pp. 146101–4. DOI: 10.1103/PhysRevLett.99.146101.

[54] F. Glas, J.-C. Harmand and G. Patriarche. 'Nucleation Antibunching in Catalyst-Assisted Nanowire Growth'. In: *Physical Review Letters* 104.13 (2010), pp. 135501–. DOI: 10.1103/PhysRevLett.104.135501.

[55] F. Glas. 'Chemical potentials for Au-assisted vapor-liquid-solid growth of III-V nanowires'. In: *Journal of Applied Physics* 108.7 (2010), pp. 073506–6. DOI: 10.1063/1.3488908.

[56] A. Rudolph. 'MBE Growth of GaAs Nanowires and Nanowire Heterostructures'. PhD thesis. Universität Regensburg, 2012. eprint: http://epub.uni-regensburg.de/25631/.

[57] M. Soda, A. Rudolph, D. Schuh, J. Zweck, D. Bougeard and E. Reiger. 'Transition from Au to pseudo-Ga catalyzed growth mode observed in GaAs nanowires grown by molecular beam epitaxy'. In: *Physical Review B* 85.24 (2012), p. 245450. DOI: 10.1103/PhysRevB.85.245450.

[58] C. Colombo, D. Spirkoska, M. Frimmer, G. Abstreiter and A. Fontcuberta i Morral. 'Ga-assisted catalyst-free growth mechanism of GaAs nanowires by molecular beam epitaxy'. In: *Physical Review B* 77.15 (2008), p. 155326. DOI: 10.1103/PhysRevB.77.155326.

[59] P. Krogstrup, H. I. Jørgensen, E. Johnson, M. H. Madsen, C. B. Sørensen, A. Fontcuberta i Morral, M. Aagesen, J. Nygård and F. Glas. 'Advances in the theory of III–V nanowire growth dynamics'. In: *Journal of Physics D: Applied Physics* 46.31 (2013), p. 313001. DOI: doi:10.1088/0022-3727/46/31/313001. arXiv: 1301.7441v3 [cond-mat.mes-hall].

[60] M. Mattila, T. Hakkarainen, H. Lipsanen, H. Jiang and E. I. Kauppinen. 'Catalyst-free growth of In(As)P nanowires on silicon'. In: *Applied Physics Letters* 89.6 (2006), p. 063119. DOI: 10.1063/1.2336599.

[61] M. Mattila, T. Hakkarainen, H. Jiang, E. I. Kauppinen and H. Lipsanen. 'Effect of substrate orientation on the catalyst-free growth of InP nanowires'. In: *Nanotechnology* 18.15 (2007), pp. 155301–. DOI: 10.1088/0957-4484/18/15/155301.

[62] F. Glas, M. R. Ramdani, G. Patriarche and J.-C. Harmand. 'Predictive modeling of self-catalyzed III-V nanowire growth'. In: *Physical Review B* 88.19 (2013), pp. 195304–. DOI: 10.1103/PhysRevB.88.195304.

[63] M. R. Ramdani, J.-C. Harmand, F. Glas, G. Patriarche and L. Travers. 'Arsenic pathways in self-catalyzed growth of GaAs nanowires'. In: *Crystal Growth & Design* 13.1 (2013), pp. 91–96. DOI: 10.1021/cg301167g.

[64] F. Matteini, V. G. Dubrovskii, D. Rüffer, G. Tütüncüoğlu, Y. Fontana and A. Fontcuberta i Morral. 'Tailoring the diameter and density of self-catalyzed GaAs nanowires on silicon'. In: *Nanotechnology* 26.10 (2015), pp. 105603–. DOI: 10.1088/0957-4484/26/10/105603.

[65] P. Krogstrup, R. Popovitz-Biro, E. Johnson, M. H. Madsen, J. Nygård and H. Shtrikman. 'Structural Phase Control in Self-Catalyzed Growth of GaAs Nanowires on Silicon (111)'. In: *Nano Letters* 10.11 (2010), pp. 4475–4482. DOI: 10.1021/nl102308k.

[66] A. Fontcuberta i Morral, C. Colombo, G. Abstreiter, J. Arbiol and J. R. Morante. 'Nucleation mechanism of gallium-assisted molecular beam epitaxy growth of gallium arsenide nanowires'. In: *Applied Physics Letters* 92.6 (2008), p. 063112. DOI: 10.1063/1.2837191; A. Fontcuberta i Morral, K. Maslov, C. Colombo, G. Abstreiter, J. Arbiol and J. R. Morante. 'Erratum: "Nucleation mechanism of gallium-assisted molecular beam epitaxy growth of gallium arsenide nanowires"'. In: *Applied Physics Letters* 92.14 (2008), p. 149903. DOI: 10.1063/1.2894500.

[67] M. Bar-Sadan, J. Barthel, H. Shtrikman and L. Houben. 'Direct Imaging of Single Au Atoms Within GaAs Nanowires'. In: *Nano Letters* 12.5 (2012), p. 2352. DOI: 10.1021/nl300314k.

[68] S. Breuer, C. Pfüller, T. Flissikowski, O. Brandt, H. T. Grahn, L. Geelhaar and H. Riechert. 'Suitability of Au- and Self-Assisted GaAs Nanowires for Optoelectronic Applications'. In: *Nano Letters* 11.3 (2011), pp. 1276–1279. DOI: 10.1021/nl104316t.

[69] M. Law, J. Goldberger and P. Yang. 'Semiconductor nanowires and nanotubes'. In: *Annual Review of Materials Research* 34.1 (2004), pp. 83–122. DOI: 10.1146/annurev.matsci.34.040203.112300.

[70] T. D. Stanescu and S. Tewari. 'Majorana fermions in semiconductor nanowires: fundamentals, modeling, and experiment'. In: *Journal of Physics: Condensed Matter* 25.23 (2013), pp. 233201–. DOI: 10.1088/0953-8984/25/23/233201.

[71] V. Mourik, K. Zuo, S. M. Frolov, S. R. Plissard, E. P. A. M. Bakkers and L. P. Kouwenhoven. 'Signatures of Majorana Fermions in Hybrid Superconductor-Semiconductor Nanowire Devices'. In: *Science* 336.6084 (2012), pp. 1003–1007. DOI: 10.1126/science.1222360.

[72] R. M. Penner. 'Chemical Sensing with Nanowires'. In: *Annual Review of Analytical Chemistry* 5.1 (2012), pp. 461–485. DOI: 10.1146/annurev-anchem-062011-143007.

[73] A. Cao, E. J. Sudhölter and L. C. de Smet. 'Silicon Nanowire-Based Devices for Gas-Phase Sensing'. In: *Sensors* 14.1 (2013), pp. 245–271. DOI: 10.3390/s140100245.

[74] E. H. Williams, A. V. Davydov, V. P. Oleshko, K. L. Steffens, I. Levin, N. J. Lin, K. A. Bertness, A. K. Manocchi, J. A. Schreifels and M. V. Rao. 'Solution-based functionalization of gallium nitride nanowires for protein sensor development'. In: *Surface Science* 627 (2014), pp. 23–28. DOI: 10.1016/j.susc.2014.04.010.

[75] L. Su, G. Lu, B. Kenens, S. Rocha, E. Fron, H. Yuan, C. Chen, P. Van Dorpe, M. B. J. Roeffaers, H. Mizuno, J. Hofkens, J. A. Hutchison and H. Uji-i. 'Visualization of molecular fluorescence point spread functions via remote excitation switching fluorescence microscopy'. In: *Nature Communications* 6.6287 (2015). DOI: 10.1038/ncomms7287.

[76] P. Krogstrup, H. I. Jorgensen, M. Heiss, O. Demichel, J. V. Holm, M. Aagesen, J. Nygard and A. Fontcuberta i Morral. 'Single-nanowire solar cells beyond the Shockley-Queisser limit'. In: *Nature Photonics* 7.4 (2013), pp. 306–310. DOI: 10.1038/nphoton.2013.32.

[77] J. Wallentin, N. Anttu, D. Asoli, M. Huffman, I. Åberg, M. H. Magnusson, G. Siefer, P. Fuss-Kailuweit, F. Dimroth, B. Witzigmann, H. Q. Xu, L. Samuelson, K. Deppert and M. T. Borgström. 'InP Nanowire Array Solar Cells Achieving 13.8% Efficiency by Exceeding the Ray Optics Limit'. In: *Science* 339.6123 (2013), pp. 1057–1060. DOI: 10.1126/science.1230969.

[78] K. Seo, T. Lim, S. Kim, H.-L. Park and S. Lu. 'Tunable-white-light-emitting nanowire sources'. In: *Nanotechnology* 21.25 (2010), pp. 255201–. DOI: 10.1088/0957-4484/21/25/255201.

[79] R. Wang, H. P. T. Nguyen, A. T. Connie, J. Lee, I. Shih and Z. Mi. 'Color-tunable, phosphor-free InGaN nanowire light-emitting diode arrays monolithically integrated on silicon'. In: *Optics Express* 22.S7 (2014), A1768–A1775. DOI: 10.1364/OE.22.0A1768.

[80] T. R. Kuykendall, A. M. Schwartzberg and S. Aloni. 'Gallium Nitride Nanowires and Heterostructures: Toward Color-Tunable and White-Light Sources'. In: *Advanced Materials* (2015). DOI: 10.1002/adma.201500522.

[81] H. Riel, L.-E. Wernersson, M. Hong and J. A. del Alamo. 'III–V compound semiconductor transistors—from planar to nanowire structures'. In: *MRS Bulletin* 39.08 (2014): *New Materials for Post-Si Computing*, pp. 668–677. DOI: 10.1557/mrs.2014.137.

[82] L.-E. Wernersson. 'III–V nanowires for logics and beyond'. In: *Microelectronic Engineering* 147 (2015): *Insulating Films on Semiconductors 2015*, pp. 344–348. DOI: 10.1016/j.mee.2015.04.122.

[83] P. Caroff, M. E. Messing, B. M. Borg, K. A. Dick, K. Deppert and L.-E. Wernersson. 'InSb heterostructure nanowires: MOVPE growth under extreme lattice mismatch'. In: *Nanotechnology* 20.49 (2009), pp. 495606–495612. DOI: 10.1088/0957-4484/20/49/495606.

[84] L. C. Chuang, M. Moewe, C. Chase, N. P. Kobayashi, C. Chang-Hasnain and S. Crankshaw. 'Critical diameter for III-V nanowires grown on lattice-mismatched substrates'. In: *Applied Physics Letters* 90.4 (2007), pp. 043115–3. DOI: 10.1063/1.2436655.

[85] S. Noor Mohammad. 'Why self-catalyzed nanowires are most suitable for large-scale hierarchical integrated designs of nanowire nanoelectronics'. In: *Journal of Applied Physics* 110.8 (2011), pp. 084310–. DOI: 10.1063/1.3624585.

[86] J. P. Boulanger and R. R. LaPierre. 'Polytype formation in GaAs/GaP axial nanowire heterostructures'. In: *Journal of Crystal Growth* 332.1 (2011), pp. 21–26. DOI: 10.1016/j.jcrysgro.2011.07.021.

[87] Y. A. Du, S. Sakong and P. Kratzer. 'As vacancies, Ga antisites and Au impurities in Zincblende and Wurtzite GaAs nanowire segments from first principles'. In: *Physical Review B* 87.7 (2013), p. 075308. DOI: 10.1103/PhysRevB.87.075308. arXiv: 1301.7339 [cond-mat.mtrl-sci].

[88] F. R. N. Nabarro. *Theory of Crystal Dislocations*. International series of monographs on physics. London et al.: Oxford University Press, 1967.

[89] J. Kepler. *Vom sechseckigen Schnee*. (originally published as *De niue sexangula*. 1611). Latin and German. Ed., trans. from the Latin and comm. by L. Dunsch. With annots. by L. Dunsch. Opera Selecta Humaniora. Dresden: Hellerau, 2005.

[90] R. Hooke. *Micrographia. Some Physiological Descriptions of Minute Bodies Made by Magnifying Glasses with Observations and Inquiries Thereupon*. London, 1665.

[91] C. Huygens. *Treatise on Light*. (originally published as *Traité de la Lumière*. 1690). Trans. from the French by S. P. Thompson. 1912.

[92] W. H. Wollaston. 'The Bakerian Lecture: On the Elementary Particles of Certain Crystals'. In: *Philosophical Transactions of the Royal Society of London* 103 (1813), pp. 51–63. DOI: 10.1098/rstl.1813.0008.

[93] W. Barlow. 'Probable Nature of the Internal Symmetry of Crystals'. In: *Nature* 29 (1883), pp. 186–188. DOI: 10.1038/029186a0; W. Barlow. 'Probable Nature of the Internal Symmetry of Crystals'. (continued). In: *Nature* 29 (1883), pp. 205–207. DOI: 10.1038/029205a0.

[94] User 'Twisp'. *File:Close Packing.svg*. Wikimedia Commons. 2008. URL: https://commons.wikimedia.org/w/index.php?title=File:Close_packing.svg&oldid=34733456 (visited on 21/05/2014). Licensed as public domain.

[95] A. Bishop. *An outline of crystal morphology*. London et al.: Hutchinson, 1967.

[96] C. Hammond. *Introduction to Crystallography*. Royal Microscopical Society Microscopy Handbooks 19. Oxford University Press, 1990.

[97] J. P. Hirth and J. Lothe. *Theory of dislocations*. McGraw-Hill series in material science and engineering. New York et al.: McGraw-Hill, 1968.

[98] A. Belabbes, J. Furthmüller and F. Bechstedt. 'Relation between spontaneous polarization and crystal field from first principles'. In: *Physical Review B* 87.3 (2013), p. 035305. DOI: 10.1103/PhysRevB.87.035305.

[99] C. Frondel and U. B. Marvin. 'Lonsdaleite, a Hexagonal Polymorph of Diamond'. In: *Nature* 214.5088 (1967), pp. 587–589. DOI: 10.1038/214587a0.

[100] F. P. Bundy and J. S. Kasper. 'Hexagonal Diamond—A New Form of Carbon'. In: *Journal of Chemical Physics* 46.9 (1967), pp. 3437–3446. DOI: 10.1063/1.1841236.

[101] A. Fontcuberta i Morral, J. Arbiol, J. D. Prades, A. Cirera and J. R. Morante. 'Synthesis of Silicon Nanowires with Wurtzite Crystalline Structure by Using Standard Chemical Vapor Deposition'. In: *Advanced Materials* 19.10 (2007), pp. 1347–1351. DOI: 10.1002/adma.200602318.

[102] P. Y. Yu and M. Cardona. 'Electronic Band Structures'. In: *Fundamentals of Semiconductors. Physics and Materials Properties.* 4th ed. Graduate Texts in Physics. Berlin and Heidelberg: Springer, 2010, pp. 17–106. DOI: 10.1007/978-3-642-00710-1.

[103] R. W. Nosker, P. Mark and J. D. Levine. 'Polar surfaces of wurtzite and zincblende lattices'. In: *Surface Science* 19.2 (1970), pp. 291–317. DOI: 10.1016/0039-6028(70)90040-3.

[104] M. Stutzmann, O. Ambacher, M. Eickhoff, U. Karrer, A. Lima Pimenta, R. Neuberger, J. Schalwig, R. Dimitrov, P. Schuck and R. Grober. 'Playing with Polarity'. In: *physica status solidi (b)* 228.2 (2001), pp. 505–512. DOI: 10.1002/1521-3951(200111)228:2<505::AID-PSSB505>3.0.CO;2-U.

[105] J. Johansson, L. S. Karlsson, C. P. T. Svensson, T. Mårtensson, B. A. Wacaser, K. Deppert, L. Samuelson and W. Seifert. 'Structural properties of ⟨111⟩ B-oriented III–V nanowires'. In: *Nature Materials* 5 (2006), pp. 574–580. DOI: 10.1038/nmat1677.

[106] Z. H. Wu, X. Y. Mei, D. Kim, M. Blumin and H. E. Ruda. 'Growth of Au-catalyzed ordered GaAs nanowire arrays by molecular-beam epitaxy'. In: *Applied Physics Letters* 81.27 (2002), pp. 5177–5179. DOI: 10.1063/1.1532772.

[107] X. Li, H. Guo, Z. Yin, T. Shi, L. Wen, Z. Zhao, M. Liu, W. Ma and Y. Wang. 'Morphology and crystal structure control of GaAs nanowires grown by Au-assisted MBE with solid As4 source'. In: *Journal of Crystal Growth* 324.1 (2011), pp. 82–87. DOI: 10.1016/j.jcrysgro.2011.04.004.

[108] B. A. Wacaser, K. Deppert, L. S. Karlsson, L. Samuelson and W. Seifert. 'Growth and characterization of defect free GaAs nanowires'. In: *Journal of Crystal Growth* 287.2 (2006), pp. 504–508. DOI: 10.1016/j.jcrysgro.2005.11.075.

[109] E. Janik, P. Dłużewski, S. Kret, A. Presz, H. Kirmse, W. Neumann, W. Zaleszczyk, L. T. Baczewski, A. Petroutchik, E. Dynowska, J. Sadowski, W. Caliebe, G. Karczewski and T. Wojtowicz. ‘Catalytic growth of ZnTe nanowires by molecular beam epitaxy: structural studies’. In: *Nanotechnology* 18.47 (2007), 475606 (8pp). DOI: 10.1088/0957-4484/18/47/475606.

[110] S. C. Lee, L. R. Dawson, S. R. J. Brueck and Y.-B. Jiang. ‘Anisotropy of selective epitaxy in nanoscale-patterned growth: GaAs nanowires selectively grown on a SiO_2-patterned (001) substrate by molecular-beam epitaxy’. In: *Journal of Applied Physics* 98.11 (2005), p. 114312. DOI: 10.1063/1.2132093.

[111] M. Rosini and R. Magri. ‘Surface Effects on the Atomic and Electronic Structure of Unpassivated GaAs Nanowires’. In: *ACS Nano* 4.10 (2010), pp. 6021–6031. DOI: 10.1021/nn1015488.

[112] S. T. Weir, Y. K. Vohra, C. A. Vanderborgh and A. L. Ruoff. ‘Structural phase transitions in GaAs to 108 GPa’. In: *Physical Review B* 39 (2 1989), pp. 1280–1285. DOI: 10.1103/PhysRevB.39.1280.

[113] M. I. McMahon and R. J. Nelmes. ‘Observation of a Wurtzite Form of Gallium Arsenide’. In: *Physical Review Letters* 95.21 (2005), pp. 215505–. DOI: 10.1103/PhysRevLett.95.215505.

[114] G. J. Ackland. ‘High-pressure phases of group IV and III-V semiconductors’. In: *Reports on Progress in Physics* 64.4 (2001), pp. 483–. DOI: 10.1088/0034-4885/64/4/202.

[115] R. Gurwitz, A. Tavor, L. Karpeles, I. Shalish, W. Yi, G. Seryogin and V. Narayanamurti. ‘Bandgap and band discontinuity in wurtzite/zincblende GaAs homomaterial heterostructure’. In: *Applied Physics Letters* 100.19 (2012), pp. 191602–3. DOI: 10.1063/1.4712562.

[116] C.-Y. Yeh, Z. W. Lu, S. Froyen and A. Zunger. ‘Zinc-blende–wurtzite polytypism in semiconductors’. In: *Physical Review B* 46.16 (1992), pp. 10086–10097. DOI: 10.1103/PhysRevB.46.10086.

[117] F. Glas. ‘A simple calculation of energy changes upon stacking fault formation or local crystalline phase transition in semiconductors’. In: *Journal of Applied Physics* 104.9 (2008), p. 093520. DOI: 10.1063/1.3009338.

[118] T. Ito, T. Akiyama and K. Nakamura. ‘Simple Systematization of Structural Stability for $A^N B^{8-N}$ Compounds’. In: *Japanese Journal of Applied Physics* 46.1R (2007), pp. 345–. DOI: 10.1143/JJAP.46.345.

[119] T. Ito. ‘Simple Criterion for Wurtzite-Zinc-Blende Polytypism in Semiconductors’. In: *Japanese Journal of Applied Physics* 37.10B (1998), pp. L1217–. DOI: 10.1143/JJAP.37.L1217.

[120] T. Akiyama, K. Sano, K. Nakamura and T. Ito. 'An Empirical Potential Approach to Wurtzite–Zinc-Blende Polytypism in Group III–V Semiconductor Nanowires'. In: *Japanese Journal of Applied Physics* 45.3L (2006), pp. L275–. DOI: 10.1143/JJAP.45.L275.

[121] A. Mujica, R. J. Needs and A. Muñoz. 'First-principles pseudopotential study of the phase stability of the III-V semiconductors GaAs and AlAs'. In: *Physical Review B* 52 (12 1995), pp. 8881–8892. DOI: 10.1103/PhysRevB.52.8881.

[122] A. Bautista-Hernández, L. Pérez-Arrieta, U. Pal and J. Rivas-Silva. 'Estudio estructural de los semiconductores AlP, GaAs y AlAs con estructura wurzita'. In: *Revista Mexicana de Física* 49.1 (2003), pp. 9–14.

[123] H. Shtrikman, R. Popovitz-Biro, A. Kretinin, L. Houben, M. Heiblum, M. Bukała, M. Galicka, R. Buczko and P. Kacman. 'Method for Suppression of Stacking Faults in Wurtzite III–V Nanowires'. In: *Nano Letters* 9.4 (2009), pp. 1506–1510. DOI: 10.1021/nl803524s.

[124] M. Galicka, M. Bukała, R. Buczko and P. Kacman. 'Modelling the structure of GaAs and InAs nanowires'. In: *Journal of Physics: Condensed Matter* 20.45 (2008), pp. 454226–. DOI: 10.1088/0953-8984/20/45/454226.

[125] R. Leitsmann and F. Bechstedt. 'Surface influence on stability and structure of hexagon-shaped III-V semiconductor nanorods'. In: *Journal of Applied Physics* 102.6 (2007), p. 063528. DOI: 10.1063/1.2783899.

[126] T. Rieger, M. I. Lepsa, T. Schäpers and D. Grützmacher. 'Controlled wurtzite inclusions in self-catalyzed zinc blende III–V semiconductor nanowires'. In: *Journal of Crystal Growth* 378 (2013): *The 17th International Conference on Molecular Beam Epitaxy*. Ed. by K. Akimoto, T. Suemasu and H. Okumura, pp. 506–510. DOI: 10.1016/j.jcrysgro.2012.12.035.

[127] L. Ahtapodov, J. Todorovic, P. Olk, T. Mjåland, P. Slåttnes, D. L. Dheeraj, A. T. J. van Helvoort, B.-O. Fimland and H. Weman. 'A Story Told by a Single Nanowire: Optical Properties of Wurtzite GaAs'. In: *Nano Letters* 12.12 (2012), pp. 6090–6095. DOI: 10.1021/nl3025714.

[128] T. Ba Hoang, A. F. Moses, L. Ahtapodov, H. Zhou, D. L. Dheeraj, A. T. J. van Helvoort, B.-O. Fimland and H. Weman. 'Engineering Parallel and Perpendicular Polarized Photoluminescence from a Single Semiconductor Nanowire by Crystal Phase Control'. In: *Nano Letters* (2010), pp. 2927–2933. DOI: 10.1021/nl101087e.

[129] M. Heiß, S. Conesa-Boj, J. Ren, H.-H. Tseng, A. Gali, A. Rudolph, E. Uccelli, F. Peiró, J. R. Morante, D. Schuh, E. Reiger, E. Kaxiras, J. Arbiol and A. Fontcuberta i Morral. 'Direct correlation of crystal structure and optical properties in wurtzite/zinc-blende GaAs nanowire heterostructures'. In: *Physical Review B* 83.4 (2011), p. 045303. DOI: 10.1103/PhysRevB.83.045303.

[130] D. L. Dheeraj, A. M. Munshi, M. Scheffler, A. T. J. van Helvoort, H. Weman and B. O. Fimland. 'Controlling crystal phases in GaAs nanowires grown by Au-assisted molecular beam epitaxy'. In: *Nanotechnology* 24.1 (2013), pp. 015601–. DOI: 10.1088/0957-4484/24/1/015601.

[131] M. J. Tambe, S. K. Lim, M. J. Smith, L. F. Allard and S. Gradečak. 'Realization of defect-free epitaxial core-shell GaAs/AlGaAs nanowire heterostructures'. In: *Applied Physics Letters* 93.15 (2008), pp. 151917–3. DOI: 10.1063/1.3002299.

[132] D. Kriegner, C. Panse, B. Mandl, K. A. Dick, M. Keplinger, J. M. Persson, P. Caroff, D. Ercolani, L. Sorba, F. Bechstedt, J. Stangl and G. Bauer. 'Unit Cell Structure of Crystal Polytypes in InAs and InSb Nanowires'. In: *Nano Letters* 11.4 (2011), pp. 1483–1489. DOI: 10.1021/nl1041512.

[133] J. Todorovic, A. F. Moses, T. Karlberg, P. Olk, D. L. Dheeraj, B. O. Fimland, H. Weman and A. T. J. van Helvoort. 'Correlated micro-photoluminescence and electron microscopy studies of the same individual heterostructured semiconductor nanowires'. In: *Nanotechnology* 22.32 (2011), pp. 325707–. DOI: 10.1088/0957-4484/22/32/325707.

[134] J. W. Christian and V. Vítek. 'Dislocations and stacking faults'. In: *Reports on Progress in Physics* 33.1 (1970), pp. 307–. DOI: 10.1088/0034-4885/33/1/307.

[135] C. Stampfl and C. G. Van de Walle. 'Energetics and electronic structure of stacking faults in AlN, GaN, and InN'. In: *Physical Review B* 57.24 (1998), R15052–R15055. DOI: 10.1103/PhysRevB.57.R15052.

[136] D. Gerthsen and C. B. Carter. 'Stacking-Fault Energies of GaAs'. In: *physica status solidi (a)* 136.1 (1993), pp. 29–43. DOI: 10.1002/pssa.2211360104.

[137] S. Takeuchi and K. Suzuki. 'Stacking Fault Energies of Tetrahedrally Coordinated Crystals'. In: *physica status solidi (a)* 171.1 (1999), pp. 99–103. DOI: 10.1002/(SICI)1521-396X(199901)171:1<99::AID-PSSA99>3.0.CO;2-B.

[138] H. Gottschalk, G. Patzer and H. Alexander. 'Stacking fault energy and ionicity of cubic III–V compounds'. In: *physica status solidi (a)* 45.1 (1978), pp. 207–217. DOI: 10.1002/pssa.2210450125.

[139] R. E. Algra, M. A. Verheijen, M. T. Borgstrom, L.-F. Feiner, G. Immink, W. J. P. van Enckevort, E. Vlieg and E. P. A. M. Bakkers. 'Twinning superlattices in indium phosphide nanowires'. In: *Nature* 456.7220 (2008), pp. 369–372. DOI: 10.1038/nature07570.

[140] P. Caroff, K. A. Dick, J. Johansson, M. E. Messing, K. Deppert and L. Samuelson. 'Controlled polytypic and twin-plane superlattices in III-V nanowires'. In: *Nature Nanotechnology* 4.1 (2009), pp. 50–55. DOI: 10.1038/nnano.2008.359.

[141] K. A. Dick, P. Caroff, J. Bolinsson, M. E. Messing, J. Johansson, K. Deppert, L. R. Wallenberg and L. Samuelson. 'Control of III-V nanowire crystal structure by growth parameter tuning'. In: *Semiconductor Science and Technology* 25.2 (2010), pp. 024009–. DOI: 10.1088/0268-1242/25/2/024009.

[142] Q. Xiong, J. Wang and P. C. Eklund. 'Coherent Twinning Phenomena: Towards Twinning Superlattices in III-V Semiconducting Nanowires'. In: *Nano Letters* 6.12 (2006), pp. 2736–2742. DOI: 10.1021/nl0616983.

[143] G. Priante, J.-C. Harmand, G. Patriarche and F. Glas. 'Random stacking sequences in III-V nanowires are correlated'. In: *Physical Review B* 89 (24 2014), p. 241301. DOI: 10.1103/PhysRevB.89.241301.

[144] O. Ambacher and V. Cimalla. 'Polarization Induced Effects in GaN-based Heterostructures and Novel Sensors'. In: *Polarization Effects in Semiconductors. From Ab Initio Theory to Device Applications.* Ed. by C. Wood and D. Jena. New York and London: Springer, 2008, pp. 27–110. DOI: 10.1007/978-0-387-68319-5.

[145] P. Lawaetz. 'Stability of the Wurtzite Structure'. In: *Physical Review B* 5.10 (1972), pp. 4039–4045. DOI: 10.1103/PhysRevB.5.4039.

[146] C. Panse, D. Kriegner and F. Bechstedt. 'Polytypism of GaAs, InP, InAs, and InSb: An ab initio study'. In: *Physical Review B* 84.7 (2011), p. 075217. DOI: 10.1103/PhysRevB.84.075217.

[147] H. Y. Al-Zahrani, J. Pal, M. A. Migliorato, G. Tse and D. Yu. 'Piezoelectric field enhancement in III–V core–shell nanowires'. In: *Nano Energy* 14 (2014): *Special issue on the 2nd International Conference on Nanogenerators and Piezotronics (NGPT 2014)*, pp. 382–391. DOI: 10.1016/j.nanoen.2014.11.046.

[148] A. Biermanns. 'X-ray diffraction from single GaAs nanowires'. PhD thesis. Siegen: Universität Siegen, 2012. eprint: http://dokumentix.ub.uni-siegen.de/opus/volltexte/2012/675.

[149] M. Tchernycheva, J. C. Harmand, G. Patriarche, L. Travers and G. E. Cirlin. ‘Temperature conditions for GaAs nanowire formation by Au-assisted molecular beam epitaxy’. In: *Nanotechnology* 17.16 (2006), pp. 4025–4030. DOI: 10.1088/0957-4484/17/16/005.

[150] R. Nelmes and M. McMahon. ‘Structural Transitions in the Group IV, III–V, and II–VI Semiconductors under Pressure’. In: *Semiconductors and Semimetals*. Vol. 54: *High Pressure in Semiconductor Physics I*. Ed. by T. Suski and W. Paul. San Diego and London: Elsevier and Academic Press, 1998. Chap. 2, pp. 145–246. DOI: 10.1016/S0080-8784(08)60231-8.

[151] S. Assali, I. Zardo, S. Plissard, D. Kriegner, M. A. Verheijen, G. Bauer, A. Meijerink, A. Belabbes, F. Bechstedt, J. E. M. Haverkort and E. P. A. M. Bakkers. ‘Direct Band Gap Wurtzite Gallium Phosphide Nanowires’. In: *Nano Letters* 13.4 (2013), pp. 1559–1563. DOI: 10.1021/nl304723c.

[152] D. Kriegner, S. Assali, A. Belabbes, T. Etzelstorfer, V. Holý, T. Schülli, F. Bechstedt, E. P. A. M. Bakkers, G. Bauer and J. Stangl. ‘Unit cell structure of the wurtzite phase of GaP nanowires: X-ray diffraction studies and density functional theory calculations’. In: *Physical Review B* 88.11 (2013), p. 115315. DOI: 10.1103/PhysRevB.88.115315.

[153] A. Biermanns, S. Breuer, A. Trampert, A. Davydok, L. Geelhaar and U. Pietsch. ‘Strain accommodation in Ga-assisted GaAs nanowires grown on silicon (111)’. In: *Nanotechnology* 23.30 (2012), p. 305703. DOI: 10.1088/0957-4484/23/30/305703.

[154] H. Morkoç and J. Leach. ‘Polarization in GaN Based Heterostructures and Heterojunction Field Effect Transistors (HFETs)’. In: *Polarization Effects in Semiconductors. From Ab Initio Theory to Device Applications*. Ed. by C. Wood and D. Jena. New York and London: Springer, 2008, pp. 373–466. DOI: 10.1007/978-0-387-68319-5.

[155] D. Jena. ‘Polarization Effects on Low-Field Transport & Mobility in III–V Nitride HEMTs’. In: *Polarization Effects in Semiconductors. From Ab Initio Theory to Device Applications*. Ed. by C. Wood and D. Jena. New York and London: Springer, 2008, pp. 161–216. DOI: 10.1007/978-0-387-68319-5.

[156] R. Butté and N. Grandjean. ‘Effects of Polarization in Optoelectronic Quantum Structures’. In: *Polarization Effects in Semiconductors. From Ab Initio Theory to Device Applications*. Ed. by C. Wood and D. Jena. New York and London: Springer, 2008, pp. 467–512. DOI: 10.1007/978-0-387-68319-5.

[157] R. D. King-Smith and D. Vanderbilt. 'Theory of polarization of crystalline solids'. In: *Physical Review B* 47 (3 1993), pp. 1651–1654. DOI: 10.1103/PhysRevB.47.1651.

[158] R. Resta. 'Macroscopic polarization in crystalline dielectrics: the geometric phase approach'. In: *Reviews of Modern Physics* 66 (3 1994), pp. 899–915. DOI: 10.1103/RevModPhys.66.899.

[159] P. Boguslawski and J. Bernhole. 'Theoretical Approach to Polarization Effects in Semiconductors'. In: *Polarization Effects in Semiconductors. From Ab Initio Theory to Device Applications*. Ed. by C. Wood and D. Jena. New York and London: Springer, 2008, pp. 1–26. DOI: 10.1007/978-0-387-68319-5.

[160] R. Resta and D. Vanderbilt. 'Theory of Polarization: A Modern Approach'. In: *Physics of Ferroelectrics. A Modern Perspective*. Ed. by K. M. Rabe, C. H. Ahn and J.-M. Triscone. Vol. 105. Topics in Applied Physics. Berlin and Heidelberg: Springer, 2007, pp. 31–68. DOI: 10.1007/978-3-540-34591-6.

[161] K. Song, C. T. Koch, J. K. Lee, D. Y. Kim, J. K. Kim, A. Parvizi, W. Y. Jung, C. G. Park, H. J. Jeong, H. S. Kim, Y. Cao, T. Yang, L.-Q. Chen and S. H. Oh. 'Correlative High-Resolution Mapping of Strain and Charge Density in a Strained Piezoelectric Multilayer'. In: *Advanced Materials Interfaces* 2.1 (2015), p. 1400281. DOI: 10.1002/admi.201400281.

[162] J. Lähnemann, O. Brandt, U. Jahn, C. Pfüller, C. Roder, P. Dogan, F. Grosse, A. Belabbes, F. Bechstedt, A. Trampert and L. Geelhaar. 'Direct experimental determination of the spontaneous polarization of GaN'. In: *Physical Review B* 86.8 (2012), pp. 081302–. DOI: 10.1103/PhysRevB.86.081302. arXiv: 1201.4294 [cond-mat.mtrl-sci].

[163] J. Lähnemann. 'Luminescence of group-III-V nanowires containing heterostructures. The role of polytypism, polarization fields and carrier localization'. PhD thesis. Berlin: Humboldt-Universität, 2013. eprint: http://edoc.hu-berlin.de/docviews/abstract.php?id=40255.

[164] L. Li, Z. Gan, M. R. McCartney, H. Liang, H. Yu, W.-J. Yin, Y. Yan, Y. Gao, J. Wang and D. J. Smith. 'Determination of Polarization-Fields Across Polytype Interfaces in InAs Nanopillars'. In: *Advanced Materials* 26.7 (2014), pp. 1052–1057. DOI: 10.1002/adma.201304021.

[165] L. Li, L. Jin, J. Wang, D. J. Smith, W.-J. Yin, Y. Yan, H. Sang, W. C. H. Choy and M. R. McCartney. 'Polarization-Induced Charge Distribution at Homogeneous Zincblende/Wurtzite Heterostructural Junctions in ZnSe Nanobelts'. In: *Advanced Materials* 24.10 (2012), pp. 1328–1332. DOI: 10.1002/adma.201103920.

[166] D. A. B. Miller, D. S. Chemla, T. C. Damen, A. C. Gossard, W. Wiegmann, T. H. Wood and C. A. Burrus. 'Band-Edge Electroabsorption in Quantum Well Structures: The Quantum-Confined Stark Effect'. In: *Physical Review Letters* 53.22 (1984), pp. 2173–2176. DOI: 10.1103/PhysRevLett.53.2173.

[167] C. Wood and D. Jena, eds. *Polarization Effects in Semiconductors. From Ab Initio Theory to Device Applications*. New York and London: Springer, 2008. DOI: 10.1007/978-0-387-68319-5.

[168] S. C. Jain, M. Willander, J. Narayan and R. Van Overstraeten. 'III–nitrides: Growth, characterization, and properties'. In: *Journal of Applied Physics* 87.3 (2000), pp. 965–1006. DOI: 10.1063/1.371971.

[169] U. Jahn, J. Lähnemann, C. Pfüller, O. Brandt, S. Breuer, B. Jenichen, M. Ramsteiner, L. Geelhaar and H. Riechert. 'Luminescence of GaAs nanowires consisting of wurtzite and zinc-blende segments'. In: *Physical Review B* 85.4 (2012), p. 045323. DOI: 10.1103/PhysRevB.85.045323. arXiv: 1201.6540 [cond-mat.mtrl-sci].

[170] P. Kusch, E. Grelich, C. Somaschini, E. Luna, M. Ramsteiner, L. Geelhaar, H. Riechert and S. Reich. 'Type-II band alignment of zinc-blende and wurtzite segments in GaAs nanowires: A combined photoluminescence and resonant Raman scattering study'. In: *Physical Review B* 89.4 (2014), pp. 045310–. DOI: 10.1103/PhysRevB.89.045310.

[171] A. Belabbes, C. Panse, J. Furthmüller and F. Bechstedt. 'Electronic bands of III-V semiconductor polytypes and their alignment'. In: *Physical Review B* 86.7 (2012), p. 075208. DOI: 10.1103/PhysRevB.86.075208.

[172] P. Corfdir and P. Lefebvre. 'Importance of excitonic effects and the question of internal electric fields in stacking faults and crystal phase quantum discs: The model-case of GaN'. In: *Journal of Applied Physics* 112.5 (2012), pp. 053512–5. DOI: 10.1063/1.4749789.

[173] B. Eßer. 'Orts- und zeitaufgelöste Spektroskopie an Halbleiter-Nanodrähten'. German. Diploma thesis. Universität Regensburg, 2012.

[174] B. Ketterer, M. Heiss, M. J. Livrozet, A. Rudolph, E. Reiger and A. Fontcuberta i Morral. 'Determination of the band gap and the split-off band in wurtzite GaAs using Raman and photoluminescence excitation spectroscopy'. In: *Physical Review B* 83.12 (2011), pp. 125307–. DOI: 10.1103/PhysRevB.83.125307.

[175] B. Ketterer, M. Heiss, E. Uccelli, J. Arbiol and A. Fontcuberta i Morral. 'Untangling the Electronic Band Structure of Wurtzite GaAs Nanowires by Resonant Raman Spectroscopy'. In: *ACS Nano* 5.9 (2011), pp. 7585–7592. DOI: 10.1021/nn202585j.

[176] P. Kusch, S. Breuer, M. Ramsteiner, L. Geelhaar, H. Riechert and S. Reich. ‘Band gap of wurtzite GaAs: A resonant Raman study’. In: *Physical Review B* 86.7 (2012), p. 075317. DOI: 10.1103/PhysRevB.86.075317.

[177] Z. Lu, S. Shi, J. Lu and P. Chen. ‘Photoluminescence of the single wurtzite GaAs nanowire with different powers and temperatures’. In: *Journal of Luminescence* 152 (2014), pp. 258–261. DOI: 10.1016/j.jlumin.2014.01.066.

[178] S. Furthmeier, F. Dirnberger, J. Hubmann, B. Bauer, T. Korn, C. Schüller, J. Zweck, E. Reiger and D. Bougeard. ‘Long carrier lifetimes in stacking-fault-free wurtzite GaAs nanowires’. In: *Applied Physics Letters* 105.22 (2014), p. 222109. DOI: 10.1063/1.4903482.

[179] A. Mukherjee, S. Ghosh, S. Breuer, U. Jahn, L. Geelhaar and H. T. Grahn. ‘Spatially resolved study of polarized micro-photoluminescence spectroscopy on single GaAs nanowires with mixed zincblende and wurtzite phases’. In: *Journal of Applied Physics* 117.5 (2015), p. 054308. DOI: 10.1063/1.4907388.

[180] M. Knoll and E. Ruska. ‘Das Elektronenmikroskop’. In: *Zeitschrift für Physik* 78.5-6 (1932), pp. 318–339. DOI: 10.1007/BF01342199.

[181] D. B. Williams and C. B. Carter. *Transmission Electron Microscopy*. 2nd ed. New York: Springer, 2009.

[182] J. Thomas and T. Gemming. *Analytische Transmissionselektronenmikroskopie. Eine Einführung für den Praktiker*. Wien et al.: Springer, 2013. DOI: 10.1007/978-3-7091-1440-7.

[183] L. Reimer and H. Kohl. *Transmission Electron Microscopy. Physics of Image Formation*. 5th ed. Springer Series in Optical Sciences 36. Springer, 2008. DOI: 10.1007/978-0-387-34758-5.

[184] J. C. H. Spence. *High-Resolution Electron Microscopy*. Monographs on the Physics & Chemistry of Materials 60. Oxford: Oxford Science, 2003.

[185] B. Fultz and J. M. Howe. *Transmission electron microscopy and diffractometry of materials*. 4th ed. Berlin and New York: Springer, 2013.

[186] A. V. Crewe, D. N. Eggenberger, J. Wall and L. M. Welter. ‘Electron Gun Using a Field Emission Source’. In: *Review of Scientific Instruments* 39.4 (1968), pp. 576–583. DOI: 10.1063/1.1683435.

[187] *Tecnai on-line help manual – Alignments*. Software version 2. FEI Company. 2004.

[188] H. Busch. ‘Berechnung der Bahn von Kathodenstrahlen im axialsymmetrischen elektromagnetischen Felde’. In: *Annalen der Physik* 386.25 (1926), pp. 974–993. DOI: 10.1002/andp.19263862507.

[189] H. Busch. 'Über die Wirkungsweise der Konzentrierungsspule bei der Braunschen Röhre'. In: *Archiv für Elektrotechnik* 18.6 (1927), pp. 583–594. DOI: 10.1007/BF01656203.

[190] L. Marks. 'What Are the Resolution Limits in Electron Microscopes?' In: *Physics* 6 (2013), p. 82. DOI: 10.1103/Physics.6.82.

[191] O. Scherzer. 'Das theoretisch erreichbare Auflösungsvermögen des Elektronenmikroskops'. In: *Zeitschrift für Physik* 114.7-8 (1939), pp. 427–434. DOI: 10.1007/BF01329522.

[192] M. Haider, S. Uhlemann, E. Schwan, H. Rose, B. Kabius and K. Urban. 'Electron microscopy image enhanced'. In: *Nature* 392.6678 (1998), pp. 768–769. DOI: 10.1038/33823.

[193] M. Haider, P. Hartel, H. Müller, S. Uhlemann and J. Zach. 'Information Transfer in a TEM Corrected for Spherical and Chromatic Aberration'. In: *Microscopy and Microanalysis* 16.04 (2010), pp. 393–408. DOI: 10.1017/S1431927610013498.

[194] S. Uhlemann, H. Müller, P. Hartel, J. Zach and M. Haider. 'Thermal Magnetic Field Noise Limits Resolution in Transmission Electron Microscopy'. In: *Physical Review Letters* 111.4 (2013), p. 046101. DOI: 10.1103/PhysRevLett.111.046101.

[195] G. Y. Fan and M. H. Ellisman. 'Digital imaging in transmission electron microscopy'. In: *Journal of Microscopy* 200.1 (2000), pp. 1–13. DOI: 10.1046/j.1365-2818.2000.00737.x.

[196] M. von Ardenne. 'Das Elektronen-Rastermikroskop'. In: *Zeitschrift für Physik* 109.9-10 (1938), pp. 553–572. DOI: 10.1007/BF01341584.

[197] K. Müller, F. F. Krause, A. Béché, M. Schowalter, V. Galioit, S. Löffler, J. Verbeeck, J. Zweck, P. Schattschneider and A. Rosenauer. 'Atomic electric fields revealed by a quantum mechanical approach to electron picodiffraction'. In: *Nature Communications* 5.5653 (2014). DOI: 10.1038/ncomms6653.

[198] M. Lohr. 'Quantitative Bestimmung innerer elektrischer Felder mit Hilfe von Differentieller Phasenkontrastmikroskopie'. PhD thesis. Universität Regensburg, 2013. eprint: http://epub.uni-regensburg.de/28741/.

[199] A. Pritschet. 'Numerical and experimental investigations of Boersch Phase Plate equipped Condenser Apertures for use in Electron Magnetic Circular Dichroism experiments in a Transmission Electron Microscope'. PhD thesis. Universität Regensburg, 2014. eprint: http://epub.uni-regensburg.de/29293/.

[200] H. Rose. 'Nonstandard imaging methods in electron microscopy'. In: *Ultramicroscopy* 2 (1977), pp. 251–267. DOI: 10.1016/S0304-3991(76)91538-2.

[201] J. Chapman, P. Batson, E. Waddell and R. Ferrier. 'The direct determination of magnetic domain wall profiles by differential phase contrast electron microscopy'. In: *Ultramicroscopy* 3 (1978), pp. 203–214. DOI: 10.1016/S0304-3991(78)80027-8.

[202] J. Chapman, R. Ploessl and D. Donnet. 'Differential phase contrast microscopy of magnetic materials'. In: *Ultramicroscopy* 47.4 (1992), pp. 331–338. DOI: 10.1016/0304-3991(92)90162-D.

[203] T. Uhlig. 'Differentielle Phasenkontrastmikroskopie an magnetischen Ringstrukturen'. PhD thesis. Berlin: Universität Regensburg, 2005.

[204] M. J. Benitez, M. A. Basith, D. McGrouther, S. McFadzean, D. A. MacLaren, A. Hrabec, R. J. Lamb, C. H. Marrows and S. McVitie. 'Engineering magnetic domain-wall structure in permalloy nanowires'. In: *Physical Review Applied* (2015). arXiv: 1501.01410v1 [cond-mat.mtrl-sci]. In press.

[205] M. Lohr, R. Schregle, M. Jetter, C. Wächter, T. Wunderer, F. Scholz and J. Zweck. 'Differential phase contrast 2.0 – Opening new "fields" for an established technique'. In: *Ultramicroscopy* 117 (2012), pp. 7–14. DOI: 10.1016/j.ultramic.2012.03.020.

[206] N. Shibata, S. D. Findlay, Y. Kohno, H. Sawada, Y. Kondo and Y. Ikuhara. 'Differential phase-contrast microscopy at atomic resolution'. In: *Nature Physics* 8.8 (2012), pp. 611–615. DOI: 10.1038/nphys2337.

[207] *Titan Themis*. FEI Company. URL: http://www.fei.com/products/tem/titan-themis/?ind=el (visited on 25/02/2015).

[208] A. Lubk and J. Zweck. 'Differential Phase Contrast – an Integral Perspective'. In: *Physical Review A* 91.2 (2015), p. 023805. DOI: 10.1103/PhysRevA.91.023805.

[209] I. Daberkow. 'Ein frei konfigurierbares ortsauflösendes Detektorsystem für ein Raster-Transmissions-Elektronenmikroskop (STEM)'. PhD thesis. Tübingen: Eberhard-Karls-Universität, 1992.

[210] H. Yang, T. J. Pennycook and P. D. Nellist. 'Efficient phase contrast imaging in STEM using a pixelated detector. Part II: Optimisation of imaging conditions'. In: *Ultramicroscopy* 151 (2014), pp. 232–239. DOI: 10.1016/j.ultramic.2014.10.013.

[211] R. Schregle. 'Kalibrierung eines DPC-Detektors mit Hilfe eines speziell erstellten Probenhalters'. Diploma thesis. Universität Regensburg, 2011.

[212] F. Schwarzhuber. 'Kalibrierung und Charakterisierung des DPC-Modus im Rastertransmissionselektronenmikroskop'. M.Sc. thesis. Universität Regensburg, 2015.

[213] V. Galioit. ‘Kontrastsimulationen zu “Atomic DPC” am Modellsystem GaN’. M.Sc. thesis. Universität Regensburg, 2014.

[214] S. Majert and H. Kohl. ‘High-resolution STEM imaging with a quadrant detector—Conditions for differential phase contrast microscopy in the weak phase object approximation’. In: *Ultramicroscopy* 148 (2015), pp. 81–86. DOI: 10.1016/j.ultramic.2014.09.009.

[215] E. Gatti and P. Rehak. ‘Semiconductor drift chamber — An application of a novel charge transport scheme’. In: *Nuclear Instruments and Methods in Physics Research* 225.3 (1984), pp. 608–614. DOI: 10.1016/0167-5087(84)90113-3.

[216] P. Lechner, S. Eckbauer, R. Hartmann, S. Krisch, D. Hauff, R. Richter, H. Soltau, L. Strüder, C. Fiorini, E. Gatti, A. Longoni and M. Sampietro. ‘Silicon drift detectors for high resolution room temperature X-ray spectroscopy’. In: *Nuclear Instruments and Methods in Physics Research Section A: Accelerators, Spectrometers, Detectors and Associated Equipment* 377.2–3 (1996), pp. 346–351. DOI: 10.1016/0168-9002(96)00210-0.

[217] B. Bauer, J. Hubmann, M. Lohr, E. Reiger, D. Bougeard and J. Zweck. ‘Direct detection of spontaneous polarization in wurtzite GaAs nanowires’. In: *Applied Physics Letters* 104.21 (2014), p. 211902. DOI: 10.1063/1.4880209.

[218] A. Rudolph, M. Soda, M. Kiessling, T. Wojtowicz, D. Schuh, W. Wegscheider, J. Zweck, C. Back and E. Reiger. ‘Ferromagnetic GaAs/GaMnAs Core-Shell Nanowires Grown by Molecular Beam Epitaxy’. In: *Nano Letters* 9.11 (2009), pp. 3860–3866. DOI: 10.1021/nl9020717.

[219] A. Fontcuberta i Morral, D. Spirkoska, J. Arbiol, M. Heigoldt, J. R. Morante and G. Abstreiter. ‘Prismatic Quantum Heterostructures Synthesized on Molecular-Beam Epitaxy GaAs Nanowires’. In: *Small* 4.7 (2008), pp. 899–903. DOI: 10.1002/smll.200701091.

[220] D. Spirkoska, J. Arbiol, A. Gustafsson, S. Conesa-Boj, F. Glas, I. Zardo, M. Heigoldt, M. H. Gass, A. L. Bleloch, S. Estrade, M. Kaniber, J. Rossler, F. Peiro, J. R. Morante, L. Samuelson, G. Abstreiter and A. Fontcuberta i Morral. ‘Structural and optical properties of high quality zinc-blende/wurtzite GaAs hetero-nanowires’. In: *Physical Review B* 80.24 (2009), p. 245325. DOI: 10.1103/PhysRevB.80.245325.

[221] M. J. Tambe, S. Ren and S. Gradečak. ‘Effects of Gold Diffusion on n-Type Doping of GaAs Nanowires’. In: *Nano Letters* 10.11 (2010), pp. 4584–4589. DOI: 10.1021/nl102594e.

[222] M. Soda. 'Structural and morphological TEM characterization of GaAs based nanowires'. PhD thesis. Universität Regensburg, 2012. eprint: http://epub.uni-regensburg.de/25592/.

[223] D. D. Nolte. 'Optical functions of GaAs'. In: *Electronic materials information service. Datareviews series.* Vol. 16: *Properties of Gallium Arsenide.* Ed. by M. R. Brozel and G. E. Stillmann. 3rd ed. London: INSPEC, 1995, p. 201.

[224] 'Gallium phosphide (GaP) dielectric constants'. In: *Group IV Elements, IV-IV and III-V Compounds. Part a - Lattice Properties.* Ed. by O. Madelung, U. Rössler and M. Schulz. Vol. 41A1a. Landolt-Börnstein - Group III Condensed Matter. Berlin and Heidelberg: Springer, 2001, pp. 1–7. DOI: 10.1007/10551045_100.

[225] *GaP - Gallium Phosphide. Basic Parameters at 300 K.* URL: http://www.ioffe.rssi.ru/SVA/NSM/Semicond/GaP/basic.html (visited on 02/06/2015).

[226] N. Shibata, S. D. Findlay, H. Sasaki, T. Matsumoto, H. Sawada, Y. Kohno, S. Otomo, R. Minato and Y. Ikuhara. 'Imaging of built-in electric field at a p-n junction by scanning transmission electron microscopy'. In: *Scientific Reports* 5.10040 (2015). DOI: 10.1038/srep10040.

[227] K. Müller, A. Rosenauer, M. Schowalter, J. Zweck, R. Fritz and K. Volz. 'Strain Measurement in Semiconductor Heterostructures by Scanning Transmission Electron Microscopy'. In: *Microscopy and Microanalysis* 18.05 (2012), pp. 995–1009. DOI: 10.1017/S1431927612001274.

[228] K. Müller, H. Ryll, I. Ordavo, M. Schowalter, J. Zweck, H. Soltau, S. Ihle, L. Strüder, K. Volz, P. Potapov and A. Rosenauer. 'STEM strain analysis at sub-nanometre scale using millisecond frames from a direct electron read-out CCD camera'. In: *Journal of Physics: Conference Series* 471.1 (2013), pp. 012024–. DOI: 10.1088/1742-6596/471/1/012024.

[229] J. Hubmann, B. Bauer, H. Körner, S. Furthmeier, M. Buchner, G. Bayreuther, F. Dirnberger, D. Schuh, C. Back, J. Zweck, E. Reiger and D. Bougeard. 'Epitaxial growth of room-temperature ferromagnetic MnAs segments on GaAs nanowires via sequential crystallization'. In: *Nano Letters* 16.2 (2016), pp. 900–905. DOI: 10.1021/acs.nanolett.5b03658.

[230] J. Hubmann. 'GaAs nanowires: Epitaxy, crystal structure-related properties and magnetic heterostructures'. PhD thesis. Universität Regensburg, 2015.

[231] K. H. Ploog. 'Spin injection in ferromagnet-semiconductor heterostructures at room temperature (invited)'. In: *Journal of Applied Physics* 91.10 (2002), pp. 7256–7260. DOI: 10.1063/1.1446125.

[232] T. Jungwirth, J. Sinova, J. Mašek, J. Kučera and A. H. MacDonald. 'Theory of ferromagnetic (III,Mn)V semiconductors'. In: *Reviews of Modern Physics* 78 (3 2006), pp. 809–864. DOI: 10.1103/RevModPhys.78.809.

[233] F. Ishikawa, K. Koyama, K. Watanabe, T. Asano and H. Wada. 'First-Order Phase Transition at the Curie Temperature in MnAs and $MnAs_{0.9}Sb_{0.1}$'. In: *Journal of the Physical Society of Japan* 75.8 (2006), pp. 084604–. DOI: 10.1143/JPSJ.75.084604.

[234] P. V. Radovanovic, C. J. Barrelet, S. Gradečak, F. Qian and C. M. Lieber. 'General Synthesis of Manganese-Doped II–VI and III–V Semiconductor Nanowires'. In: *Nano Letters* 5.7 (2005), pp. 1407–1411. DOI: 10.1021/nl050747t.

[235] M. Hilse, Y. Takagaki, M. Ramsteiner, J. Herfort, S. Breuer, L. Geelhaar and H. Riechert. 'Strain in GaAs-MnAs core-shell nanowires grown by molecular beam epitaxy'. In: *Journal of Crystal Growth* 323.1 (2010), pp. 307–310. DOI: 10.1016/j.jcrysgro.2010.10.126.

[236] K. Gas, J. Sadowski, T. Kasama, A. Siusys, W. Zaleszczyk, T. Wojciechowski, J.-F. Morhange, A. Altintaş, H. Q. Xu and W. Szuszkiewicz. 'Structural and optical properties of self-catalytic GaAs:Mn nanowires grown by molecular beam epitaxy on silicon substrates'. In: *Nanoscale* 5.16 (2013), pp. 7410–7418. DOI: 10.1039/C3NR01145C. arXiv: 1312.5460 [cond-mat.mtrl-sci].

[237] H. Ohno, A. Shen, F. Matsukura, A. Oiwa, A. Endo, S. Katsumoto and Y. Iye. '(Ga,Mn)As: A new diluted magnetic semiconductor based on GaAs'. In: *Applied Physics Letters* 69.3 (1996), pp. 363–365. DOI: 10.1063/1.118061.

[238] S. S. A. Seo, T. W. Noh, Y.-W. Kim, J. D. Lim, Y. D. Park, Y. S. Kim, Z. G. Khim, H. C. Jeon, T. W. Kang and S. J. Pearton. 'Nondestructive spectroscopic method to detect MnAs metallic nanocrystals in annealed GaAs:Mn'. In: *Journal of Applied Physics* 95.12 (2004), pp. 8172–8177. DOI: 10.1063/1.1739524.

[239] M. Yatago, H. Iguchi, S. Sakita and S. Hara. 'Growth and Characterization of MnAs Nanoclusters Embedded in GaAs Nanowires by Metal-Organic Vapor Phase Epitaxy'. In: *Japanese Journal of Applied Physics* 51.2S (2012), 02BH01–. DOI: 10.1143/JJAP.51.02BH01.

[240] S. Hara, H. Fujimagari, S. Sakita and M. Yatago. 'Difference in formation of ferromagnetic MnAs nanoclusters on III-V semiconducting nanowire templates'. In: *Proceedings of SPIE 8820*. Vol. 88200V. Society of Photo-Optical Instrumentation Engineers (SPIE) Conference Series. 2013. DOI: 10.1117/12.2023173.

[241] T. A. Bither and W. H. Cloud. 'Magnetic Tetragonal δ Phase in the Mn-Ga Binary'. In: *Journal of Applied Physics* 36.4 (1965), pp. 1501–1502. DOI: 10.1063/1.1714349.

[242] M. Boström and S. Hovmöller. 'Preparation and Crystal Structure of the Pseudo-Decagonal Approximant Mn_3Ga_5'. In: *Journal of Solid State Chemistry* 153.2 (2000), pp. 398–403. DOI: 10.1006/jssc.2000.8790.

[243] O. Gourdon and G. J. Miller. 'Reinvestigation of the GaMn structure and theoretical studies of its electronic and magnetic properties'. In: *Journal of Solid State Chemistry* 173.1 (2003), pp. 137–147. DOI: 10.1016/S0022-4596(02)00031-2.

[244] G. Cliff and G. W. Lorimer. 'The quantitative analysis of thin specimens'. In: *Journal of Microscopy* 103.2 (1975), pp. 203–207. DOI: 10.1111/j.1365-2818.1975.tb03895.x.

[245] G. Priante, S. Ambrosini, V. G. Dubrovskii, A. Franciosi and S. Rubini. 'Stopping and Resuming at Will the Growth of GaAs Nanowires'. In: *Crystal Growth & Design* 13.9 (2013), pp. 3976–3984. DOI: 10.1021/cg400701w.

[246] B. Jenichen, V. M. Kaganer, M. Kästner, C. Herrmann, L. Däweritz, K. H. Ploog, N. Darowski and I. Zizak. 'Structural and magnetic phase transition in MnAs(0001)/GaAs(111) epitaxial films'. In: *Physical Review B* 68.13 (2003), p. 132301. DOI: 10.1103/PhysRevB.68.132301.

[247] Y. Takagaki, E. Wiebicke, L. Däweritz and K. H. Ploog. 'Distribution of α and β phases in the coexistence regime in MnAs(0001) layers grown on GaAs(111)B'. In: *Applied Physics Letters* 85.9 (2004), pp. 1505–1507. DOI: http://dx.doi.org/10.1063/1.1786359.

[248] R. Engel-Herbert, T. Hesjedal, D. M. Schaadt, L. DÃ¤weritz and K. H. Ploog. 'Micromagnetic properties of MnAs(0001)/GaAs(111) epitaxial films'. In: *Applied Physics Letters* 88.5 (2006), p. 052505. DOI: http://dx.doi.org/10.1063/1.2171790.

[249] J. Varalda, A. J. A. de Oliveira, A. Ouerghi, M. Eddrief, M. Marangolo, D. Demaille, V. H. Etgens, N. Mattoso and D. H. Mosca. 'Growth and magnetic properties of MnAs epitaxied on GaAs(111)B'. In: *Journal of Applied Physics* 100.9 (2006), p. 093524. DOI: 10.1063/1.2364389.

[250] Y. Takagaki, C. Herrmann, J. Herfort, C. Hucho and K.-J. Friedland. 'Stress-modified structural and electronic properties of epitaxial MnAs layers on GaAs'. In: *Physical Review B* 78.23 (2008), pp. 235207–. DOI: 10.1103/PhysRevB.78.235207.

[251] M. Tanaka, J. P. Harbison, M. C. Park, Y. S. Park, T. Shin and G. M. Rothberg. 'Epitaxial orientation and magnetic properties of MnAs thin films grown on (001) GaAs: Template effects'. In: *Applied Physics Letters* 65.15 (1994), pp. 1964–1966. DOI: 10.1063/1.112831.

[252] S. Assali. 'RE: Spontaneous polarization measurements on WZ GaP nanowires'. Private communication. 2014.

Own Publications

Journal Articles

J. Hubmann, B. Bauer, H. Körner, S. Furthmeier, M. Buchner, G. Bayreuther, F. Dirnberger, D. Schuh, C. Back, J. Zweck, E. Reiger and D. Bougeard. 'Epitaxial growth of room-temperature ferromagnetic MnAs segments on GaAs nanowires via sequential crystallization'. In: *Nano Letters* 16.2 (2016), pp. 900–905. DOI: 10.1021/acs.nanolett.5b03658.

B. Bauer, J. Hubmann, M. Lohr, E. Reiger, D. Bougeard and J. Zweck. 'Direct detection of spontaneous polarization in wurtzite GaAs nanowires'. In: *Applied Physics Letters* 104.21 (2014), p. 211902. DOI: 10.1063/1.4880209.

S. Furthmeier, F. Dirnberger, J. Hubmann, B. Bauer, T. Korn, C. Schüller, J. Zweck, E. Reiger and D. Bougeard. 'Long carrier lifetimes in stacking-fault-free wurtzite GaAs nanowires'. In: *Applied Physics Letters* 105.22 (2014), p. 222109. DOI: 10.1063/1.4903482.

B. Bauer, A. Rudolph, M. Soda, A. Fontcuberta i Morral, J. Zweck, D. Schuh and E. Reiger. 'Position controlled self-catalyzed growth of GaAs nanowires by molecular beam epitaxy'. In: *Nanotechnology* 21.43 (2010), p. 435601. DOI: 10.1088/0957-4484/21/43/435601. arXiv: 1006.4060v2 [cond-mat.mes-hall].

Conference Contributions

Contributions as first or presenting author

B. Bauer, J. Hubmann, J. Wild, E. Reiger, D. Bougeard and J. Zweck. 'Direct Detection of Spontaneous Polarization in Wurtzite GaAs Nanowires via Differential Phase Contrast Microscopy'. In: 18th International Microscopy Congress. (Prague, 7th–12th Sept. 2014). 2014. Poster presentation.

B. Bauer, J. Hubmann, M. Lohr, E. Reiger, D. Bougeard and J. Zweck. 'Direct detection of spontaneous polarization in wurtzite GaAs nanowires'. In: 7th nanowire growth workshop. (Lausanne, 10th–12th June 2013). 2013, p. 80. Poster presentation.

S. Leinfelder, B. Bauer and J. Zweck. 'Construction and first results from a sample holder for cathodoluminescence measurements in a TEM'. In: *Proceedings of the 15th European Microscopy Congress*. European Microscopy Congress EMC 2012. (Manchester, 16th–21st Sept. 2012). 2012. Conference talk.

A. Rudolph, B. Bauer, M. Soda, J. Zweck and E. Reiger. 'Crystal structure control of Au-catalyzed GaAs nanowires'. In: *6th Nanowire Growth Workshop*. (St. Petersburg, 4th–6th June 2012). 2012, p. 36. Conference talk.

B. Bauer, J. Bill, M. Soda, A. Rudolph, E. Reiger and J. Zweck. 'Elemental and Structural Analysis of Nanowires in Cross-Sectional Specimens'. In: *Verhandlungen der Deutschen Physikalischen Gesellschaft*. DPG Frühjahrstagung (Spring Meeting) of the Condensed Matter Section (SKM). (Berlin, 25th–30th Mar. 2012). Vol. 47. 4. 2012, p. 230. Poster presentation.

B. Bauer, J. Bill, M. Soda, A. Rudolph, E. Reiger and J. Zweck. 'Ultramicrotomy: a fast and gentle sample preparation method for nanowire cross sections'. In: *Proceedings of the Microscopy Conference MC 2011 Kiel*. Microscopy Conference MC 2011. (Kiel, 28th Aug.–2nd Sept. 2011). 2011. Poster presentation.

J. Hubmann, B. Bauer, A. Rudolph, A. Fontcuberta i Moral, D. Schuh, D. Bougeard, J. Zweck and E. Reiger. 'Influence of the nanowire interdistance on growth conditions and crystal structure of self-catalyzed GaAs nanowires grown via MBE'. In: *Verhandlungen der Deutschen Physikalischen Gesellschaft*. DPG Frühjahrstagung (Spring Meeting) of the Condensed Matter Section (SKM). (Dresden, 13th–18th Mar. 2011). Vol. 46. 1. 2011, p. 377. Poster presentation.

B. Bauer. 'Influence of the nanowire interdistance on growth conditions and crystal structure of self-catalyzed GaAs nanowires grwon via MBE'. In: *III–V Nanowires. Growth, Properties, and Applications*. 473. WE-Heraeus-Seminar. (Bad Honnef, 21st–23rd Feb. 2011). 2011. Poster presentation.

B. Bauer, A. Rudolph, A. Fontcuberta i Morral, D. Schuh, M. Soda, J. Zweck and E. Reiger. 'Position control of self-catalyzed MBE-grown GaAs nanowires'. In: *Verhandlungen der Deutschen Physikalischen Gesellschaft*. DPG Frühjahrstagung (Spring Meeting) of the Condensed Matter Section (SKM). (Regensburg, 21st–26th Mar. 2010). Vol. 45. 3. 2010, p. 320. Conference talk.

A. Rudolph, M. Soda, M. Kiessling, B. Bauer, D. Schuh, T. Wojtowicz, W. Wegscheider and E. Reiger. 'MBE growth of GaAs/GaMnAs core-shell nanowires'. In: *Verhandlungen der Deutschen Physikalischen Gesellschaft*. DPG Frühjahrstagung (Spring Meeting) of the Condensed Matter Section (SKM). (Regensburg, 22nd–27th Mar. 2009). Vol. 44. 5. 2009, p. 256. Poster presentation.

Acknowledgements

Science is, as the saying goes, about dwarfs standing on the shoulders of giants and – as also is life – it is not a one man show. Hence, there are a lot of people to be thanked for having been on this journey with me. Not all of them may be giants themselves, but nonetheless they have their fair share in the success of this work. And although I gave my best to remember and mention them all in one way or another, there will surely be some whom I unwittingly didn't think of – whoever they are, they may feel acknowledged here as well.

- My supervisor, Joe Zweck, for giving me the opportunity to work in his group, for leaving me the freedom to choose among the numerous topics to explore the ones I found most interesting, but being supportive, approachable, and open for discussions whenever it was necessary.

- The nanowire group around Elisabeth Reiger and Dominique Bougeard for providing me with lots of solvable and unsolvable problems and samples to characterize that would be enough for several PhD lifetimes.

- The whole TEM group around Joe Zweck for the good work atmosphere, for mind-blowing, brain-twisting, constructive – sometimes also distractive – discussions, for after-work beers and spare-time activities. They came as colleagues but many of them left as friends.

- The heart and soul of our chair – Sylvia, Magdalena and Claudia from the secretary's office – for their help and support with all the smaller and bigger everyday issues, fighting the administrative dragon and still always having an open ear and time for a coffee.

- All the members of the Chair of Christian Back for legendary chair parties, excursions, lunchtime and coffee break discussions and for the doubtful 'honour' to be their *Kaffeewart* for one year.

- Both the nanowire and electron microscopy scientific community for highly interesting conferences and inspiring discussions in great venues and getting to know many great and interesting minds.

- The German Research Foundation (DFG) for funding via Grants SFB 689 'Spin Phenomena in Reduced Dimensions' and 'Focused Researcher's Group: PolarCoN (FOR 957)'.
- René Hübner (Helmholtz-Zentrum Dresden-Rossendorf) and Peter Veith (Universität Magdeburg) for the opportunity to visit their labs and learn from their expertise.
- The LaTeX community for the tools that allow to write – and draw, thanks to Ti*k*Z and PGFPLOTS – optically pleasing documents.
- All the friends that have been with me during my PhD time and hopefully beyond for making life worth living.
- My two families – my in-laws as well as my own – for having made me what I am today, especially my father who has inspired and always encouraged my scientific curiosity.
- And finally my wife, Verena, for accepting me as I am, bearing my moods, listening to my problems, not complaining when work was more important than coming home, for pushing me and not pushing me, for being there when I needed someone to be there and letting me be when I needed to be alone. Thank you for being part of my life!

Thank you all!

Colophon

The process which finally leads to a finished dissertation in experimental physics makes quite inevitably use of data processing tools throughout all stages of its generation. As far as possible, open source software has been used to complete these tasks. In particular the following tools have been employed:

Data acquisition For data acquisition the software supplied with the respective instruments has been used. These were

- *Gatan Digital Micrograph* for TEM images,
- *FEI TIA* for STEM images,
- *Bruker Esprit 2* for EDX data.

Since the DPC system was developed within the workgroup and custom made for the instrument the acquisition of its data was performed using the *DPCWitch2* software developed within the workgroup initially by Matthias Lohr and expanded by Johannes Wild.

General image processing has been performed using *Fiji* ('Fiji Is Just ImageJ'), the image processing suite built upon *ImageJ*. High resolution overview images have been done using the *MosaicJ* image stitching plugin.

DPC image processing The initial processing of the DPC data was performed using Joe Zweck's *DPC Eval Suite*.

1D data processing Line scan data extracted from the acquired images was handled and processed with *QtiPlot*.

Data visualization The data graphs in this work have been plotted using the PGFPLOTS library for LaTeX.

Drawing All drawings in this document are drawn with the Ti*k*Z library for LaTeX.

Typesetting The whole document has been typeset in LaTeX 2ε using pdfLaTeX with KOMA-Script, biblatex/biber and the lmodern fonts from the TeX Live distribution.